

THESIS FOR THE DEGREE OF DOCTOR OF PHILOSOPHY

Polymer-Based Micromachining for Scalable and Cost-Effective Fabrication of Gap Waveguide Devices Beyond 100 GHz

SADIA FARJANA



Department of Microtechnology and Nanoscience
CHALMERS UNIVERSITY OF TECHNOLOGY

Göteborg, Sweden 2023

Polymer-Based Micromachining for Scalable and Cost-Effective Fabrication of Gap Waveguide Devices Beyond 100 GHz

SADIA FARJANA

ISBN 978-91-7905-845-6

© SADIA FARJANA, 2023.

Doktorsavhandlingar vid Chalmers tekniska högskola

Ny serie nr 5311

ISSN 0346-718X

Department of Microtechnology and Nanoscience

Chalmers University of Technology

SE-412 96 Gothenburg

Sweden

Telephone + 46 (0)31-772 1000

Cover: From left to right, top to bottom: periodic pin structures at 140 GHz fabricated by dry film photoresist, power divider at 300 GHz fabricated by dry film photoresist, bent ridge gap waveguide transmission line at 300 GHz fabricated by dry film photoresist.

Printed by Chalmers Reproservice

Gothenburg, Sweden 2023

To my family

Polymer-Based Micromachining for Scalable and Cost-Effective Fabrication of Gap Waveguide Devices Beyond 100 GHz

SADIA FARJANA

Department of Microtechnology and Nanoscience
Chalmers University of Technology

Abstract

The terahertz (THz) frequency bands have gained attention over the past few years due to the growing number of applications in fields like communication, healthcare, imaging, and spectroscopy. Above 100 GHz transmission line losses become dominating, and waveguides are typically used for transmission. As the operating frequency approaches higher frequencies, the dimensions of the waveguide-based components continue to decrease. This makes the traditional machine-based (computer numerical control, CNC) fabrication method increasingly challenging in terms of time, cost, and volume production. Micromachining has the potential of addressing the manufacturing issues of THz waveguide components. However, the current microfabrication techniques either suffer from technological immaturity, are time-consuming, or lack sufficient cost-efficiency. A straightforward, fast, and low-cost fabrication method that can offer batch fabrication of waveguide components operating at THz frequency range is needed to address the requirements.

A gap waveguide is a planar waveguide technology which does not suffer from the dielectric loss of planar waveguides, and which does not require any electrical connections between the metal walls. It therefore offers competitive loss performance together with providing several benefits in terms of assembly and integration of active components. This thesis demonstrates the realization of gap waveguide components operating above 100 GHz, in a low-cost and time-efficient way employing the development of new polymer-based fabrication methods.

A template-based injection molding process has been designed to realize a high gain antenna operating at D band (110 - 170 GHz). The injection molding of OSTEMER is an uncomplicated and fast device fabrication method. In the proposed method, the time-consuming and complicated parts need to be fabricated only once and can later be reused.

A dry film photoresist-based method is also presented for the fabrication of waveguide components operating above 100 GHz. Dry film photoresist offers rapid fabrication of waveguide components without using complex and advanced machinery.

For the integration of active circuits and passive waveguides section a straightforward solution has been demonstrated. By utilizing dry film photoresist, a periodic metal pin array has been fabricated and incorporated in a waveguide to microstrip transition that can be an effective and low-cost way of integrating MMIC of arbitrary size to waveguide blocks.

Keywords: Antenna, Dry film photoresist, Gap waveguide, Injection molding, MEMS, mmWave, Polymer microfabrication, Terahertz frequency, Waveguide.

Acknowledgements

I would like to convey my sincere thanks to my former supervisor and examiner Professor Peter Enoksson, for allowing me to work under his supervision in the Micro and Nanosystems group. It has been a pleasure to have him as my main supervisor at the beginning of my PhD journey and later as an assistant supervisor. My greatest gratitude goes to him for his kind and thoughtful supervision, constant support, and guidance. I appreciate the freedom connected with some responsibilities he has given me. It has helped me immensely to grow as a researcher.

I am also grateful to my current supervisor Professor Per Lundgren. It was delightful for me to have him as the main supervisor after my Licentiate and he has supported me a lot with his technical guidance and thoughtful discussions during these years to smoothly follow the planned research direction. Thank you for always being so supportive and encouraging words.

My sincere gratitude goes to my examiner Prof. Johan Liu for his continuous support. In the supervision team, I would like to thank my co-supervisor Associate Prof. Dr. Vessen Vassilev for so many fruitful technical discussions, guidance, and attention. It was a pleasure to work with you and I have learned so many things from you. I would like to thank my former co-supervisors: Dr. Sjoerd Haas, Dr. Mohammad Amir Ghaderi, and Dr. Sofia Rahiminejad for their support, at the beginning of the PhD journey. Special thanks to Dr. Mohammad Amir Ghaderi for always being on my side and making me feel comfortable to ask for help.

Special thanks to Dr. Esperanza Alfonso. It was a pleasure to work with you. I am thankful to Dr. John Halonen of the Nanofabrication Lab for helping me to establish the new experimental setup in the cleanroom. I am grateful to Dr. Mattias Fredriksson, Dr. Henrik Frederiksen, Dr. Mats Hagberg for your time, effort, and valuable feedback regarding the fabrication process. My heartiest thanks to Mats Myremark for providing all the milled structures used in this thesis. Special thanks go to all the industrial partners involved in the project, especially Thomas Emanuelsson from Ericsson AB, Dr. Jonas Hansson from Mercene Lab AB, Dr. Yinggang Li from Ericsson AB, Ros-Marie Lundh from Saab, Marcus Hasselblad from Gapwaves AB.

A special thanks to my colleagues and friends Azega, Markus, Agin, Carl, Mazharul, Lukas for all the happy hours during our lively lunchroom discussions. I would like to thank my friends Ayesha Bhabi and Tanuja Apu for being on my side during all the ups and downs, for understanding my untold needs, and for covering up many of my responsibilities.

I would like to thank my parents for their unconditional love, continuous support, and blessings. I am grateful to my mother-in-law for her blessings. I am thankful to my brothers and sister-in-law for their inspiration and love. A special thanks go to my youngest brother Rafi, thank you for checking upon me daily and keeping me calm and motivated. I would like to thank my husband Shuvo for his support. Thank you for sharing your knowledge and experience and for making things a lot easier for me. Finally, I would like to thank my two kids, Rumysa and Rayaan, who have sacrificed the most in this journey. You two are my source of joy and happiness, and you inspire me every moment.

Sadia Farjana

Göteborg, June 2023

Preface

This thesis is in partial fulfillment for the degree of Doctor of Philosophy at Chalmers University of Technology, Gothenburg, Sweden.

The work resulting in this thesis was carried out between November 2018 and June 2023 at the Micro- and Nanosystems group, Electronics Material and Systems Laboratory, Department of Microtechnology and Nanoscience.

Professor Peter Enoksson (until June 2021) was the main supervisor and examiner, and Dr. Sjoerd Haas, Dr. Mohammad Amir Ghaderi, and Dr. Sofia Rahiminejad were the co supervisors. Since June 2021 Professor Per Lundgren is the main supervisor and Professor Johan Liu the examiner. In addition, Professor Peter Enoksson and Associate Professor Vessen Vassilev are assistant supervisors.

This work is partially supported by the innovation program "Smartare Elektroniksystem" by Vinnova, Formas and the Swedish Energy Agency the Wenner-Gren Foundation, FORWARD project funded by Strategic vehicle research and innovation program (FFI) 2018-02707, and Adlerbertska Forskningsstiftelsen Fund.

List of Publications

This thesis is based on the work contained in the following papers:

Paper I

Sadia Farjana, Mohammadamir Ghaderi, Ashraf Uz Zaman, Sofia Rahiminejad, Thomas Eriksson, Jonas Hansson, Yinggang Li, Thomas Emanuelsson, Sjoerd Haasl, Per Lundgren, Peter Enoksson. Realizing a 140 GHz Gap Waveguide-Based Array Antenna by Low-Cost Injection Molding and Micromachining. *J Infrared Millimeter, and Terahertz Waves* 42, 893–914 (2021). <https://doi.org/10.1007/s10762-021-00812-8>.

Paper II

Sadia Farjana, Mohamadmir Ghaderi, Sofia Rahiminejad, Sjoerd Haasl, Peter Enoksson. Dry Film Photoresist-Based Microfabrication: A New Method to Fabricate Millimeter-Wave Waveguide Components. *Micromachines* 2021, 12, 260. <https://doi.org/10.3390/mi12030260>.

Paper III

Sadia Farjana, Mohammadamir Ghaderi, Ashraf Uz Zaman, Sofia Rahiminejad, Per Lundgren, Peter Enoksson. Low Loss Gap Waveguide Transmission line and Transitions at 220–320 GHz Using Dry Film Micromachining. *IEEE Transactions on Components, Packaging and Manufacturing Technology*, vol. 11, no. 11, pp. 2012–2021, Nov. 2021, doi: 10.1109/TCPMT.2021.3111137.

Paper IV

Sadia Farjana, Ashraf Uz Zaman, Per Lundgren, Peter Enoksson. Micromachined Wideband Ridge Gap Waveguide Power Divider at 220–325 GHz. *IEEE Access*, vol. 10, pp. 27432–27439, 2022, doi: 10.1109/ACCESS.2022.3156095.

Paper V

Sadia Farjana, Esperanza, Alfonso, Per Lundgren, Vessen Vassilev, Peter Enoksson, Ashraf Uz Zaman. Multilayer Dry Film Photoresist Fabrication of a Robust >100 GHz Gap Waveguide Slot Array Antenna. *IEEE Access*, doi: 10.1109/ACCESS.2023.3271357.

Paper VI

Sadia Farjana, Per Lundgren, Vessen Vassilev, Peter Enoksson, Ashraf Uz Zaman. Micromachined Low-Loss Transition from Waveguide-to-Microstrip Line for Large MMIC Integration and Packaging at 250 GHz. Submitted to IEEE Transactions on Terahertz Science and Technology.

Contribution of the Author

The contribution of Sadia Farjana to each publication, major (•••), partial (••), or minor (•)

Paper	Design	Fabrication	Characterization	Writing
I	•	•••	••	•••
II	•	•••	•••	•••
III	•••	•••	•••	•••
IV	•••	•••	•••	•••
V	••	•••	•••	•••
VI	•••	•••	•••	•••

Other related publications by the Author not included in this thesis:

- i. Sadia Farjana, Esperanza Alfonso, Per Lundgren, Vessen Vassilev, Peter Enoksson, Ashraf Uz Zaman. 140 GHz Gap Waveguide Based Slot Array Antenna Fabrication Technique by Dry Film photoresist. IEEE International Symposium on Antennas and Propagation and USNC-URSI Radio Science Meeting, July 23–28, 2023, Portland, Oregon, USA.
- ii. Sadia Farjana, Per Lundgren, Peter Enoksson and Ashraf Uz Zaman. Micromachined Ridge Gap Waveguide Transmission Line and Transition at 220–310 GHz. 2021 IEEE International Symposium on Antennas and Propagation and USNC-URSI Radio Science Meeting (APS/URSI), Singapore, Singapore, 2021, pp. 1297-1298, doi: 10.1109/APS/URSI47566.2021.9703735.
- iii. Sadia Farjana, Mohammad Amir Ghaderi, Ashraf Uz Zaman and Peter Enoksson. Polymer based D-Band Multi-layer Gap Waveguide Slot Antenna Array for Line of Sight (LOS) MIMO Systems. ICEAA-IEEE APWC 2020, Honolulu, Hawaii, USA, August 10-14, 2020.
- iv. Sadia Farjana, Sofia Rahiminejad, Ashraf Uz Zaman, Jonas Hansson, Mohammad Amir Ghaderi, Sjoerd Haasl, Peter Enoksson. Polymer based 140 GHz Planar Gap Waveguide Array Antenna for Line of Sight (LOS) MIMO Backhaul Links, 2019 IEEE MTT-S International Microwave Workshop Series on Advanced Materials and Processes for RF and THz Applications (IMWS-AMP), Bochum, Germany, 2019, pp. 148-150, doi: 10.1109/IMWS-AMP.2019.8880101.
- v. Sadia Farjana, Sofia Rahiminejad, Mohammad Amir Ghaderi, Sjoerd Haasl, Peter Enoksson. Fabrication of Multilayer Planar Array Antenna by SU8. MME 2019, 30th Micromechanics and Microsystems Europe workshop. 18-20 August 2019, Oxford, United Kingdom.
- vi. Sadia Farjana, Ashraf Uz Zaman, Sofia Rahiminejad, Jonas Hansson, Tomas Eriksson, Sjoerd Haasl, Tomas Emanuelsson, Jonas Hansryd, Yinggang Li, Peter Enoksson. Micromachined 140 GHz Planar Gap Waveguide Array Antenna for Line of Sight (LOS) MIMO Backhaul Links, published in Swedish Microwave Day, Lund, 2018.
- vii. Sadia Farjana, Ashraf Uz Zaman, Sofia Rahiminejad, Jonas Hansson, Tomas Eriksson, Sjoerd Haasl, Tomas Emanuelsson, Jonas Hansryd, Yinggang Li, Peter Enoksson.

- Micromachined D-Band Multi-layer Gap Waveguide Slot Antenna Array for Line of Sight (LOS) MIMO Systems, published in Micronano system workshop, Finland, 2018.
- viii. Sadia Farjana, Ashraf Uz Zaman, Peter Enoksson. Pick and Place Assembly Technique for Fabrication of Groove Gapwaveguide Resonator. Journal of Physics: Conference Series. 922. 012017. 10.1088/1742-6596/922/1/012017.

Table of Contents

Part I

Chapter 1 Introduction.....	1
1.1 Terahertz Technology	1
1.2 RF-MEMS for Terahertz Applications	3
1.3 Challenges at THz Frequencies.....	3
1.3.1 Transmission line issues at high frequencies.....	4
1.3.2 Geometrical complexity and manufacturing tolerance.....	7
1.3.3 Characterization.....	8
1.3.4 Integration and packaging	10
1.3.5 Thermal effects	12
1.4 Aim and Outline of the Thesis	12
Chapter 2 Technology Alternatives for THz Components	15
2.1 CNC Milling.....	15
2.2 3D Printing	16
2.3 Micromachining	17
2.3.1 Silicon micromachining.....	17
2.3.2 LIGA method.....	18
2.3.3 Photoresist-based method.....	19
2.3.4 Surface micromachining.....	21
2.4 Challenges and Motivation.....	21
Chapter 3 Overview of Gap Waveguide Technology	23
3.1 Fundamentals of Gap Waveguide Technology	23
3.2 Design of Parallel Plate Stopband Realized by Bed of Nails.....	25
3.3 Benefits of Gap Waveguide Technology for THz Applications	26
3.4 Applications of Gap Waveguide Technology	26
Chapter 4 Template-Based Injection Molding.....	29
4.1 Background	29
4.2 Motivation	31
4.3 Challenges	31
4.4 Materials and Method.....	33
4.4.1 Master fabrication by SU8 photoresist	33

4.4.2 PDMS mold fabrication.....	34
4.4.3 Injection molding of OSTEMER.....	35
4.5 Fabrication of 140 GHz Slot Array Antenna	36
4.5.1 Method I	36
4.5.2 Method II	37
4.5.3 Results and Discussion	38
Chapter 5 Dry Film Photoresist-Based Method.....	41
5.1 Motivation	41
5.2 Challenges	42
5.3 Material and Method	42
5.4 Process Optimization.....	45
5.4.1 Exposure dose selection.....	45
5.4.2 Thick resist lamination	48
5.5 Fabricated Devices	49
5.6 Summary	59
Chapter 6 Transition from Waveguide-to-Microstrip Line.....	61
6.1 Background and Motivation.....	61
6.2 Challenges	62
6.3 Transition Design	63
6.3.1 Supporting metal block design	64
6.4 Fabrication Method	65
6.4.1 EBG pin fabrication.....	65
6.4.2 Microstrip line fabrication.....	66
6.5 Results and Discussion.....	67
Chapter 7 Conclusion and Future Work.....	71
7.1 Future Work	72
Bibliography.....	74

Part II

Appended Papers.....	87
-----------------------------	-----------

List of Figures

Figure 1.1: Image of CNC milled planar array antenna based on gap waveguide technology operating at different frequencies (a) 16×16 slot array antenna at 30 GHz, (b) 16×16 slot array antenna at 60 GHz, (c) 16×12 slot array antenna at 140 GHz.	2
Figure 1.2: Planar transmission lines (a) Microstrip line. (b) Coplanar waveguide. (c) Stripline.	4
Figure 1.3: Standard hollow metal waveguides, (a) rectangular waveguide, (b) circular waveguide.	5
Figure 1.4: Schematic of substrate integrated waveguide.	6
Figure 1.5: Different versions of gap waveguides, (a) ridge gap waveguide, (b) groove gap waveguide, (c) microstrip gap waveguide.	6
Figure 1.6: (a) A multistep DRIE process for complex THz waveguide components [27], (b) waveguide circuits of a mixer operating in the 1.6–2 THz frequency range by thick resist electroforming technology [28], (c) a 300 GHz E-plane waveguide bend manufactured by SU-8 micromachining technology [29], (d) an example of a fabricated waveguide filter after metallization at WR-3 by SU8 photoresist [30].	7
Figure 1.7: Measurement interfaces for THz waveguide passive component characterization. (a) A microfabricated compression pin and in-plane edge-port interfacing method [35], (b) out-of-plane vertical-port interfacing method for a RGW structure at 220 – 325 GHz (Paper III), (c) design of a supporting metal block GW pin flange adaptor to compensate for the gap between the interface of the metal block and the micromachined chip for vertical-port interfacing method (Paper V), (d) on-wafer probing method [43].	9
Figure 1.8: Various transitions used to connect MMICs and RW. (a) An Inline transition from RW to microstrip[48], (b) a RW to microstrip transition by E-plane probe[52], (c) vertical transition between RW to microstrip line [51], (d) a RW to microstrip transition with metal pin lid for oversized MMIC substrate [47].	11
Figure 2.1: (a) CNC milled waveguide component for use at 260 GHz [54], (b) a 1.5 THz balanced HEB mixer with integrated feed horns [54].	16
Figure 2.2: (a) 3D printed E-, D-, and H-band horns [65], (b) D-Band 3D-Printed all metal antenna [66].	16
Figure 2.3: (a) SEM image of the waveguide structure and coupling slots, (b) radiating elements with a zoomed view showing the coupling slots, (c) pictures of the manufactured antennas mounted on a standard WM- 570 waveguide flange[82].	18
Figure 2.4: Optical microscope image of one symmetric half after the photoresist removal, lapping, and polishing [102].	19
Figure 2.5: Photograph of a fabricated planar array 8×8 slotted waveguide, (a) radiating side, (b) back side [111].	20
Figure 2.6: Stress-related bend in thick SU8 structure released from the substrate.	20
Figure 3.1: Basic concept of gap waveguide technology. (a) PEC – PMC parallel-plate electromagnetic wave cutoff. (b) TEM local waves propagation through the strip.	23

Figure 3.2: 'Bed of nails' structures by periodically placed electrically conductive pins.	24
Figure 3.3: A PEC surface and an AMC surface are placed parallel to each other.	24
Figure 3.4: Different versions of gap waveguide geometries, (a) ridge gap waveguide. (b) groove gap waveguide. (c) microstrip gap waveguide. (d) inverted-microstrip gap waveguide [130].	25
Figure 3.5: (a) A microstrip-to-groove gap waveguide transition operating at W-band [159], (b) rectangular waveguide to ridge gap waveguide transition [160].	27
Figure 4.1: Schematic of the template-based injection molding process. (a-f) fabrication of SU8 master, (g-h) fabrication of PDMS mold, (i-j) Injection molding of polymer OSTEMER (Paper I).	32
Figure 4.2: Image of SU8 masters, (a) slot layer, (b) cavity layer, (c) feed layer.	33
Figure 4.3: Fabrication of PDM mold for the slot layer, (a) before toluene treatment, (b) after toluene treatment.	34
Figure 4.4: Injection molding steps for the cavity layer. (a) PDMS mold for the cavity layer, (b) aluminum (Al) mold, (c) closed image of the milled Al piece showing the pins to create the cavity opening after injection molding, (d) PDMS mold on top of the aluminum mold, ready for injection molding, (e) cavity layer made of OSTEMER after UV exposure and heat cure, (d) cavity layer after conductive layer deposition.	35
Figure 4.5: A schematic process plan to fabricate SU8 slot layer.	36
Figure 4.6: Simulated and measured S_{11} for the 16×16 element antenna array. (a) The slot layer was made of SU8, the cavity layer, and the feed layer was made of OSTEMER, (b) all layers were made of OSTEMER (Paper I).	37
Figure 4.7: Fabricated antenna, (a) slot Layer, (b) feed Layer, (c) cavity Layer, (d) complete antenna mounted of the milled base plate.	38
Figure 4.8: Flow chart of the fast fabrication process.	39
Figure 4.9: Misalignment between PDMS mold and Al mold. (a) Al mold for the cavity layer, (b) placing PDMS mold with the aluminum mold for injection molding of OSTEMER, (c) schematic of misalignment that happened during placing two molds.	40
Figure 5.1: Dry film photoresist lamination steps, (a) removing the PET sheet, (b) dry film photoresist placed on a wafer and the wafer placed in carrier plate, (c) lamination of dry film photoresist, (d) withdrawing the middle plastic sheet slowly.	43
Figure 5.2: Schematic of dry film fabrication.	44
Figure 5.3: (a) Base layer after delamination of pins, (b) A pin released from the base layer.	46
Figure 5.4: SUEX structures after optimizing the exposure dose, (a) bend ridge, (b) part of the resonator, (c) T- ridge section of the transition.	46
Figure 5.5: SEM image of a fabricated structure showing vertical sidewalls.	47
Figure 5.6: Lamination of thick photoresist by using shims.	49
Figure 5.7: SEM image of a fabricated resonator and full electromagnetic wave simulation compared with measurement results (Paper II).	50
Figure 5.8: Fabricated chip. (a) Straight RGW on chip (b) bend RGW chip, (C) groove GW chip. SEM images of the fabricated chips: (d) straight RGW, (e) bend RGW (Paper III).	51

Figure 5.9: Schematic of the misalignment of the ridge with respect to the WG position, (a) transverse direction, (b) longitudinal direction, and (c) top and bottom plate of the support package with the fabricated chip (Paper III).	52
Figure 5.10: Measured (solid line) and simulated (dashed lines) S-parameters of the back-to-back (a) straight RGW transmission line, (b) bend RGW transmission line, (c) GGW transmission line (Paper III).	53
Figure 5.11: (a) Microscopic image, (b) SEM image of the fabricated power divider, (c) closeup SEM image of the T-section, (d) measurement setup.	55
Figure 5.12: The fabricated antenna, (a) slot layer, (b) feed layer, (c) supporting bottom plate with WR-6.5 opening and gap waveguide pin flange structure, (d) fabricated antenna mounted in the machined supporting plate and connected to the VDI D-band extender.	56
Figure 5.13: Measured surface roughness of the fabricated antenna at different thermal cycles.	57
Figure 5.14: Simulated and measured S11 of the fabricated antenna before and after the thermal cycling test.	58
Figure 5.15: The schematic of a case where the fabrication of a pin of 380 μm height is part of a multilayer fabrication.	59
Figure 6.1: Proposed packaging solution as an inline transition.	63
Figure 6.2: Proposed packaging solution as a vertical transition for arbitrary width substrate.	64
Figure 6.3: Schematic of the metal block, (a) bottom plate of the inline transition, (b) top plate of the inline transition, (c) bottom plate of the vertical transition, (d) top plate of the vertical transition.	65
Figure 6.4: Schematic of the quartz fabrication, (a) preparing the quartz substrate for handling, (b) deposition of the seed layer, (c) spin coat resist S1813, (d) exposure of the photoresist, (e) photoresist after development, (f) electroplating of the quartz wafer, (g) removal of the photoresist, (h) dicing of the quartz wafer and releasing from the handling wafer.	66
Figure 6.5: Fabricated microstrip chip and EBG pins mounted on the milled metal block, (a) vertical transition, (b) inline transition.	67
Figure 6.6: Measurement of the vertical transition, (a) measurement setup for the back-to-back waveguide transition, (b) simulation and measured S-parameter results for the back-to-back vertical transition.	68
Figure 6.7: Measurement of the inline transition, (a) measurement setup for the back-to-back waveguide transition, (b) simulation and measured return loss for the back-to-back inline transition, (c) simulation and measured insertion loss for the back-to-back inline transition.	68
Figure 6.8: Schematic of the air gap between two split blocks for the inline transition.	69

Acronyms

AR	Aspect Ratio
AMC	Artificial Magnetic Conductor
CNC	Computer Numerically Controlled
CPW	Coplanar Waveguides
DRIE	Deep Reactive Ion Etching
EM wave	Electromagnetic Wave
EBG	Electromagnetic Band Gap
GGW	Groove Gap Waveguide
GW	Gap Waveguide
IC	Integrated Circuit
LCP	Liquid Crystal Polymer
LTCC	Low Temperature Co-Fired Ceramic
MEMS	Micro-Electrical-Mechanical-System
MMIC	Monolithic Microwave Integrated Circuit
mmWave	Millimeter-Wave
PA	Power Amplifier
PCB	Printed Circuit Board
PDMS	Polydimethylsiloxane
PEB	Post Exposure Bake
PEC	Perfect Electric Conductive
PET	Polyethylene
PLB	Post Lamination Bake
PMC	Perfect Magnetic Conductive
PNA	Performance Network Analyzer
Q-TEM	Quasi Transverse Electromagnetic Modes
TEM	Transverse Electromagnetic Modes
RF	Radio Frequency
RGW	Ridge Gap Waveguide
RW	Rectangular Waveguide
SEM	Scanning Electron Microscope

SIW	Substrate Integrated Waveguide
Sub-mmWave	Sub-Millimeter-Wave
SOI	Silicon On Insulator
TE	Transverse Electric
THz	Tera Hertz
TEM	Transverse Electromagnetic
TM	Transverse Magnetic
UV	Ultraviolet
VNA	Vector Network Analyzer

Part I

Chapter 1

Introduction

This chapter presents the objective of the thesis to the reader. It gives a brief introduction to terahertz (THz) technology and describes THz MEMS technology together with different types of waveguides technologies. The challenges and possible solutions for the realization of THz components are mentioned as a background analysis for the work in the thesis.

1.1 Terahertz Technology

In recent years, the development of a new generation of wireless systems has greatly impacted the daily lives and social activities of people [1]. As the lower frequency range of the radio frequency (RF) spectrum becomes crowded, future telecommunications and RF applications are expected to shift towards higher frequency spectrums, which offer larger bandwidth, smaller components, and less interference.

The term RF encompasses electromagnetic waves in the frequency range of 3 kHz to 3 THz and therefore covers millimeter-wave (mmWave), sub-millimeter-wave (sub-mmWave), and THz frequencies. The mmWave range includes frequencies from 30 to 300 GHz, with wavelengths between 10 mm and 1 mm. While sub-mmWave radiation or THz ranges from 100 GHz to 3 THz (depending on the definition) [2-4]. In this thesis, "THz" refers to the sub-mmWave frequency range for our practical applications. Potential commercial wireless applications operating at the THz frequency range include high data rate wireless communication, high precision industrial radars, sensing, imaging, and life science [5-13].

At and above mmWave frequency, the losses of the transmission lines play a key role in the performance of the RF systems. Hollow rectangular waveguides (RW) are the transmission line of choice at THz frequencies. Passive components such as high-Q bandpass filters, orthomode transducers, and planar slot array antennas are commonly realized in hollow waveguide structures, due to the low insertion loss and high-power handling capability of RW. Designing RW-based THz components presents several technological and mechanical challenges, such as smaller size, increased system density, effective packaging, crosstalk suppression, low power operation, and cost pressure. Therefore, breakthroughs in low-loss, low-cost, wideband THz components and systems are required to take THz technology closer to consumer products. New design methodologies, semiconductor technologies, and integration concepts can help address some of these issues. However, the fabrication requirements needed for the realization of the delicate three-dimensional (3D) THz waveguide

components still is considered a bottleneck. This is usually addressed within the frames of the manufacturing sector considering mass production in a cost-efficient way.

The well-known fact is that if we move towards higher frequencies, the component size decreases, making traditional machining techniques such as computer numerical control (CNC) metal machining and electric discharge machining (EDM) unfeasible for THz waveguide components due to strict fabrication requirements, increased manufacturing time to achieve delicate dimensional features and hence increased cost. Using these techniques to manufacture metal waveguides operating at mmWave frequencies, specifically above 60 GHz, is both complicated and costly [14-16]. The challenges become more and more prominent as the operating frequency moves towards an even higher frequency, especially above 100 GHz. Figure 1.1 shows an image of slot array antennas operating at different frequencies and represents the miniaturizing trend of moving toward high frequency.

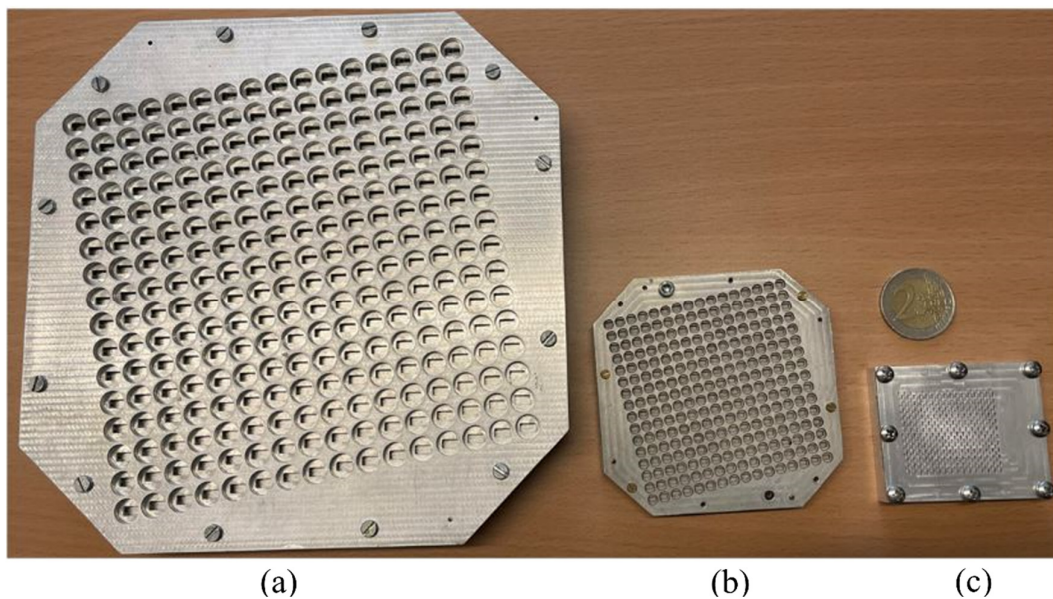


Figure 1.1: Image of CNC milled planar array antenna based on gap waveguide technology operating at different frequencies: (a) 16×16 slot array antenna at 30 GHz, (b) 16×16 slot array antenna at 60 GHz, (c) 16×12 slot array antenna at 140 GHz.

In this regard, having upcoming THz applications in mind, a new, alternative fabrication technology that can offer low-cost, rapid manufacturing of miniaturized waveguide components is needed. This is where MEMS (Micro-Electro-Mechanical System) based fabrication which is also known as micromachining can play a significant role. Micromachining, a technique that enables the construction of 3D micro-sized structures on or within a substrate, offers a solution to cost-effectively fabricate small, compact components. In the early 1970s, MEMS-based sensors have been developed based on photolithographic processes, which allow entire batches of devices in a single run, resulting in a lower cost per device when produced in volume [17]. A similar micromachining concept has also been developed for the fabrication of THz waveguide components. However, this technology still has to evolve significantly to realize cost-effective 3D waveguide components at the THz frequency range.

1.2 RF-MEMS for Terahertz Applications

At an early stage, MEMS have been used to fabricate different sensor devices. In the early 1980s, RF-MEMS switches have been demonstrated for low-frequency applications. The demonstrated RF-MEMS switch can create a short circuit or an open circuit in a transmission line by mechanical motion. In 1991, with the finance of the Defense Advanced Research Projects Agency (DARPA), Dr. Larry Larson designed the first MEMS switch for microwave applications and demonstrated excellent performance up to 50 GHz. Today, MEMS is a mature technology with advanced infrastructure and processes; it is possible to achieve high-volume production of MEMS components. MEMS-based passive components and systems that operate at THz frequency have numerous strengths over conventional metal-block THz devices in terms of higher compactness, reduced cost, and weight. The RF MEMS research field can be divided into different areas [17]:

- i) RF-MEMS switches, varactors, and inductors,
- ii) micromachined transmission lines, high-Q resonators, filters, and antennas,
- iii) FBAR (thin Film Bulk Acoustic Resonators) and filters, and
- iv) RF micromechanical resonators and filters.

The thesis is focused on the second research area of RF-MEMS.

1.3 Challenges at THz Frequencies

The huge potential of THz technology comes with major challenges. RF systems operating at THz frequencies suffer from strong atmospheric attenuation and high path loss and they are vulnerable to weather conditions [5]. Theoretically, increasing the transmitted power can solve the above-mentioned issues. However, the RF power that THz sources can deliver is low and this is one of the most significant challenges. So, the compensation for the high atmospheric attenuation in the THz range has been done by minimizing the loss generated by the rest of the components. Generally, highly-directive antennas with high aperture efficiency are needed and can be realized by reflector antennas [18]. However, the solution comes with a large volume and high cost. Planar array antennas are more attractive in this case, due to their lower volume and weight. As mentioned earlier, the hollow waveguide is popular for realizing passive components at THz frequencies, due to low insertion loss and high-power handling. Yet, the manufacturing cost of the hollow waveguide is high at millimeter-wave frequencies due to the strict tolerance requirements in the split-block construction technique. Therefore, the challenges at THz frequency come in different forms:

- i) choice of transmission line technology,
- ii) design tolerance and choice of the manufacturing method,
- iii) characterization of the THz components,
- iv) integration and packaging,
- v) thermal issues.

In this section, we will discuss the most relevant challenges that have been addressed in the works presented in the thesis.

1.3.1 Transmission line issues at high frequencies

Waveguides and transmission lines are the key components of any THz system for guiding, manipulating, or simply transmitting signals. Well-established transmission line technologies are hollow waveguide technology, planar waveguides such as striplines, microstrip lines, coplanar waveguide (CPW), substrate integrated waveguide (SIW), and gap waveguide (GW) technology. In this section, the benefits and drawbacks of the above-mentioned technologies will be discussed.

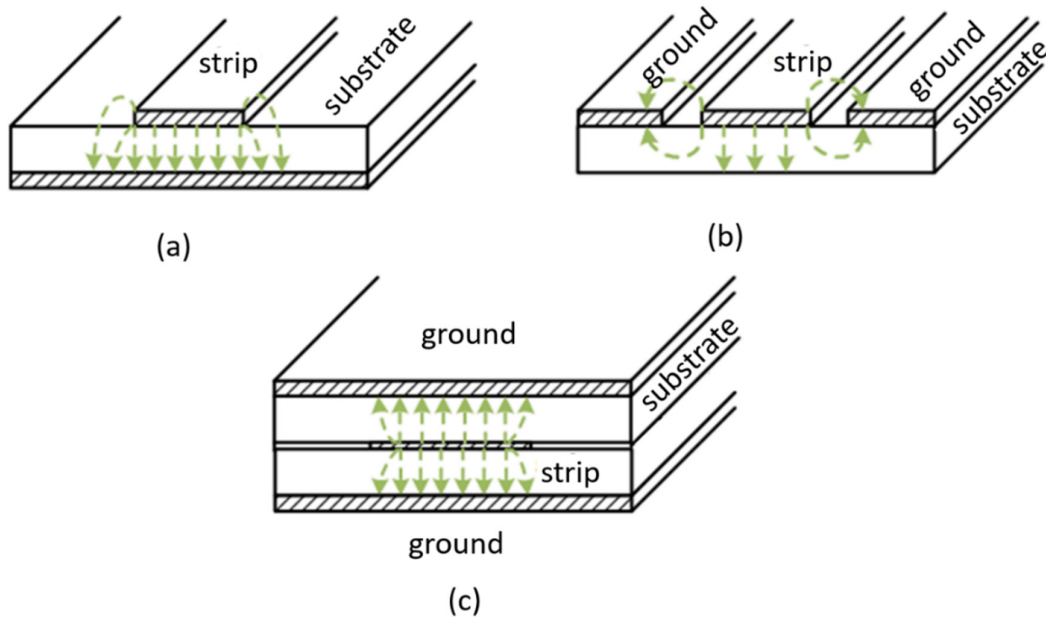


Figure 1.2: Planar transmission lines: (a) microstrip line, (b) coplanar waveguide, (c) stripline.

i) Planar transmission lines

The microstrip (a type of transmission line that consists of a conductor fabricated on a dielectric substrate with a grounded plane), stripline (typically consists of a conducting strip surrounded by a dielectric material and sandwiched between two conducting ground planes), and coplanar waveguide (CPW) (a strip conductor with two ground planes parallel and on both side of the strip on the same dielectric substrate) lines are typical representations of a planar transmission line structure. Figure 1.2 shows the schematics and E-field distributions of planar transmission lines with their respective modes. The main advantages of planar transmission lines are their robustness, being mass producible at low-cost, and allowing direct integration with active microwave components on circuit boards. Nevertheless, these transmission lines suffer from high dielectric and ohmic losses, as the transmission property depends on the material parameters of a (lossy) substrate. For this reason, these transmission lines are not appropriate for high-efficiency antennas and low-loss filters at THz frequency.

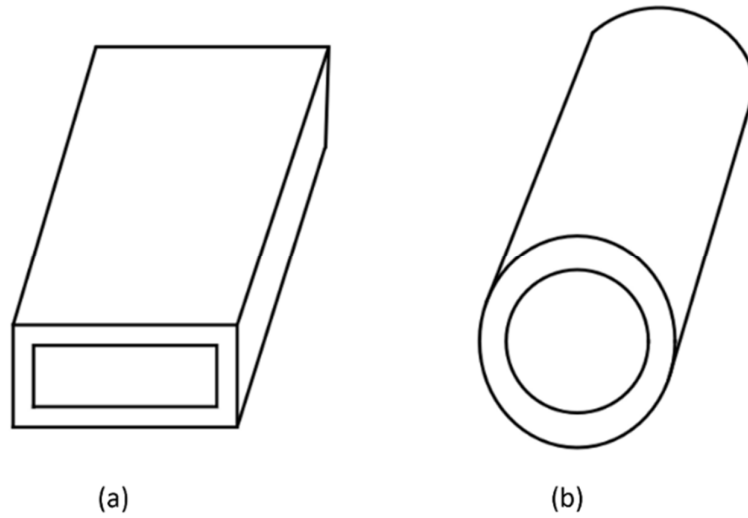


Figure 1.3: Standard hollow metal waveguides: (a) rectangular waveguide, (b) circular waveguide.

ii) Hollow waveguides

Standard hollow waveguides have existed in microwave operation for a long time in the form of circular waveguides and rectangular waveguides (RW), as shown in Figure 1.3. Compared to planar transmission lines, standard hollow waveguides have high power handling capability and lower losses[19]. However, their main challenge lies in finding low-cost fabrication alternatives for components in the THz frequency ranges. As shown in Figure 1.3, conventional waveguides are single-conductor transmission lines. If fabricated in two blocks, a very highly conductive metal connection is required between the metal blocks to allow propagation of the desired mode with maintained low losses. Also, the non-planar design of standard waveguides is their major disadvantage as it makes their integration difficult in the current trend of all-in-one chip integrated circuits, with passive and active components in the same module. The traditional way to manufacture standard waveguides is CNC milling and it becomes more and more challenging and expensive at THz frequencies[15, 16, 20].

iii) Substrate integrated waveguides

The substrate integrated waveguide (SIW) or post-wall waveguide, illustrated in Figure 1.4, has lately been introduced [21, 22]. It combines some of the advantages of planar transmission lines and hollow waveguides. The SIW can be realized in printed technology, where two rows of metalized via-holes replace the narrow walls of the waveguide. The planar profile makes them interesting for integration with active components. However, due to the presence of a dielectric material, the SIW faces the same problem as microstrip transmission lines, i.e. high dielectric losses. Also, it displays some radiation losses due to the via holes providing non-perfect shielding [23, 24].

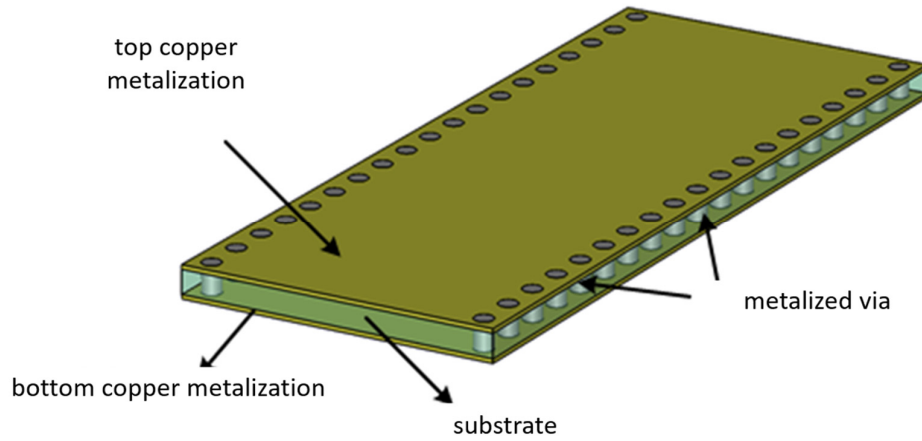


Figure 1.4: Schematic of substrate integrated waveguide.

iv) Gap waveguide technology

The gap waveguide (GW) technology is comparatively new and was introduced by Kildal *et al.* [25, 26]. An illustration of different gap waveguide structures is shown in Figure 1.5. In gap waveguides, the field is traveling in the air gap between parallel metal plates, and unlike in a standard hollow waveguide, no connection between the side walls is required for the electrical performance of the waveguide. Moreover, like microstrip transmission lines, CPWs, and SIWs, this structure can keep a planar profile, without suffering from any dielectric loss since it can support waves in the air. For these above-mentioned reasons, the gap waveguide is a promising alternative to hollow waveguides and microstrip lines for high-frequency applications. The details of gap waveguide structures will be presented in Chapter 3.

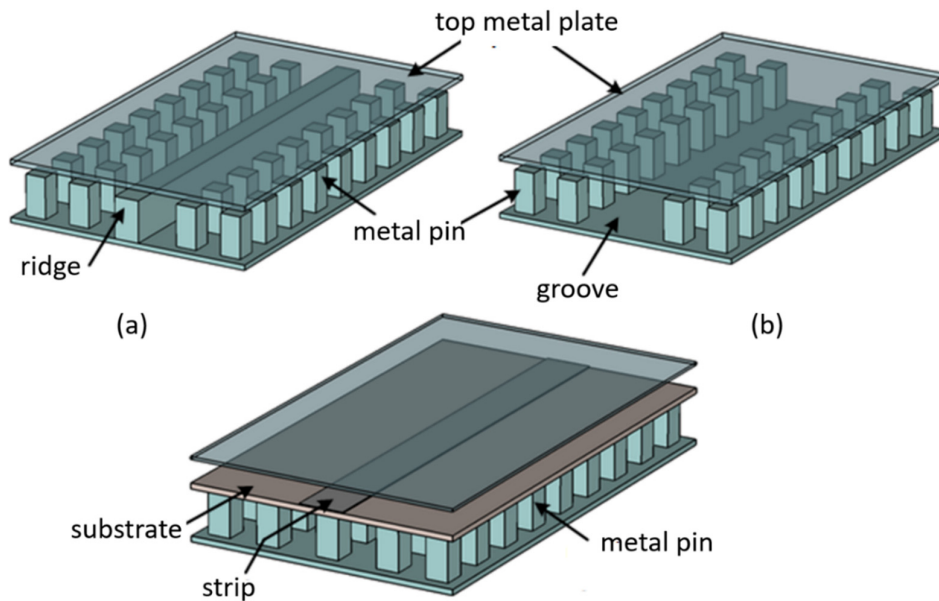


Figure 1.5: Different versions of gap waveguides: (a) ridge gap waveguide, (b) groove gap waveguide, (c) microstrip gap waveguide.

1.3.2 Geometrical complexity and manufacturing tolerance

The main challenge for the use of waveguide components at high frequencies comes from the wavelength-dependent miniaturization mentioned at the beginning of this chapter. Additionally, the fabrication of 3D THz waveguide devices is very different and much more complex than 2D structures. Due to their reduced size and increased sensitivity to fabrication errors, most common machining techniques become unpractical for the implementation of such THz waveguide components, see Chapter 2. Some common fabrication challenges have been presented in this section which will be later described in detail in Chapter 2.

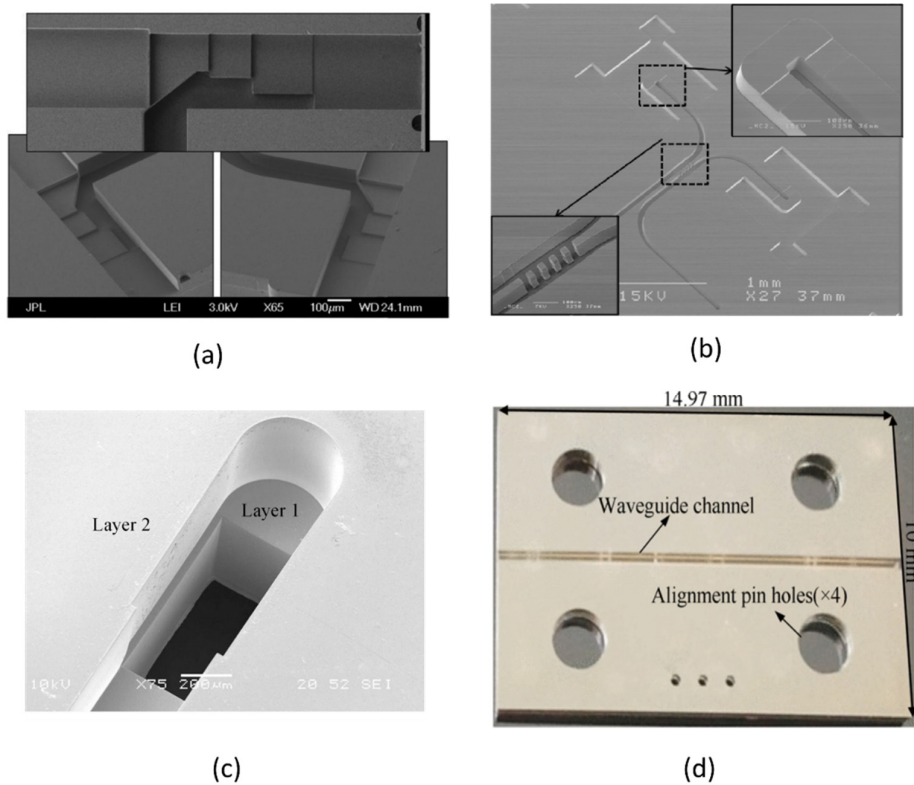


Figure 1.6: (a) A multistep DRIE process for complex THz waveguide components [27], (b) waveguide circuits of a mixer operating in the 1.6–2 THz frequency range by thick resist electroforming technology [28], (c) a 300 GHz E-plane waveguide bend manufactured by SU8 micromachining technology [29], (d) an example of a fabricated waveguide filter after metallization at 220–325 GHz by SU8 photoresist [30].

Fabrication issues

MEMS technology offers precise control of structures from a few micrometers to a few hundred micrometers and has been confirmed as a suitable method for producing a variety of high-performance THz components [31–34], shown in Figure 1.6. However, challenges remain in fabricating complex 3D structures due to small feature sizes and the demand for high fabrication accuracy. Sidewall verticality, surface roughness, geometrical tolerance, and gaps between separately fabricated pieces after mounting them together are a few common geometrical complexities that need to be addressed by the micromachining steps.

Many attempts based on different micromachining technologies to realize high-performance THz components have been made. Among the different micromachine methods, silicon (Si) micromachining, thick resist, or SU8-based techniques, and electroforming or LIGA (Lithographie, Galvanformung, Abformung) are the most commonly used and are discussed in detail in Chapter 2. However, when approaching THz frequencies, small fabrication imperfections could induce significant performance degradation or changes, such as additional losses, quality-factor (Q-factor) reduction, frequency shift, or bandwidth change, despite the convenience of the fabrication method. As a solution for the above-mentioned problems, the fabrication process should comprise as few steps as possible, which is sometimes very critical considering the expectations of the application.

The work presented in the thesis is focused on the improvement of fabrication issues (dimensional tolerance, surface roughness improvement without post-processing, and fast fabrication). The challenges of the existing methods and possible solutions are discussed in the following chapters. In Paper I, a molding technique has been proposed where the complicated and time-consuming part is done only once, which simplifies the final device fabrication. Paper II to Paper V present a new fabrication scheme based on dry film photoresist and demonstrate its benefits over existing micromachining methods. The detail of the fabrication methods is presented in Chapter 4 and Chapter 5 respectively.

1.3.3 Characterization

The testing of the passive components is very important before integrating them with the active devices while developing a system. The characterization can be done by an in-plane measurement, where a waveguide extends to the edge of the device [35], by extending the waveguide interface vertically through the device [33, 36, 37], or on wafer measurement by probing a CPW-waveguide transition [38]. The advanced vector network analyzer (VNA), and frequency extenders, are capable to perform S-parameter measurements up to the THz range by using a waveguide or CPW probe [39, 40]. Different ways of characterization techniques are shown in Figure 1.7.

The on-wafer circuit measurement is a basic method and does not require any direct waveguide interfaces, therefore avoiding assembly issues. However, this characterization approach has not been considered in this thesis as this is mainly for circuit/planar transmission line measurement. The rest of the characterization methods require a machined metal block as an adapter or a supporting piece, to connect the device under test (DUT) and the standard waveguide flanges. The measurement accuracy significantly depends on the manufacturing precision of the metal supporting block and the alignment accuracy between the metal block to the measurement setup. However, there are additional challenges exist when a micromachined DUT needs to be oriented in the metal supporting block. Firstly, the assembly or alignment accuracy of the fabricated pieces to the metal supporting block. In the case of metal machined devices, precision alignment is accomplished by using undersized alignment holes as it is possible to press the pins through the undersized holes. However, this is not possible in the case of micromachined devices as they are fragile and can deform or crack if force has been applied. In the case of a device that requires multilayer structures, the misalignment effect can be a further challenge. Additionally, due to the imperfect vertical edges of the DUT, a gap can be introduced between the test flange and the DUT.

Different attempts have been made to compensate for the above-mentioned issues. A microfabricated compression pin has been used to improve the alignment accuracy between the chip and the metal-supporting block [35], a GW-based pin flange adaptor has been used to compensate for the gap between the interface of the opening for the waveguide in the metal-supporting block and the micromachined device [41], and a non-galvanic transition from micromachined component to a metallic rectangular waveguide has been proposed, to compensate for the imperfect vertical edges of the micromachined DUT and a gap between the test flange [42]. In this thesis, a vertical transition with high alignment tolerance has been proposed in Paper III, where a simple approach to compensate for the misalignment between the DUT and the position of the waveguide has been proposed by creating a deep channel on the machined piece. In Paper I and Paper V, the GW pin flange adapter was used to compensate for the alignment gap between the chip and the CNC machined adapter.

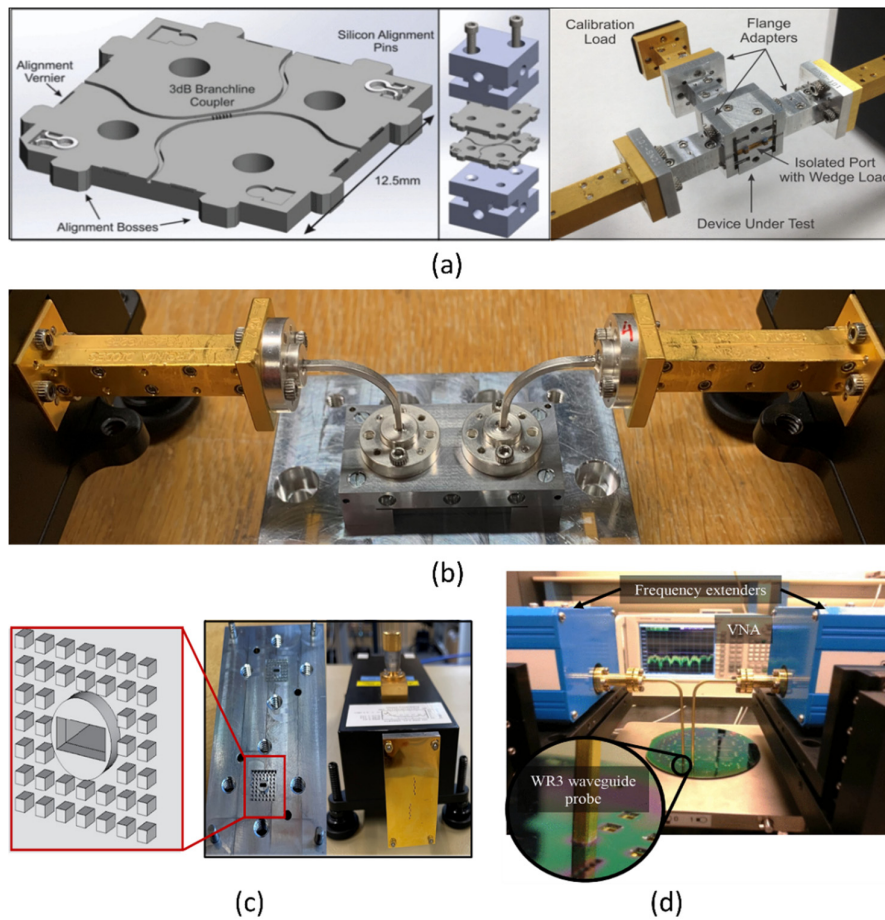


Figure 1.7: Measurement interfaces for THz waveguide passive component characterization. (a) A microfabricated compression pin and in-plane edge-port interfacing method [35], (b) out-of-plane vertical-port interfacing method for a RGW structure at 220 – 325 GHz (Paper III), (c) design of a supporting metal block GW pin flange adaptor to compensate for the gap between the interface of the metal block and the micromachined chip for vertical-port interfacing method (Paper V), (d) on-wafer probing method [43].

1.3.4 Integration and packaging

Another major challenge at THz frequency is integration, low-loss interconnectivity, and the lack of high-performance packaging solutions. Integration and packaging can be classified into three levels:

- i) single RF chip or transceiver integration,
- ii) multiple chip module interconnects, and
- iii) system-level packaging and shielding.

Among the different integration techniques, bond wires and flip-chip packaging are the most common and have been gaining popularity in recent years [44]. However, there are still some challenges to accomplishing the performance requirements needed in THz systems such as low loss and wide bandwidth. Furthermore, wire bonding suffers from poor repeatability and manufacturability challenges above 100 GHz, and flip chip mounting onto an underlying substrate involves some parasitic phenomena and can lead to significant performance deterioration of a packaged system [45].

A solution to this is directly coupling the MMICs (monolithic microwave integrated circuits) with the waveguide by using an E-plane probe, inline transition, or vertical transition. Figure 1.8 shows different approaches of the waveguide to microstrip transition. To support the designed transition, waveguides are machined on E-plane split-block or H-plane split-block configurations in metal blocks which are subsequently assembled, to form a complete structure. The problem with using H-plane split block is that any tiny gap between the metal blocks will perturb the current on the side wall as the current is strong along the side wall of the waveguide, hence the energy will leak via the tiny gap. Even though CNC milling can achieve high fabrication precision and good surface quality, at the THz band it can be still very challenging to attain proper contact between the split blocks. Therefore, the preferable way of integrating active components is using an E-plane split block. Here the MMIC substrate is inserted in E-plane through a narrow channel and coupled directly to the waveguide and this offers low-loss and wideband performance. However, the limitation of this technique is the dimension of the MMIC substrate, due to the propagation of higher modes in an oversized substrate. To mitigate this problem the MMIC substrate part containing the transition is reshaped and made narrow enough not to allow cavity modes to propagate [46]. However, this is not the most convenient solution as that narrow part of the MMIC substrate becomes mechanically fragile and breaks easily. Also, the production of such a narrow substrate is very challenging and can be expensive. This limitation has been overcome by using an artificial magnetic conductor surface in the lid to suppress the substrate mode in an oversized substrate [47].

Among the different RF transitions, in-line transitions have been proposed by different groups to integrate a single RF chip [48-50]. Those transitions use H-plane split waveguide blocks where smaller height waveguide sections are used and gradually tapered to full height waveguide. One such demonstrated transition operating at 74 GHz to 80 GHz has shown 1.5 ± 0.5 dB insertion loss per transition [49]. Similarly, different approaches have been made to design vertical transitions. One example is using the coplanar patch to convert the quasi-transverse electric and magnetic (Q-TEM) mode of the microstrip to the transverse electric TE₁₀ mode of the rectangular waveguide and a microstrip line is fed directly at the non-radiating edge of the patch with an offset from the center line of the patch [51]. Typically, those transitions are narrowband and prone to leakage via the gap between the waveguide block and the printed circuit board (PCB).

An improved and compact inline transition will be presented in this thesis where a $\lambda/4$ cavity is used on the bottom plate to couple field from the microstrip line to the waveguide and a perfect magnetic conductor (PMC) is used on the top lid to achieve a non-galvanic contact between the microstrip and the waveguide section. The detail of the design and the fabrication will be presented in Chapter 6. The thesis also presents a vertical transition and demonstrates the usefulness of GW pins for transition operating at high frequency. The designed transitions also utilize the benefits of dry film photoresist while fabricating the GW pins. The detail of the fabrication process and design of the transition is presented in Paper VI and Chapter 6.

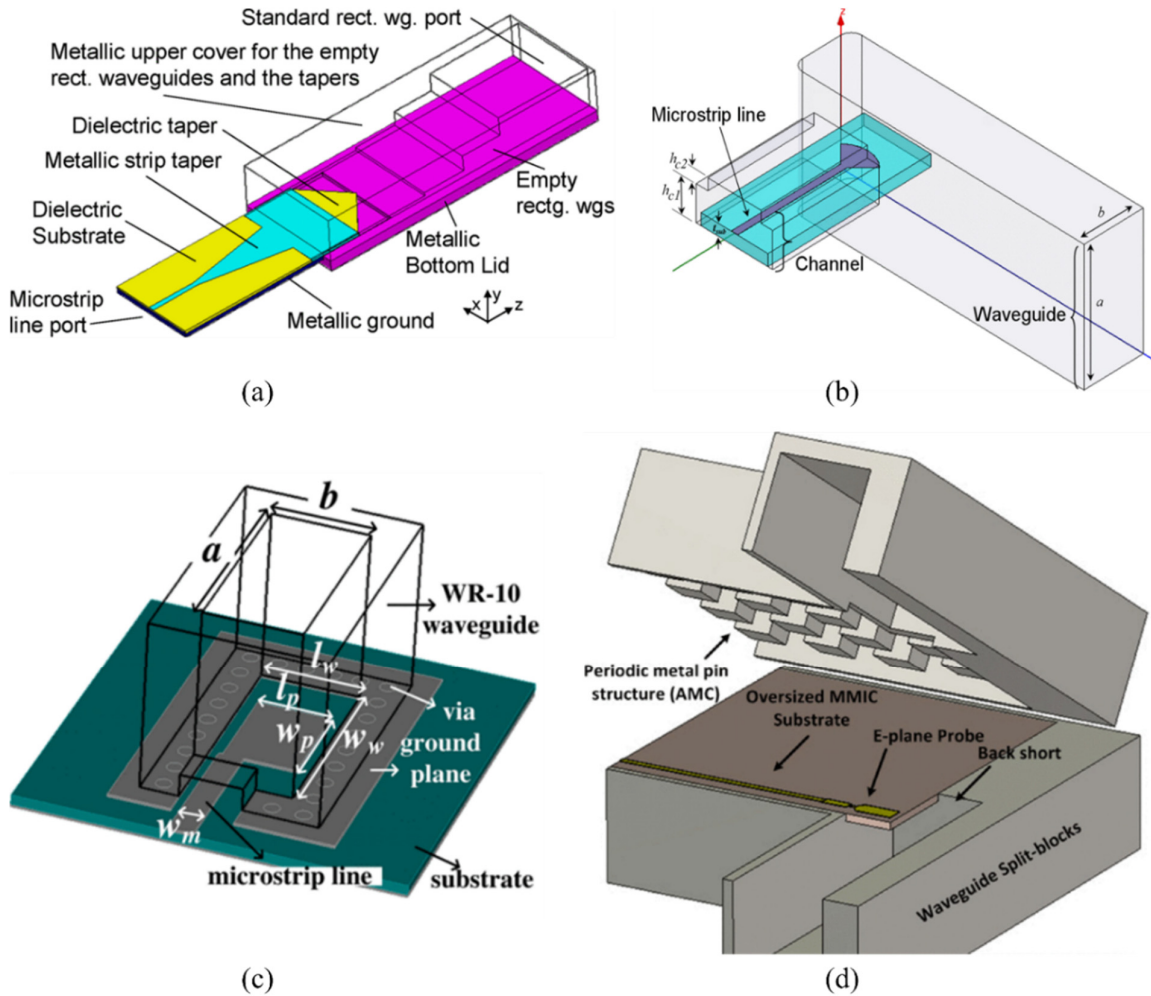


Figure 1.8: Various transitions used to connect MMICs and RW: (a) an Inline transition from RW to microstrip[48], (b) a RW to microstrip transition by E-plane probe[52], (c) a vertical transition between RW to microstrip line [51], (d) a RW to microstrip transition with metal pin lid for oversized MMIC substrate [47].

1.3.5 Thermal effects

Another challenge at THz frequency is related to thermal effects and it is of serious concern, especially when taking packaging into account. The localized heating of the active devices affects the entire system and efforts are needed to maintain proper cooling. However, it becomes more challenging when the passive components are fabricated by polymers. Polymers, having poor thermal conductivity and a relatively high coefficient of thermal expansion (CTE), can cause deformation, delamination of the component itself from the packaging, or delamination of the deposited conductive metal layer.

Aiming towards obtaining a low-cost microfabrication technique for future THz waveguide components, this thesis has been focused on polymer-based microfabrication methods. Paper II- Paper VI presents a novel technique to use SU-8 dry film photoresist to fabricate waveguide components above 100 GHz. Paper V presents the results of conducting a thermal cycling test which indicates the possibility of using dry film photoresist SU-8 in applications where large temperature variations can occur.

1.4 Aim and Outline of the Thesis

Waveguide components operating at THz frequency offer many benefits. Yet, the main challenge for the use of waveguide components at high frequencies comes from wavelength-dependent miniaturization. The conventional machining techniques become impractical due to the reduced size of the waveguide components and increased requirements on fabrication tolerances.

Micromachining has proven itself a suitable candidate to fabricate waveguide components operating at THz frequencies. However, the existing micromachining techniques suffer from different fabrication issues and require many processing steps, or they are time-consuming, or not cost-efficient. The cost of any process is a combination of production type (serial or batch), and the cost of the material, equipment, lab, and labor hours. Therefore, a fabrication method utilizing low-cost material and offering time-efficient batch fabrication of devices can be claimed as a low-cost method. This thesis addresses the existing challenges of the polymer-based method and proposes solutions to those problems considering the manufacturing time and cost.

This thesis proposes a solution in this regard and presents straightforward, fast, and low-cost micro-fabrication methods that can offer batch fabrication of THz waveguide components. A template-based injection molding process has been designed to realize a high-gain antenna operating at the D band (110 - 170 GHz). In the proposed method, the time-consuming and complicated parts need to be fabricated only once and can later be reused. A dry film photoresist-based method is also presented in this thesis to fabricate waveguide components operating above 100 GHz. Dry film photoresist offers rapid fabrication of waveguide components without using sophisticated tools.

Apart from the waveguide component fabrication, integration of planar electronics with the waveguide module also becomes challenging at the THz frequency range. In this thesis, a simple transition without the strict requirement of electrically conductive connections between the top and the bottom metal block can solve many issues. By utilizing a dry film photoresist, a periodic metal-coated pin array has been fabricated and this was later incorporated in a

waveguide to microstrip transition that can be an effective and low-cost solution for integrating large-size MMIC to waveguide blocks.

The first part of the thesis is organized as follows:

Chapter 2 presents the current and emerging machining and micromachining techniques used for the fabrication of waveguide components operating at THz frequencies. This chapter also covers the motivation of the thesis in the context of state-of-the-art micromachining methods.

Chapter 3 introduces gap waveguide theory, which covers an overview of the gap waveguide technology and its working principle.

Chapter 4 presents the motivation behind the developed template-based injection molding method. It also presents the fabricated device by the developed fabrication method and discusses the challenges of the fabrication method.

Chapter 5 shows the dry film photoresist-based method, its benefits, and challenges and presents the fabricated devices.

Chapter 6 presents the micromachined low-loss transition from the waveguide-to-microstrip line. This chapter describes the fabrication of the microstrip chip and the characterization challenges of the designed transition.

Chapter 7 presents an overall conclusion of the thesis and the proposed future work that looks the most promising

In the second part of the thesis, the most relevant contributions of the author are included in the form of six appended papers. Additionally, other related publications can be found as references in the section List of Publications.

Chapter 2

Technology Alternatives for THz Components

This chapter presents the state-of-the-art manufacturing methods used for the realization of passive waveguide components at THz frequencies. This chapter also covers the advantages and challenges of the existing methods. The motivation for using the developed polymer-based methods will be mentioned here.

2.1 CNC Milling

CNC milling is the traditional and dominating method for manufacturing waveguide components at THz frequency and is in use today to manufacture a large portion of existing THz products [53]. Over the years, CNC milling precision has improved significantly, and typical machining tolerances are on the order of $\pm 5\text{--}10\text{ }\mu\text{m}$ [54]. Additionally, with the advancement of micro tooling, milling tolerance can go down to $\pm 2.5\text{ }\mu\text{m}$, while offering 5- μm -wide channels and aspect ratios 10:1, and can fabricate components that can operate at THz frequencies [55, 56].

However, CNC is a serial process and at a higher frequency, the cost of the process increases along with the complexities. Also, in the case of CNC milling, the lower the required precision value, the higher becomes the machining time and hence the higher the manufacturing cost. Moreover, to define waveguide cavities, components are inevitably fabricated from two or more parts which introduce additional challenges such as alignment, and sufficient surface flatness to ensure good contact between the split blocks. Additionally, above 500 GHz when the thicknesses of the metal blocks go down below 3 mm, it is challenging to maintain adequate flatness [57].

The surface roughness of the machined piece is typically 600 nm and is quite high for THz frequencies [58]. However, by using a high-precision CNC machine and after polishing the fabricated device, the measured average roughness (Ra) can go down to a value of 200 nm [56]. CNC milled waveguide components form a large part of all THz systems in use today across both industrial and academic sectors due to the availability of the required tools and infrastructure and the lack of compelling alternatives. Figures 2.1a and 2.1b show two waveguide components manufactured by CNC milling.

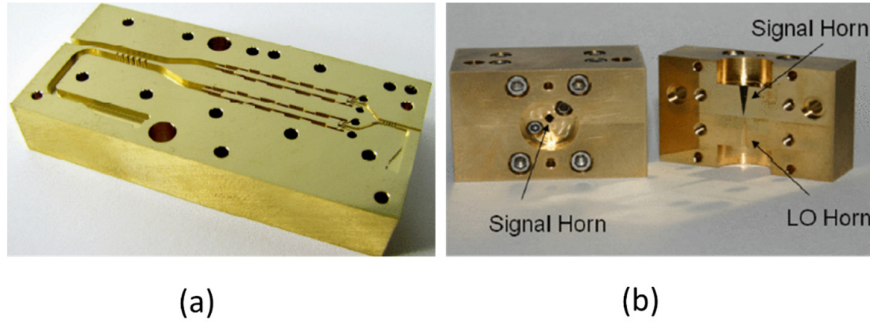


Figure 2.1: (a) CNC milled waveguide component for use at 260 GHz [54], (b) a 1.5 THz balanced HEB mixer with integrated feed horns [54].

2.2 3D Printing

Recently, additive manufacturing (AM) or 3D Printing (3DP) has opened new opportunities to fabricate THz frequency waveguide components, due to their low weight, reduced cost, and compatibility with complex geometries [59-63]. This process gives flexibility to designers by allowing for the fabrication of three-dimensional structures via selective deposition of both conductive and nonconductive materials. Non-metallic 3D printed parts are lightweight but lack mechanical robustness. A H-band (220–325 GHz) waveguide and a diagonal horn have been demonstrated by the stereolithographic apparatus (SLA) method, with an average 0.4-dB insertion loss [64]. However, they must be printed in split pieces and require assembly after manufacturing, as well as post-processing, such as the deposition of a conductive layer.

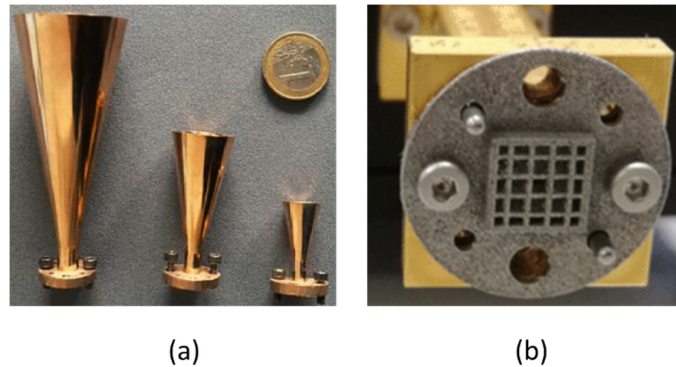


Figure 2.2: (a) 3D printed E-, D-, and H-band horns [65], (b) D-Band 3D-Printed all metal antenna [66].

On the other hand, metallic 3D printing can compensate for the drawbacks of non-metallic 3D printed devices [65]. Yet they suffer from high surface roughness which requires post processes such as manual polishing, gold electroplating to smooth the surface, or a micromachining process (MMP) [66, 67]. All those additional processes increase the cost and time of the final device fabrication. Furthermore, it is difficult to polish narrow channels and openings which causes a sharp rise in insertion loss [58, 68]. Figures 2.2a and 2.2b show images of waveguide components manufactured by 3D printing.

2.3 Micromachining

Micromachining has the potential to realize small structures with more than sufficient accuracy at a reduced cost. This technology was initially developed for the integrated circuit (IC) and the microelectromechanical system (MEMS) industry. In micromachining three dimensional (3-D) patterns are transferred to the substrate by photolithography and geometries are achieved either by subtractive techniques (bulk micromachining) or by additive techniques (surface micromachining). Bulk micromachining involves wet etching and dry etching, whereas surface micromachining involves thin film growth on the substrate [17]. Micromachining techniques have been used in different sectors, such as the semiconductor industry, for microfluidic devices and biomedical applications, sensors and actuators, and so on. The first micromachined sub-THz waveguide was manufactured in 1980 [69]. Since then, different micromachining techniques have been used to fabricate sub-THz waveguide components, some of which are presented in this section.

2.3.1 Silicon micromachining

Silicon micromachining (or silicon etching) is a subtractive process in which the pattern is transferred by chemical or physical removal of the material. Based on the substrate removal technique, etching can be categorized into wet etching and dry etching which are performed by chemical solution or by a plasma method respectively [70]. Etching can be isotropic or anisotropic. In 1980, the first dielectric component operating at sub-mm-wave was fabricated by wet etching of a silicon wafer [69]. Later this process was used to fabricate hollow metallic waveguides [71-73]. With the development of other advanced micromachining techniques wet etching process lost its popularity due to its dependency on the crystallography of the silicon wafer [74-76]. However, some recent work still has been done due to the low processing cost [77, 78].

Unlike wet etching, dry etching needs sophisticated equipment, where plasma or etchant gases are used to remove material from the substrate at low pressure (a few millitorrs) and moderate temperatures (from room temperature to 250 °C). Dry etching can be of different types:

- i) Physical dry etching, where the high kinetic energy of particle beams is used to etch the substrate.
- ii) Chemical dry etching, where chemical reactions with etchant gases attack the surface.
- iii) Reactive ion etching (RIE), where a combination of both physical etching and chemical etching is used.

Recently, the most used etching process is deep reactive ion etching (DRIE). DRIE is a bulk silicon micromachining technique based on plasma etching, where the wafer is exposed alternately to an etchant (plasma of sulphur hexafluoride, SF₆) and a passivant (octafluorocyclobutane, C₄F₈) to control the integrity of the side wall of the structure. The etching and the passivation process alternate continuously until the desired depth is achieved. The major advantage of DRIE is its ability to deliver high aspect ratio (AR) structures. The first silicon micromachined waveguide components by DRIE were demonstrated in 2004 [77, 79]. The DRIE process can deliver the fabrication of trenches with near-vertical sidewalls and can potentially manufacture an unlimited number of structures. Additionally, the DRIE fabrication technique has very low manufacturing uncertainty, which makes it attractive for the

growing field for the fabrication of THz waveguide components. A Waveguide fabricated by DRIE with insertion loss as low as 0.38 – 0.42 dB /mm at 750 - 1100 GHz has been reported [80]. Even lower insertion loss of 0.2 – 0.25 dB /mm at 750 - 1100 GHz has been achieved by using a subsequent oxidation step to smooth out etching defects [81]. Figure 2.3 presents a slot array antenna fabricated by DRIE of SOI (silicon on insulator) wafers.

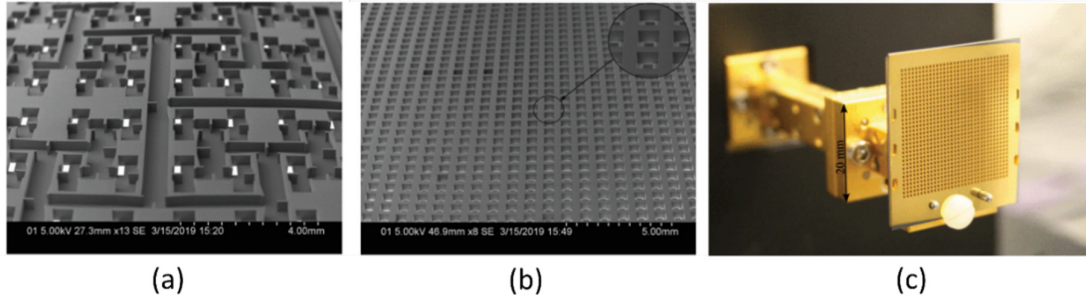


Figure 2.3: (a) SEM image of the waveguide structure and coupling slots, (b) radiating elements with a zoomed view showing the coupling slots, (c) pictures of the manufactured antennas mounted on a standard WM- 570 waveguide flange[82].

However, the process is time-consuming, expensive, and requires sophisticated and expensive pieces of equipment. Furthermore, multiple DRIE etching steps are needed to fabricate complicated structures. This technique affects the flatness of the wafer and thus the uniform resist deposition for the next DRIE process [83]. Also, sidewall under-etching, mask undercut, and sidewall scallops affect sidewall verticality, surface roughness, geometrical tolerance, and gaps inside the waveguide, which are all well-known phenomena of this process [84, 85]. A significant effect of the oxidation step has been observed and surface roughness can be reduced from 206 nm to 118 nm however this includes additional time to the final device fabrication and cost as well [86].

Despite prolonged processing time and high processing cost, the DRIE fabrication technique does provide a very low manufacturing uncertainty, which makes it attractive in the growing field of THz waveguide components fabrication, as reported in many recent papers [27, 31, 33, 35, 41, 84, 86-97]

2.3.2 LIGA method

LIGA is a German acronym for lithography, electroforming, and molding developed by Forschungszentrum Karlsruhe [98]. By electrodeposition of a metal on a polymer mold, and later by dissolving this polymer mold, a fully metallic structure can be obtained by this micromachining technique. Copper is the most used metal for the electrodeposition process. Two different types of LIGA technology are available: X-ray LIGA and UV LIGA. The X-ray LIGA process uses X-rays produced by a synchrotron to generate a high aspect ratio structure (up to 50-100:1). Example of utilizing the X-ray LIGA process to fabricate the THz component has already been presented [99]. X-ray LIGA is a very expensive process as both the installation of the X-ray synchrotron and the mask used by this process are very expensive. Figure 2.4 presents 340-GHz copper folded waveguides using the UV-LIGA method.

UV LIGA uses ultraviolet light which makes it comparatively low-cost. The fabrication steps are as follows: a thick photoresist (usually SU8, KMPR) is exposed and developed to be used as a mold for galvanofarming or electroforming. Once the photoresist mold gap is filled with filling material, the photoresist is stripped away leaving the metal structure. By using UV LIGA, structures with an aspect ratio of up to 20:1 can be achieved [100]. Several waveguide components operating at THz frequencies have been reported in the literature [101-106].

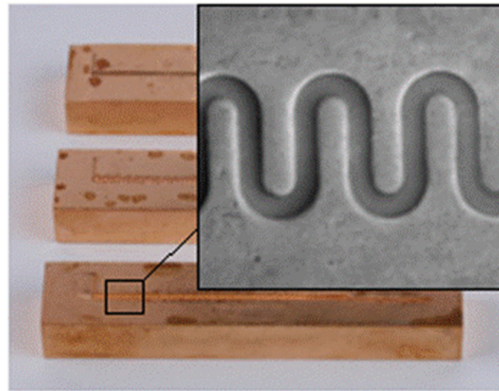


Figure 2.4: Optical microscope image of one symmetric half after the photoresist removal, lapping, and polishing [102].

One major benefit of the method is that LIGA produces metal structures, so it is easier to couple to standard metal waveguide components. Still, the process suffers from drawbacks such as non-uniformity and thus requires an additional processing step, such as lapping, to planarize the final device.

2.3.3 Photoresist-based method

Another attractive process is to fabricate waveguide components directly from permanent photoresists. Photoresist-based methods are additive processes, where layers of photoresist are spin-coated, soft-baked, patterned, and coated with metal. In the previously described LIGA process, the photoresist acts as a mold and is removed at the end of the process. In contrast, the technique presented in this section is adopted for the photoresist to remain as a part of the structure. This process can be carried out by using standard lithography tools and this is a major advantage of this technology. Among the different photoresists, SU8 has gained interest due to its ability to deliver high aspect ratio structures. Many SU8 micromachining-based waveguide components have been reported in the literature [32, 107-112].

SU8 is an epoxy-based negative photoresist developed by IBM in the late 80's [113]. SU8 photoresist is comprised of SU8 resin, a photoinitiator, and a solvent. As a negative photoresist, the regions exposed to light become insoluble in the developer. SU8 is biocompatible, rigid, thermally, and chemically stable. Additionally, it is suitable to achieve structures of aspect ratios over 25 [114] and up to 1.5 mm high using a single coating step [115]. Figure 2.5 shows an 8×8 slotted waveguide antenna operating at 220 GHz to 320 GHz based on the micromachined SU8 technology.

The main benefit of the SU8 process is that the height of the structure is not dependent on the substrate material. By adding multiple resist layers, a thicker structure can be obtained.

Additionally, depending on the geometry of the waveguide components, the fabrication process can be altered between single layer SU8 processing or multilayer SU8 processing. Also, the process does not require any sophisticated and expensive micromachining tools, which reduces the processing cost.

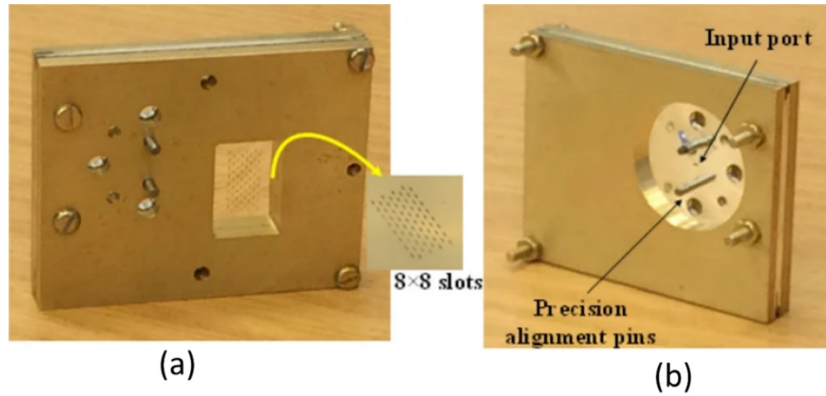


Figure 2.5: Photograph of a fabricated planar array 8×8 slotted waveguide, (a) radiating side, (b) back side [111].

However, the process suffers from significant instabilities and delamination issues between the thick resist and the carrier wafer. Additionally, while working with thick layers of photoresist, SU8 processes are very challenging to stabilize, and the layer thickness is difficult to control. Moreover, the spin-coated resist layer suffers from edge bead issues and due to stress in the photoresist, the released structure suffers from a flatness problem. Figure 2.6 shows a part of an antenna fabricated by the SU8 photoresist, that is buckled up due to the stress in the released SU8 films. Additionally, SU8 processes require longer soft baking times, and a significant amount of waiting time in between each step. Due to the prolonged fabrication process, SU8 processing is not a suitable material for batch production.

The discussions above have been dealing with liquid photoresists. There is also an UV-sensitive dry photoresist, which offers many advantages over liquid photoresist. Later in this thesis, we describe and investigate its impact and effectiveness on passive waveguide components operating at THz frequencies.

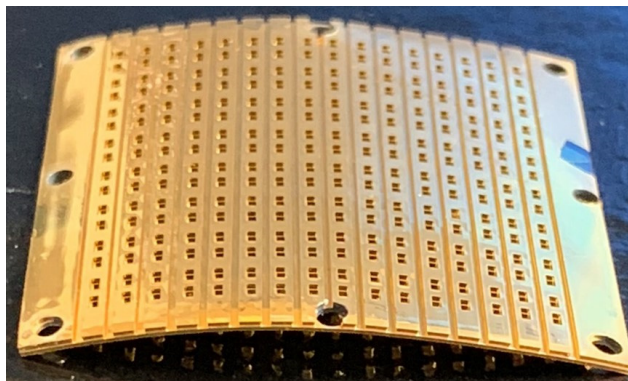


Figure 2.6: Stress-related bend in thick SU8 structure released from the substrate.

2.3.4 Surface micromachining

Surface micromachining is an additive process, where thin films are deposited above the surface of the silicon substrate. A soluble layer, which is called a sacrificial layer, is deposited underneath other patterned materials for later removal. The main purpose of this soluble or removable sacrificial layer is to temporarily support the structural layers during successive fabrication steps. This layer needs to be stable during deposition and throughout the fabrication process. Chemical wet etching is usually used to remove the sacrificial layer. Generally, metals (i.e. Au, Ni, or Al), dielectrics (SiO_2 or Si_3N_4), or polymers (photoresist) can be used as sacrificial layers. Waveguide components operating from millimeter wavelengths up to the THz frequency range have been fabricated by surface micromachining [116-119]. Due to its ability to deliver fully metallic structures, the integration of surface micromachined components with other technologies is straightforward. Also, very complicated 3D structures can be obtained by this technology.

2.4 Challenges and Motivation

The above-mentioned micromachining processes are attractive and offer significant advantages to overcome the fabrication challenges faced by traditional CNC milling. Nevertheless, work is needed for the advancement of microfabrication methods to fabricate low-cost and high-performance waveguide components operating at the THz frequency band. From the discussion presented in Chapter 1 and Chapter 2, a fabrication process should offer the following benefits:

- ***Fabrication tolerance*** – targeting feature size accuracy and low surface roughness.
- ***Process complexity and time*** – to reduce the number of processing steps.
- ***Process scalability*** – to offer batch production.

The waveguide components developed in this thesis are mainly polymer based as they offer a cost-effective and simple fabrication process compared to other methods. In an attempt to provide a solution to the existing microfabrication methods and target a cost-efficient solution, two different polymer-based microfabrication methods have been developed and investigated in this thesis. These two different methods are:

- i) Template-based injection molding method
- ii) SUEX dry film photoresist-based method

Paper I is focused on a template-based injection molding process where the time-consuming part of the microfabrication needs to be done only once. The device fabrication by molding is straightforward, scalable, and fast. The details and results of the fabrication method are presented in Chapter 4.

Paper II – Paper V are focused on the SUEX dry film photoresist-based method. This offers rapid fabrication of waveguide components without using sophisticated tools. The measurement results presented in the thesis indicate that this dry film-based approach is a promising method for fabricating waveguide components operating in THz frequency ranges. The details and results of the SUEX fabrication are presented in Chapter 5.

Chapter 3

Overview of Gap Waveguide Technology

This chapter presents an overview of gap waveguide technology by describing the fundamental operating principle of this technology. Additionally, the application of gap waveguide technology to evaluate passive components, array antennas, and packaging on all possible variants of gap waveguide technology is summarized in this chapter.

3.1 Fundamentals of Gap Waveguide Technology

The gap waveguide technology was introduced following the earlier studies on *hard* and *soft* surfaces and the cutoff of electromagnetic waves on a parallel perfect electric conductor (PEC) and perfect magnetic conductor (PMC) waveguide configuration [120, 121]. The gap-waveguiding concept is based on controlling the propagation of electromagnetic waves in desired directions inside a parallel-plate waveguide by using fundamentals of boundary conditions. The terminologies hard and soft surfaces come from acoustic theory, where, a soft surface damps the acoustic wave, and a hard surface allows propagation of the acoustic wave. In electromagnetic field theory, the PEC/PMC parallel-plate condition acts as the stop surface and does not allow any propagation of mode within a certain band of interest. Similarly, the PEC/PEC configuration allows for electromagnetic wave propagation.

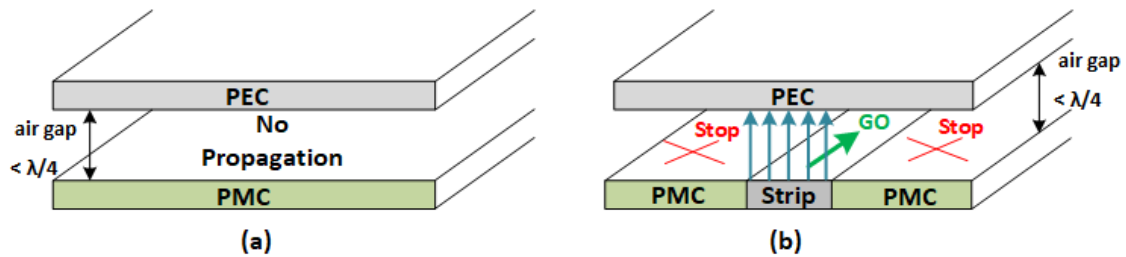


Figure 3.1: Basic concept of gap waveguide technology. (a) PEC – PMC parallel-plate electromagnetic wave cutoff. (b) TEM local wave propagation through the strip.

To control the electromagnetic wave propagation, the gap waveguide uses the basic cut-off of a PEC-PMC parallel-plate waveguide configuration between the two parallel plates. As long as the separation between the PEC and PMC plates is less than $\lambda/4$, no wave can propagate between the plates. However, if a PEC strip is now placed on the PMC plate, the wave can

propagate along the strip. The idea is shown in Figure 3.1. As PMCs are not existing in nature, the PMC condition must be satisfied by an artificial magnetic conductor (AMC) in the form of periodic structures such as metal pins [122] or mushroom structures [123].

An AMC surface is realized from "Fakir's Bed of Nails" [122]. Metallic pins are arranged periodically in all directions on a conducting ground plane, to achieve a 2D AMC surface as shown in Figure 3.2. These pins create open circuit conditions, over a certain frequency range, resulting in the tangential magnetic field to zero at its surface with a nonzero value for the tangential electric field. Hence, this metallic pin-based surface acts as an AMC surface. An electrically conducting surface has the opposite characteristic, where the tangential electric field is zero and the tangential magnetic field has a nonzero value.

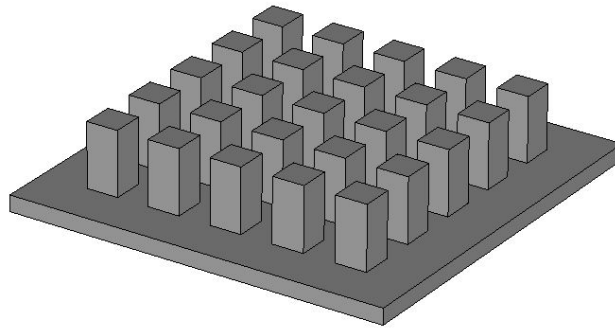


Figure 3.2: 'Bed of nails' structures by periodically placed electrically conductive pins.

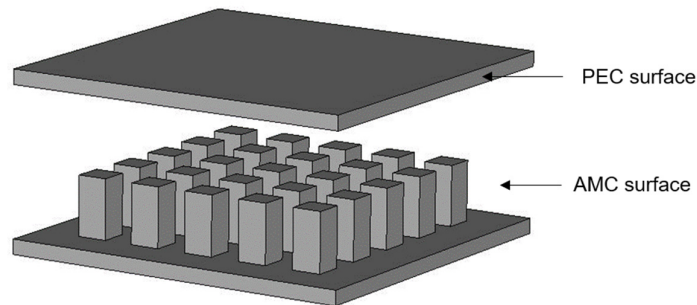


Figure 3.3: A PEC surface and an AMC surface are placed parallel to each other.

When a PEC surface and an AMC surface are placed opposite to each other and the separation between the PEC and AMC plates is less than $\lambda/4$, due to the contradicting boundary conditions, a stopband is created, and no waves can propagate in the gap between the two surfaces [124]. Figure 3.3 shows an AMC surface and a PEC surface placed parallel to each other and this case can be referred to as an ideal parallel plate cut-off case. The addition of a metal strip in the AMC layer will now allow the propagation of electromagnetic waves along the strip without being leaked away in the lateral direction. The field in the two PEC/AMC regions will decay very fast. Thus, the waveguide can be formed without the need for electrical sidewalls. Based on the guiding line, the gap waveguide can be made in different versions; strip, ridge, or groove

[26, 125, 126]. Different versions of gap waveguide structures (ridge gap waveguide, groove gap waveguide, and microstrip gap waveguide) with their supported propagation mode are presented in Figure 3.4, where periodic metal pins are used as AMC surface (Figure 3.4a, Figure 3.4b, and Figure 3.4d). There are other types of pins that can be used to attain an AMC surface, such as the mushroom with metalized vias shown in Figure 3.4c, the inverted pyramid pin, and even a spring-shaped pin [123, 127, 128]. The propagation mode of the GW is dependent on the guiding structure. The ridge gap waveguide (RGW) and microstrip gap waveguide (GGW) both support the quasi-TEM mode of propagation. On the other hand, the groove gap waveguide (GGW) supports a mode very similar to the TE_{10} mode of rectangular waveguide [129].

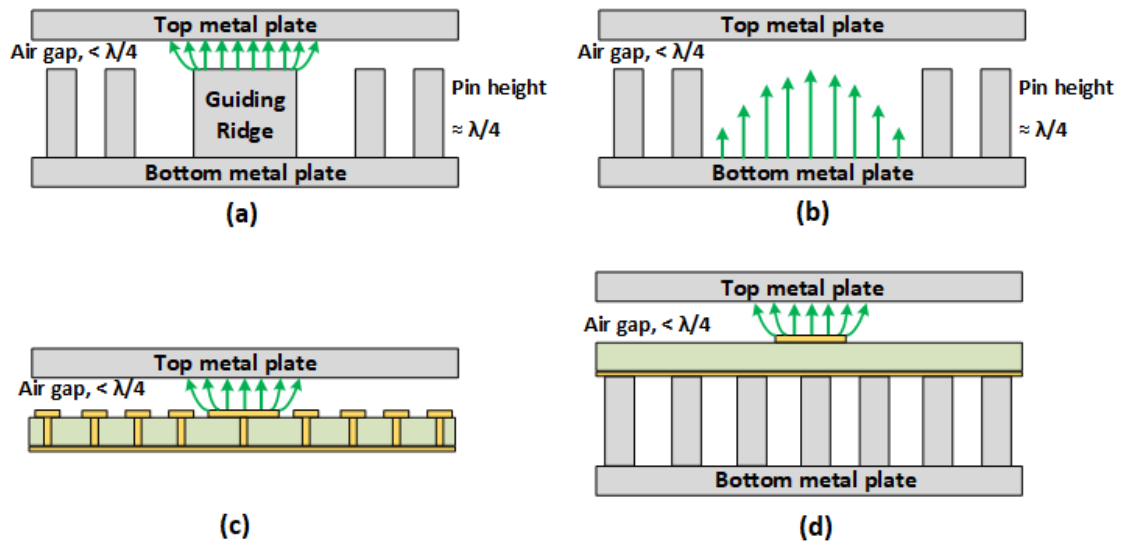


Figure 3.4: Different versions of gap waveguide geometries: (a) ridge gap waveguide, (b) groove gap waveguide, (c) microstrip gap waveguide, (d) inverted-microstrip gap waveguide [130].

3.2 Design of Parallel Plate Stopband Realized by Bed of Nails

As mentioned before, the performance of the GW is determined by the periodic texture located around the ridge, groove, or strip. Those periodic textures can create a parallel plate stopband for wave propagation in the undesired direction. While designing the stopband to obtain the lower and upper cut-off frequency of this stopband, the geometrical parameters of the periodic structure play a vital role. A generic study and performance evaluation of different periodic electromagnetic bandgap (EBG) structures in gap waveguide technology has been thoroughly evaluated [124]. The geometrical parameters that may influence the stopband of the parallel-plate waveguide are:

- The gap height,
- the height of the pins,

- the period of the pins,
- the radius of the pin and
- the lattice geometry.

3.3 Benefits of Gap Waveguide Technology for THz Applications

The GW technology offers all the benefits covered by other existing waveguide technologies, such as microstrip transmission lines, SIW, CPW, and RW. Favorable features of gap waveguide structures are the planar structure, low loss, flexible manufacturing, and low manufacturing cost, especially at frequencies higher than 100 GHz. GW structures offer low loss compared to planar transmission lines. As the wave propagates in the air, the GW has no dielectric loss. Also, they do not require any electrical connections between the metal walls. Therefore, compared with RW, it has more flexible fabrication requirements. Similarly, the semi-open configuration of the GW geometry gives more freedom in the integration of active electronic circuits with the low-loss metal waveguide.

From the point of material selection while manufacturing GW components, due to the wave propagating through the air in GW structures, they are independent of the material properties used for manufacturing. Thus, any material suitable to be used for a low-cost fabrication method can be used. The only requirement that exists in GW geometry is the metallization of the layers which must be 4-5 times thicker than the skin depth at the frequency of operation. The flexible fabrication requirement introduces new opportunities to focus on batch fabrication of gap waveguide components cost-effectively.

3.4 Applications of Gap Waveguide Technology

The benefits of GW technology have been evaluated and demonstrated and confirmed in many different applications. A summary of some previous work will be presented in this section.

i) Transitions, resonators, filters, and passive components

The GW research was started by designing several transitions working at different frequency bands, from GW to conventional transmission lines. The interface of most equipment is standard RW and most of the MMICs need microstrip or coplanar probes. Thus, new transitions are needed to connect the gap waveguide circuits with the conventional waveguide flanges and to RF MMICs. Different transitions working at different frequency bands from different variants of GW to conventional transmission lines such as RGW to RW, CPW, microstrip line, coaxial cable to RGW, GGW to RW, microstrip line, inverted-microstrip GW to RW has been demonstrated [131-139]. Figure 3.5 shows a microstrip-to-GGW transition and a RW to RGW transition.

To determine the losses of gap waveguide structures the Q-factor of resonators can be extracted. The Q-factor of RGW resonators and GGW resonators have been investigated and reported [140]. Various bandpass filters have been realized based on different varieties of gap waveguide technology. Compact bandpass filters using ridge GW, GGW, microstrip gap

waveguide, inverted-microstrip gap waveguide, and printed inverted-microstrip gap waveguide have been reported [141-155]. Also, other waveguide components such as magic-T, orthomode transducers (OMTs), and hybrid couplers have been designed at mmWave frequency range based on GW technology [156-158].

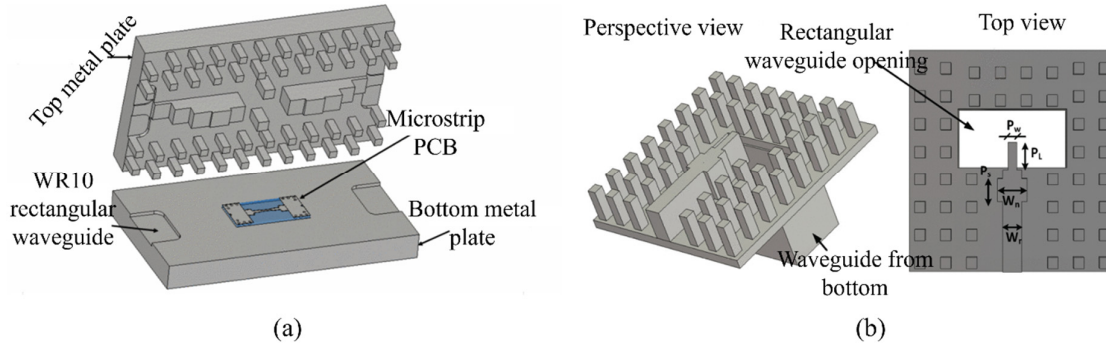


Figure 3.5: (a) A microstrip-to-groove gap waveguide transition operating at W-band [159], (b) rectangular waveguide to ridge gap waveguide transition at Ku- band [160].

ii) Planar array antennas compared to the state-of-the-art methods

GWs can propagate waves in any direction within a parallel plate and therefore are a suitable candidate to design planar array antennas with attractive features such as flat structure, low volume, and high antenna efficiency. At THz frequencies designing high gain, high efficiency and low-profile antennas are one of the main challenges.

Despite having a low profile, microstrip and SIW arrays suffer from dielectric and ohmic losses (discussed in Section 1.3.1 i and 1.3.1 iii). The problem becomes worse with the increased number of elements, where a long transmission line is required as a distribution network. Additionally, for SIW antennas the size and position of a large number of vias make the fabrication of the antenna more challenging above 100 GHz. RW or hollow waveguides show low loss and high efficiency, which make them suitable for such applications where high-gain antennas are a requirement. The challenging part is achieving a good electrical connection between each layer as the manufacturing is done by metal split blocks.

Slotted waveguide array antennas are one of the best choices for high-efficiency and high-power applications. The basic working principle is disturbing the surface current on the waveguide walls by introducing slots. As the series-fed slotted waveguide arrays provide a narrow bandwidth due to the long line effect, and single layer full corporate feed structure cannot feed each radiating element in parallel and suffers from grating lobe effect, a multilayer waveguide based corporate distribution network is the common way to design high gain antenna with a larger bandwidth. Hence, the challenging part of designing a multilayer corporate feed antenna focused on RW is to achieve good electrical contact between the vertical waveguide walls and the consecutive upper layers.

Due to the non-galvanic contact nature of GW, this technology can be used to obtain multilayer, high-gain planar array antenna. Low-loss array antennas based on ridge and groove gap waveguide corporate feed network have been demonstrated [160-170], where the feeding network was designed based on RGW or GGW configuration. Less common configurations like inverted microstrip gap waveguide, and microstrip-ridge gap waveguide, are used as

corporate-feed networks for a dual-mode horn array and multilayer SIW cavity-backed slot array respectively [171, 172].

iii) Integration and packaging

The traditional way of packaging MMICs is using metal shielding boxes, where the main drawback is the presence of cavity resonance modes when the dimensions of the box are larger than half wavelength. Additionally, surface waves in the PCB, radiation from interconnects, and standing waves along the lines, can cause crosstalk and interference problems. One way to suppress these resonances is by applying lossy absorber materials. However, this packaging approach introduces additional losses in the system. The AMC of the gap waveguide technology has been used to package circuits and suppress all unwanted fields inside the package [173, 174]. Moreover, this packaging technique has been applied to improve the performance of a coupled-line microstrip filter, SIW-GCPW bandpass filter. Also, active circuits such as monolithic microwave integrated circuits (MMIC) power amplifier chain has been packaged using the packaging solution [175-177]. A frequency-division duplex (FDD) radio front-end module has been reported, where a high-gain array antenna, a diplexer, and an RF circuit board consisting of Tx/Rx MMICs have been integrated into one single module [178]. Many simple integration techniques have also been proposed and demonstrated at different frequencies to connect GW to MMICs, and those transitions are suitable to use for single layer as well as multi-layer applications [159, 179-184].

Chapter 4

Template-Based Injection Molding

In Chapter 2 we presented different microfabrication methods to manufacture passive waveguide components operating at the THz frequency range. Several concerns and issues of such methods were also discussed. In this chapter, we will present the developed injection molding process to realize a high-gain antenna operating at the D band (110 -170 GHz). Some results presented in this section are repeated from the appended papers to improve readability.

4.1 Background

The most common high-gain antennas above 100 GHz are horn feed reflectors, microstrip patch arrays, and waveguide-based slot array antennas. However, the reflectors are bulky, costly, difficult to manufacture, and not suitable for many applications, especially when approaching the THz frequency range [185]. On the other hand, printed circuit board (PCB) technologies such as Liquid Crystal Polymer (LCP) or Low-Temperature Co-fired Ceramics (LTCC) based arrays suffer from high dielectric losses and lower antenna efficiencies [186, 187]. An alternative way to realize high-gain antennas is to use a planar array. Generally, planar antennas require multilayer structures and complicated geometry. A planar array antenna with high efficiency and gain, with low fabrication complexity and low production cost is preferable for commercial applications.

Different approaches have been taken to fabricate high-gain antennas. Among them, CNC milling, DRIE, and diffusion bonding have shown promising performance. In Chapter 2 we have already discussed the benefits and challenges of CNC milling and Si micromachining. The reported first corporate feed array antenna above 300 GHz using Si micromachining showed increased loss and narrow bandwidth [188]. However, considering the fabrication tolerance in the design later Si micromachined corporate feed array has been demonstrated to have satisfactory performance [82]. On the other hand, in diffusion bonding, a multi-layer structure is formed by the stacking of etched metal plates in vacuum at high temperatures (around 1000 °C with precise thermal control) and high mechanical pressure. This process requires several fabrication steps and specific conditions which make it an expensive serial manufacturing technique. Most of the mentioned fabrication methods are time-consuming and a fabrication method with a focus on high fabrication accuracy, low fabrication complexity, processing time, and cost is needed. Table 4.1 lists some state-of-the-art fabrication methods to fabricate high-gain antennas.

Table 4.1: State-of-the-art fabrication method to realize high gain antenna at THz frequency band.

Ref	Technology	No of Elements	Frequency, GHz	Max. gain dBi	Efficiency%
[189]	CNC, GW	16×16	94	30	-
[190]	CNC, GW	16×16	164	30	50
[191]	PolyStra process, RW	10	150	14	63
[187]	LTCC, SIW	40×32	140	32	35
[192]	LTCC, SIW	8×8	140	20	35
[186]	PCB	32×32	94	28.8	24
[193]	Diffusion bonding	32×32	120	37	55
		64×64	120	43	50
[188]	Si micromachining	16×16	350	30	-
[82]	Si micromachining	16×16	340	32	70
		32×32	340	38	60
Paper I	Template-based injection molding	16×16	140	31	53

4.2 Motivation

SU8 is one of the most used liquid photoresists and it offers many attractive features, but also has several challenges mentioned in Section 2.3.3. One major issue of SU8 fabrication is the flatness problem. Optimizing the hard baking process can result in an optimally flat structure. In our experiment, the released structure was pressed between two wafers during the hard baking process and the hard baking was done at 165 °C for 15 minutes on each side. Nevertheless, applying pressure to the structure during hard baking can cause damage to any features such as pins, steps, and overhanging structures so this is not an effective solution for all cases. Additionally, due to the many processing steps, the necessity of introducing a waiting time between two steps, and the very long soft baking time for thick photoresists, the fabrication process becomes prolonged and makes the SU8 an unsuitable material for batch production. Considering the challenges faced by the SU8 fabrication method and the need to implement new fabrication techniques, two different microfabrication methods have been developed. The process presented in Paper I is a combination of three main microfabrication techniques: fabricating a master by using the SU8 photoresist, fabrication of the PDMS mold, and injection molding of OSTEMER.

GW technology offers many benefits over other WG technologies and has been discussed in Chapter 3. The fabrication method is designed to fabricate a slot array antenna designed by gap waveguide technology. The antenna was designed to operate at the D band. A complete 16×16 slot array antenna consists of in total of 64 sub-arrays. The antenna consists of three separate conductive layers: a slot layer, a cavity layer, and a feed layer. The slot layer contained radiating slots and corrugations between the neighboring slot elements. The cavity layer was placed above the feeding layer and the electromagnetic energy was coupled from the feed layer to the cavity layer by the coupling slots. The feeding layer consisted of sixty-three 3-dB power dividers cascaded one after another. The dimensions of important parameters of this array geometry were mentioned in Paper I. The developed fabrication process is suitable to fabricate multilayer antennas with complex features. A schematic of the fabrication process for the above-mentioned device is shown in Figure 4.1.

4.3 Challenges

The following challenges have been addressed considering the slot array presented in Paper I.

Fabrication tolerance and repeatability: Meeting the required tolerance is very critical for this specific antenna, as the design has a geometrical dependency on the process parameters. Due to having features of multiple heights in each layer, the photoresist patterning method should be optimized carefully to obtain the thickness of the various layers as accurately as possible. Also, each step should be possible to perform with standardized tools and routines to assure the repeatability of the process.

Alignment of features: As the three layers of the antenna have been fabricated separately and later mounted together, misalignment between the various parts can lead to severe performance degradation. An accurate, and repeatable alignment method to avoid misalignment, is required.

Challenges

Process complexity and time: The fabrication requires many processing steps due to the complex geometry of the antenna and due to multilayer structures. Therefore, the fabrication process should comprise as few steps as possible.

Process scalability: The method should focus on batch fabrication of the device. This can be achieved by fabricating multiple pieces in the same batch or by adopting a fabrication method that can be very fast and straightforward.

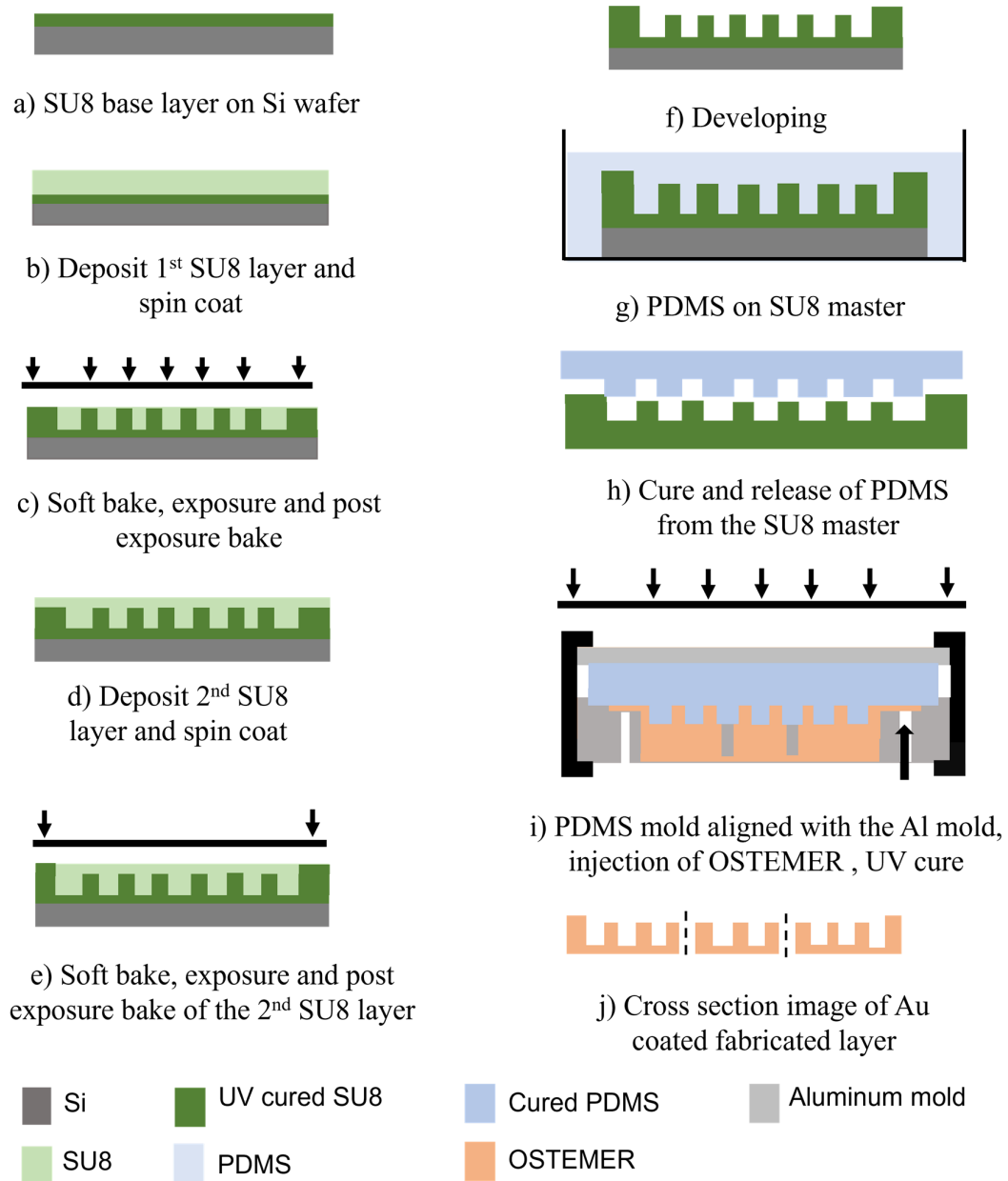


Figure 4.1: Schematic of the template-based injection molding process: (a-f) fabrication of SU8 master, (g-h) fabrication of PDMS mold, (i-j) Injection molding of polymer OSTEMER.

4.4 Materials and Method

4.4.1 Master fabrication by SU8 photoresist

The master fabrication process steps involve common SU8 lithography steps such as soft baking of the thick SU8 photoresist, photolithography of the photoresist, post-exposure baking (PEB), development of the photoresist, and hard baking. To fabricate the SU8 master two different SU8 photoresists were used. SU8 2035 was used to achieve structures smaller than 110 μm and SU8 2150 was used to achieve structures greater than 110 μm considering the viscosity of the specific photoresist. All the SU8 masters were comprised of a base layer made of SU8 2035. The slot array antenna has three separate layers: a slot layer, a cavity layer, and a feed layer. Each layer was fabricated in a separate process and the fabrication process was optimized for each layer, depending on their geometries, and the height of the pins.

The slot layer consists of radiating slots of 750 μm depth and corrugation of 490 μm depth and was hence fabricated in two steps. The first step was designed to obtain the slot heights until 260 μm , no corrugation was defined at this point. The remaining part of the radiating slot depth was added while defining the corrugation.

The cavity layer is comprised of cavity slots, cavity pins of height 644 μm , and spacers of height 750 μm to define the air gap between the cavity layer and the slot layer. The cavity master only included the cavity pins and spacers as the cavity slots were defined later during injection molding using an aluminum mold. The fabrication was divided into two steps, where the first step defines the pins and partial height of the spacers, and the second step was optimized to achieve the remaining height of the spacers.

The feed layer consists of the ridge, feed pins, and spacers. The ridge was designed with a step to provide good impedance matching during the transition from ridge gap waveguide to WR 6.5. The first photolithography step defined the partial height of the ridge, pins, and spacers, while the remaining height of the ridge and feed pins and the partial height of the spacers were added in the later steps. Finally, the remaining height of the spacers was defined during the final spin coat.

After defining all the structures required by the specific layer, the SU8 was developed and hard-baked. Later these SU8 masters were used to fabricate PDMS molds, and the fabricated masters are reusable. The detailed master fabrication method was presented in Paper I. Figure 4.2 shows the image of the fabricated masters.

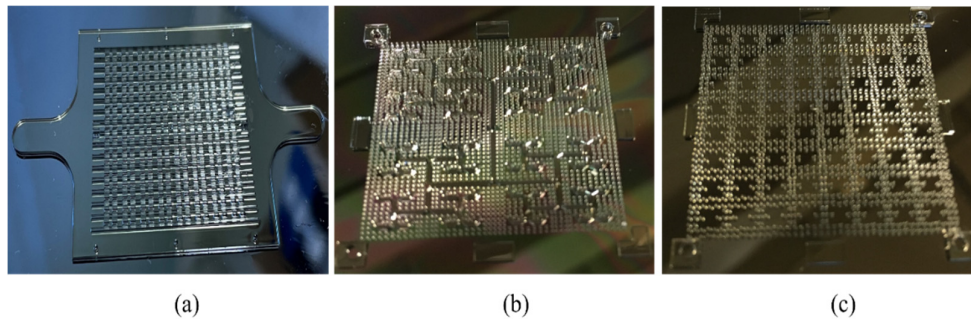


Figure 4.2: Image of SU8 masters, (a) slot layer, (b) cavity layer, (c) feed layer.

4.4.2 PDMS mold fabrication

Polydimethylsiloxane or PDMS is the most used elastomer in the rapid prototyping of MEMS devices because of its simple fabrication procedure. The low viscosity of PDMS allows it to spread over large areas and the cured PDMS can be removed from the masters easily due to its elasticity. Moreover, the straightforward processing of PDMS, short processing time, chemically inertness, and durability make it attractive for soft lithography. PDMS is composed of a two-part heat-curable mixture, a polymer base, and a curing agent. Usually, the prepolymer and the curing agent are mixed in a 10:1 ratio in weight. Different chemical and mechanical properties of the final mixture can be obtained by varying this ratio. After pouring the PDMS prepolymer into the master, the master filled with PDMS was kept in a vacuum chamber to release the trapped bubbles and later heat cured at 80 °C for three hours.

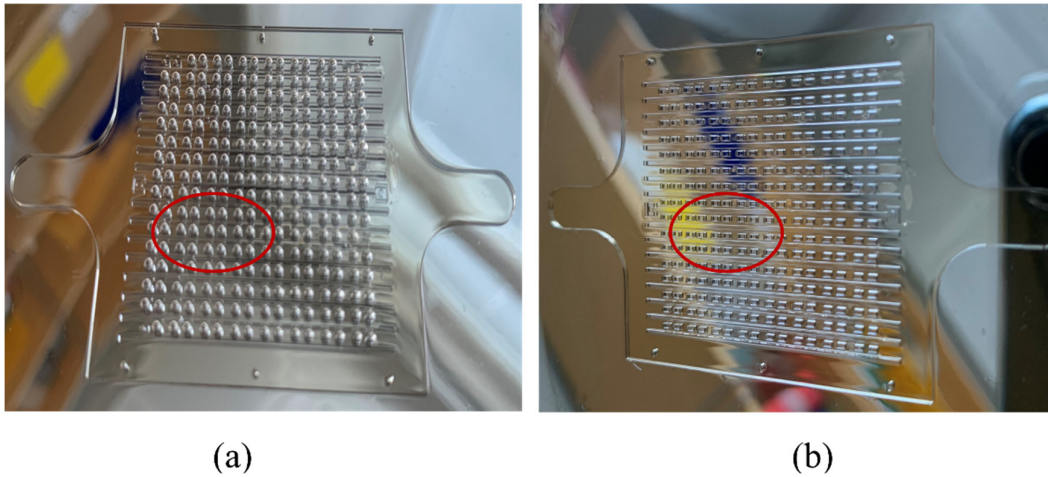


Figure 4.3: Fabrication of PDM mold for the slot layer, (a) before toluene treatment, (b) after toluene treatment.

Fabrication of the PDMS molds for the cavity layer and the feed layer was a straightforward process. However, the PDMS mold fabrication of the slot layer proved to be more challenging and needed some process optimization. The narrow opening of the slot made it difficult for the thick PDMS solution to enter through the slot openings. Figure 4.3 shows the result of the heat cured PDMS mold for the slot layer. The released PDMS mold should contain pins, but the figure shows that instead of pins it formed some bubble-type texture, but close inspection shows that bubbles were formed at the holes (Figure 4.3a). This is due to the trapped air bubbles caused by the high surface tension of the SU8. To overcome this issue, we used a toluene solution to reduce the surface tension of the SU8 structure, allowing the high-viscosity PDMS to flow into the narrow slot openings. The slot master was treated by dipping it in toluene for 2 minutes and then drying it with a nitrogen gun before dispensing the PDMS. Figure 4.3b shows the image of a heat cured PMDS mold after toluene treatment. The mold was later combined with an aluminum mold and used for injection molding.

4.4.3 Injection molding of OSTEMER

For injection molding, off-stoichiometry thiol–enes-epoxy (OSTEMER) polymers were used. It is a new type of thermosetting polymer developed specifically for microfabrication [194]. Due to its attractive features, OSTEMER becomes a promising material for microfluidic applications [194, 195]. The viscosity of OSTEMER makes it a suitable material for reaction injection molding [196]. Reaction injection molding is a process where the thermosetting polymer is injected inside a mold [197]. The curing reaction takes place inside the mold. In this process, the injecting material can be kept at room temperature. Once the material is hard after UV curing it is ejected out of the mold. This is a straightforward process and requires minimum lab facilities [198]. It has been reported that OSTEMER showed good adhesion with gold (Au) [199], thus it could be a suitable material for RF application.

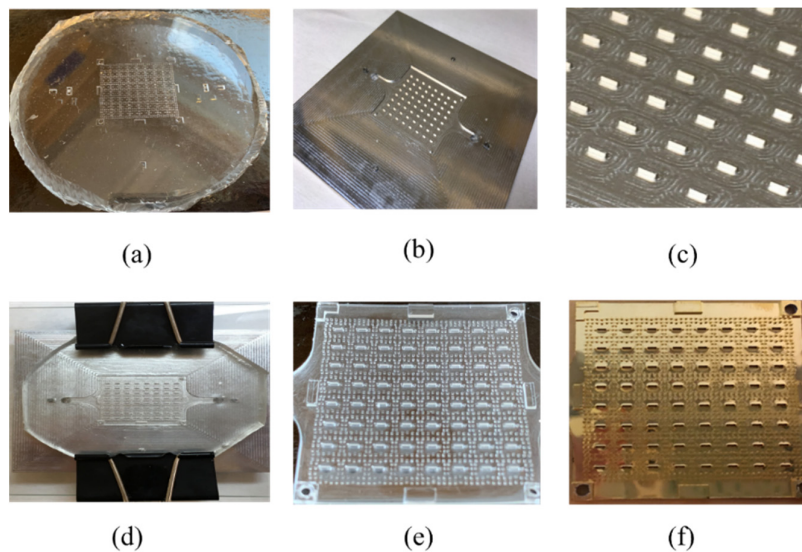


Figure 4.4: Injection molding steps for the cavity layer. (a) PDMS mold for the cavity layer, (b) aluminum (Al) mold, (c) closed image of the milled Al piece showing the pins to create the cavity opening after injection molding, (d) PDMS mold on top of the aluminum mold, ready for injection molding, (e) cavity layer made of OSTEMER after UV exposure and heat cure, (f) cavity layer after conductive layer deposition.

OSTEMER can be cured by UV exposure. Another attractive feature of OSTEMER is that after complete polymerization (by UV), the polymer contains unreacted thiol or allyls groups, which can be used later for direct surface modification or bonding [200]. The OSTEMER can be selected to provide a very stiff and flat surface. Also, it does not shrink during curing, so no shrinkage effect of OSTEMER needs to be considered while designing the mask for the master mold.

The following steps were taken during the injection molding process:

- i) aligning the PDMS mold with the corresponding Al mold,
- ii) maintaining the mold in a vacuum chamber to induce degasification,
- iii) injecting the OSTEMER pre-polymer,
- iv) exposing the mold to UV light to cure the material,

- v) removing the mold from the Al mold, and
- vi) heat curing.

The Al mold for the slot layer was flat, as the entire structure was defined in the SU8 master and transferred to the PDMS mold. Conversely, the Al mold for the cavity layer and the feed layer featured pins that defined the coupling slots and openings in the feed network layer, respectively. A more in-depth explanation of the injection molding process can be found in Paper I. The heat-cured pieces were first coated with titanium (Ti) and gold (Au) by sputtering and later coated with Au by electroplating, resulting in a 1.1 μm thick layer of Au layer. Figure 4.4 shows the steps used in the injection molding of the cavity layer.

4.5 Fabrication of 140 GHz Slot Array Antenna

To fabricate the antenna two different ways have been tried out. The methods will be discussed in this section.

4.5.1 Method I

The method involved fabricating the slot layer using SU8 and the cavity layer and feed layer via a template-based injection molding process. The geometry of the slot layer was straightforward and could be easily produced using the SU8 method. However, the complex structures of the cavity layer and feed layer made them more challenging to produce with SU8, leading to the choice of using the template-based injection molding method. The process schematic is illustrated in Figure 4.5.

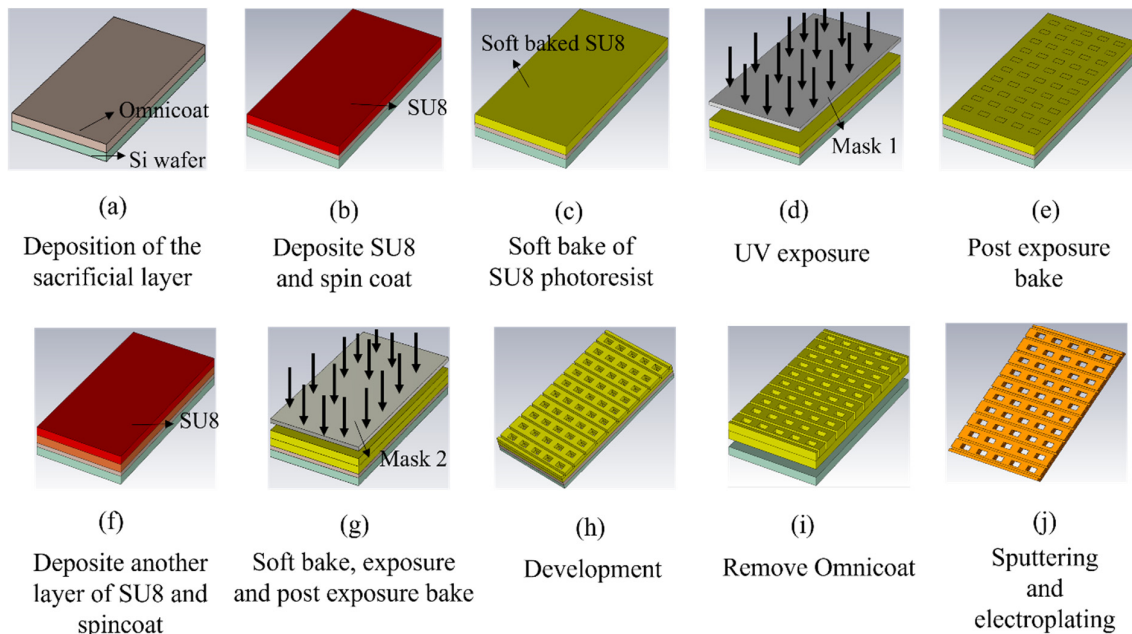


Figure 4.5: A schematic process plan to fabricate the SU8 slot layer.

To fabricate the slot layer using SU8, the process steps for producing a slot layer master were followed, with the addition of depositing a sacrificial layer on the Si wafer. Omnicoat was used as the sacrificial layer and was deposited on the Si wafer through spinning, followed by a soft bake at 200 °C for 1 minute. The rest of the fabrication process was like the slot layer master fabrication process described in Section 4.4.1. After the layer was released from the wafer, a hard bake at 165 °C was conducted, followed by sputtering with Ti and Au and electroplating with a 1.1 μm thick layer of Au to make the layer conductive.

The measurement results shown in Figure 4.6a exhibit a peak at 145 GHz in the reflection coefficient of the prototypes. This peak in S_{11} at 145 GHz may be a result of impedance variations in the feed line due to misalignments among the different antenna layers. Different shrinkage rates of different materials could contribute to these misalignments, as SU8 does not shrink during curing while PDMS is known to shrink during the curing process. Despite compensation for PDMS shrinkage, some misalignments still occurred between the slot layer, cavity layer, and feed layer. As these variations are random process variations, the only way to avoid these is to optimize the fabrication process to minimize the misalignments.

4.5.2 Method II

To address the complications introduced by different layers being made of different materials, all three layers were fabricated using template-based injection molding. This change in the fabrication process improved the S_{11} performance of the antenna over the 132-152 GHz band, as shown in Figure 4.6b. The simulation of the complete 16×16 element antenna array showed an S_{11} level well below -11 dB over the desired frequency range of 135-150 GHz. The radiation pattern and gain of the array antenna, fabricated using method II, were measured in an anechoic chamber and compared to the simulated results, as presented in Paper I. The measured patterns showed good agreement with the simulated patterns. The improved S_{11} indicated that a reduction in the misalignment between layers improves the performance.

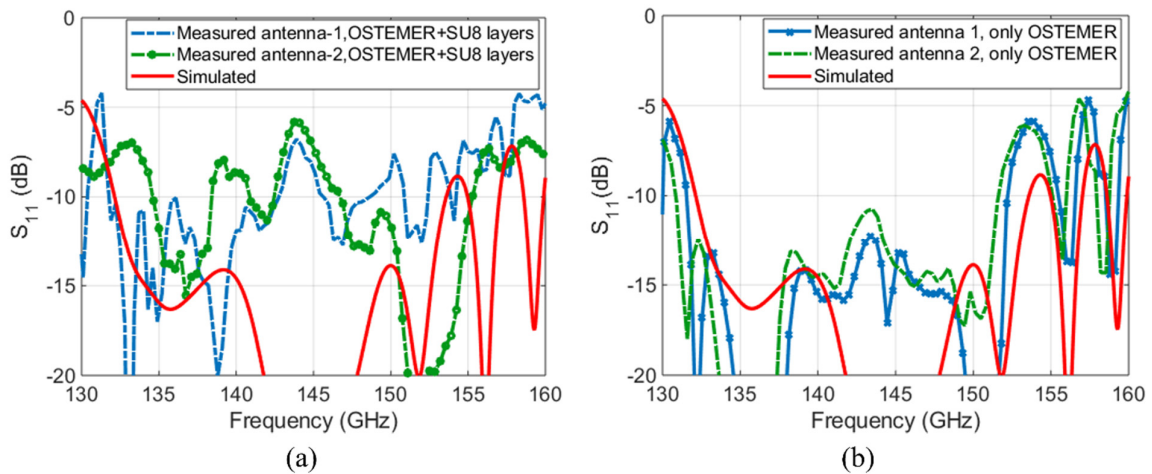


Figure 4.6: Simulated and measured S_{11} for the 16×16 element antenna array. (a) The slot layer was made of SU8, the cavity layer, and the feed layer was made of OSTEMER, (b) all layers were made of OSTEMER (Paper I).

4.5.3 Results and Discussion

The fabricated antenna can be seen in Figure 4.7. The input reflection coefficient was measured to be below -11 dB over a 14 % bandwidth from 132-152 GHz, and the antenna gain was measured to be 31 dBi at 140 GHz, both of which are in good agreement with the simulations.

To understand the slight discrepancy between the simulation and the measured S_{11} , the impact of shrinkage on the antenna's S_{11} performance was analyzed using CST microwave studio. It was observed that shrinkage of the cavity layer, while the rest of the layers remain at their original size, has the most critical effect on the performance of the antenna. Another simulation was also conducted to understand the effect of similar shrinkage or expansion on all three layers. The simulation results indicated that when all layers experience a similar amount of shrinkage or elongation compared to the optimized antenna dimensions, the operational bandwidth of the antenna shifts towards higher frequency or lower frequency, respectively (details can be found in Paper I).

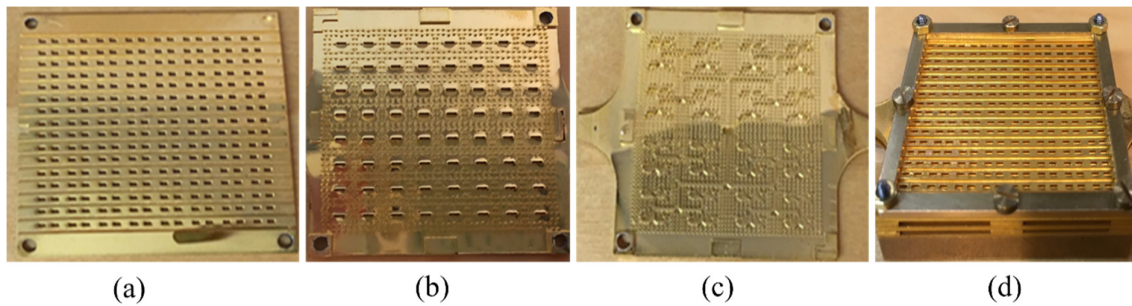


Figure 4.7: Fabricated antenna, (a) slot layer, (b) feed layer, (c) cavity layer, (d) complete antenna mounted on the milled base plate.

Accomplishments

Fabrication tolerance and reproducibility

The developed process shows sufficient fabrication accuracy within the limit of 1.5 % in the longitudinal direction which is good compared to the height of the structures. Most of this is translated from the SU8 master, and this can be improved. However, for this specific antenna and the operating bandwidth, this fabrication tolerance is satisfactory. The same master can be used multiple times to fabricate the PDMS mold, and the fabricated PDMS mold is also reusable. Therefore, the fabricated device is reproducible.

Process complexity and time

The developed fabrication process is designed in a way that the time-consuming and complicated processing steps need to be done only once. As stated, the fabricated SU8 master is reusable and can be used multiple times. Therefore, this process is suitable for the fabrication of complicated structures. The injection molding process and metallization of the molded parts can be completed effortlessly in a regular environment in a very short period. This will result in a high throughput of the devices, thereby reducing the cost significantly. A flow chart of the fast fabrication process is shown in Figure 4.8.

Process scalability

The developed method is suitable for batch fabrication as the final chip fabrication has been done by injection molding, which is a very common method of batch production of microfluidic devices [201, 202]

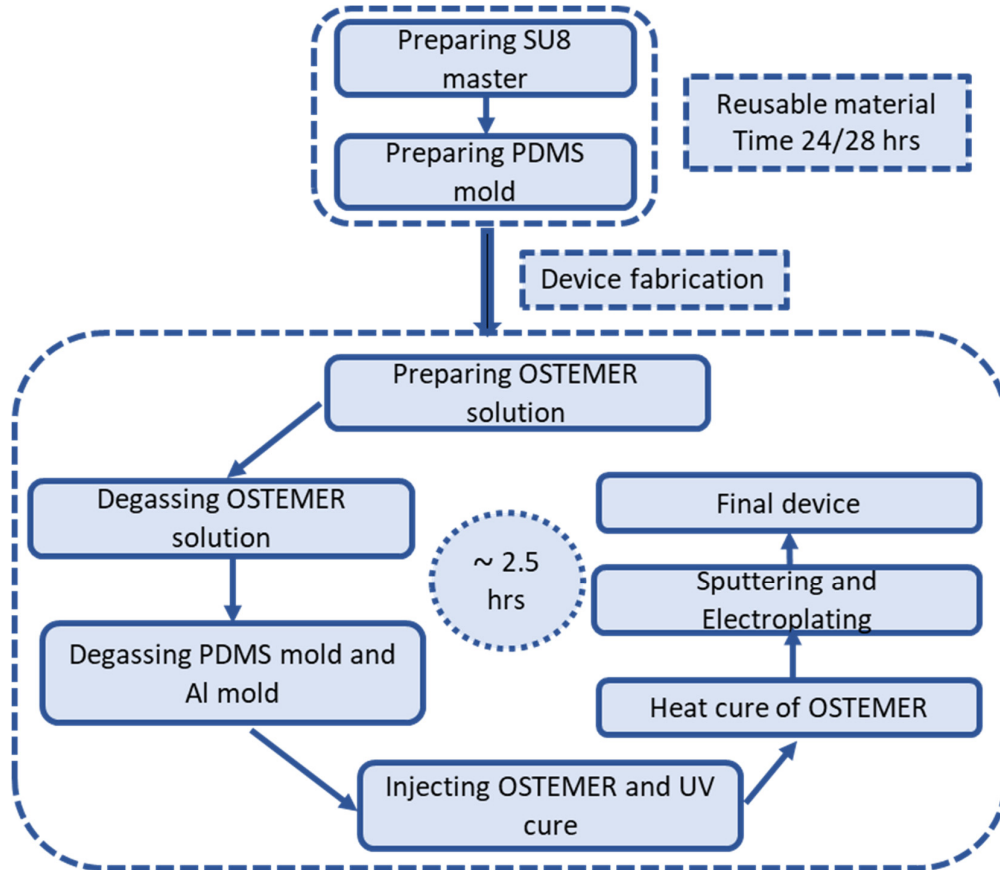


Figure 4.8: Flow chart of the fast fabrication process.

Limitations

Alignment of features

One major issue that needs to be addressed later is the alignment of the features. The reasons for misalignment between different layers are the following:

PDMS shrinkage compensation error

Calculated PDMS shrinkage was $1.4 \pm 0.1\%$ indicating a measured error of approximately $\pm 32 \mu\text{m}$ across the total dimension of each layer. As Figure 4.6b shows that the S_{11} has slightly shifted towards lower frequency, thus considering the simulation results of all layers experiencing a similar amount of shrinkage or elongation, we assume the PDMS shrinkage was somewhat overcompensated.

Alignment error between the PDMS mold and aluminum mold for the cavity layer and the feed layer

Another misalignment was introduced between the cavity PDMS mold and the cavity Al mold. The partial structure of the cavity layer was fabricated by the cavity master, while the remaining part of the cavity layer was transferred by the Al mold. To fabricate the complete cavity layer, the PDMS mold and the Al mold needed to be placed together. This was a manual process, which might introduce some misalignment. Additionally, the calculated PDMS shrinkage error of approximately $\pm 32 \mu\text{m}$ may have contributed to the alignment error between the cavity pins and cavity openings. The misalignment between the cavity PDMS mold and the cavity Al mold is presented in Figure 4.9.

Alignment error while mounting all three layers in the base plate

Moreover, during measurement, the three fabricated layers were placed on a base plate using four guiding pins and screws, which could have introduced some rotational error.

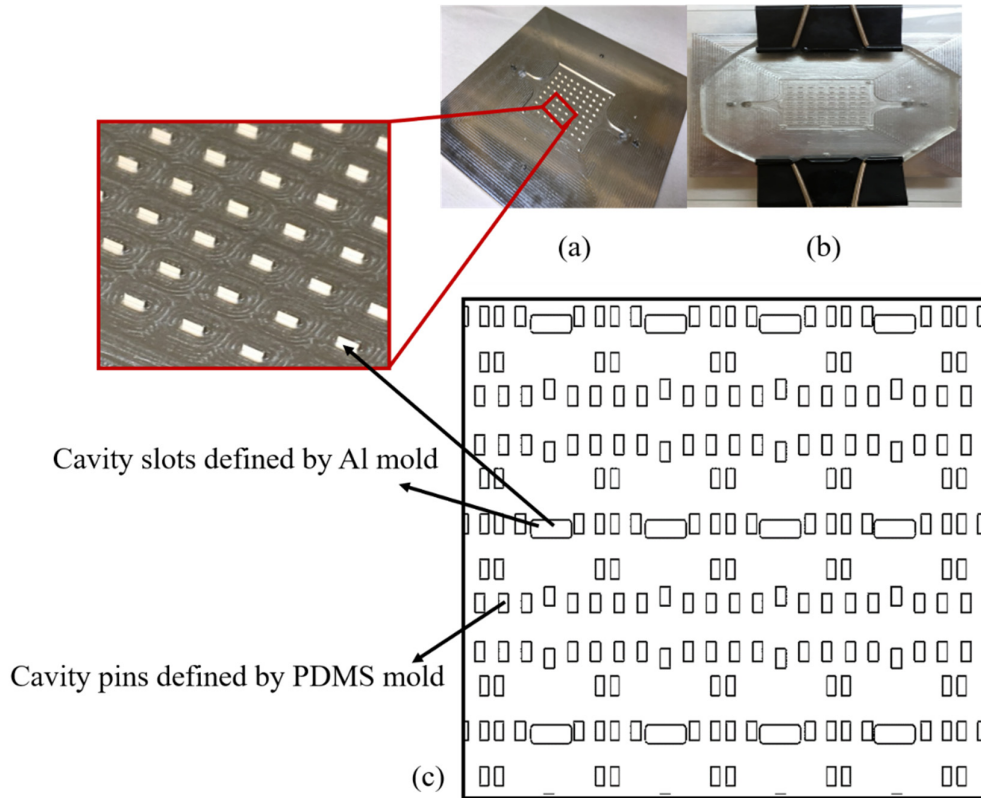


Figure 4.9: Misalignment between PDMS mold and Al mold. (a) Al mold for the cavity layer, (b) placing PDMS mold with the aluminum mold for injection molding of OSTEMER, (c) schematic of misalignment that happened during placing two molds.

Chapter 5

Dry Film Photoresist-Based Method

This chapter will be focused on describing the SUEX dry film photoresist-based fabrication method. The process optimization, the fabricated devices, and comparison to the state-of-the-art manufacturing will be presented along with the fabrication challenges.

In the process presented in Paper II, Paper III, Paper IV, and Paper V, SUEX dry film photoresist was used to fabricate gap waveguide structures. Among the different dry film photoresists, SUEX is a suitable material to achieve high aspect ratio structures by lithography [203]. SUEX dry film photoresist has been used to fabricate different types of structures to evaluate their usefulness for THz frequency device applications.

5.1 Motivation

The benefits and challenges of liquid photoresists were mentioned in Section 2.3.3. In Paper I we presented the challenges of using SU8 photoresist for thick structures; very long baking time, long waiting time between each step, and stress-related bending are the major issues that have been presented and discussed in Paper I. As a solution to these issues, SU8 was used as a molding material, where the final device can be fabricated in a comparatively short time and also no need to think of bending after releasing from the substrate. Yet, SU8 mold fabrication needs some extra care to overcome the fabrication issues, and the process is very time-consuming.

Additionally, ensuring sufficiently planar distribution of the resist, optimizing the soft baking time and temperature to bake the photoresist properly, and optimizing processes to achieve the required thicknesses all need quite some effort for a particular design and are unavoidable. Therefore, it will be interesting to investigate a new material that can be used as a device material along with offering a straightforward and time-efficient fabrication method. At this point, a dry film photoresist can be a suitable substitute. The advantages offered by dry film photoresists are

- i) no edge bead,
- ii) a high degree of thickness uniformity over the whole wafer,
- iii) fast processing, no need for soft baking,
- iv) straight sidewalls,
- v) requiring less sophisticated tools,
- vi) overall lower fabrication cost.

5.2 Challenges

The following challenges need to be considered when fabricating the THz passive waveguide components by utilizing SUEx dry film photoresist:

Fabrication tolerance: For a novel fabrication method it is very important to know that the fabrication process meets the tolerance requirement at THz frequencies. This includes feature size control as well as the verticality of the waveguide side walls, pins, and other fabricated structures.

Reproducibility of the developed process: The fabrication process must be repeatable. This includes fewer processing steps, less dependency on the fabrication tool, and less need of using sophisticated tools.

Surface roughness of the fabricated device: The fabricated waveguide components are covered with metal. However, the surface roughness of the fabricated structure is very important at the THz frequency range. Therefore, the expected surface roughness of the fabricated device needs to be very low.

Delamination of separately patterned layers: The dry film process is based on the lamination of multiple dry films on top of each other. Delamination of the separately patterned layers can be a major challenge of this process, especially for devices where multilayer structures are required.

Geometrical simplicity: Keeping the geometrical complexity low, is one of the most important considerations while investigating a new fabrication method. This will help to investigate the fabrication process and solve the fabrication issues thoroughly. One way to make the electromagnetic design simple is to minimize the number of steps in a design and to avoid large AR structures.

5.3 Material and Method

Dry film photoresists were invented almost 50 years ago and since then, they have been widely used in the production of printed circuit boards (PCBs) [204]. They come as sheets of negative-acting material without solvent and in pre-defined thicknesses sandwiched between two polyethylene (PET) sheets. The middle layer is a photosensitive layer. Generally, a photosensitive layer consists of monomers, photoinitiators, polymer binders, and some additional additives such as adhesion promoters and dyes [205]. Monomers are the main components of a dry film, which is initially solvable in the developer and becomes unsolvable after UV light exposure and heat treatment. Dry films are laminated on top of a substrate by hot roll lamination and have already been used for several MEMS applications and they offer many advantages over liquid photoresists [206-209].

Different types of dry film resist have been used commercially: Riston, Ordyl BF410, Etertec 5600, DF 4615, and DFR-15 [210]. Recently SUEx dry film photoresist has proven itself a promising material for micro- and nanofluidic applications [211]. SUEx is a cationically cured modified epoxy formulation using an antimony-free photo acid generator (PAG). An aspect ratio of 15:1 has been reported for SUEx structures [212]. The general dry film lamination process is shown in Figure 5.1.

The general processing steps for dry film fabrication is

- i) lamination of the dry film,
- ii) post lamination bake (PLB),
- iii) exposure,
- iv) post-exposure bake (PEB),
- v) development of the photoresist,
- vi) hardbake,
- vii)conductive layer deposition.

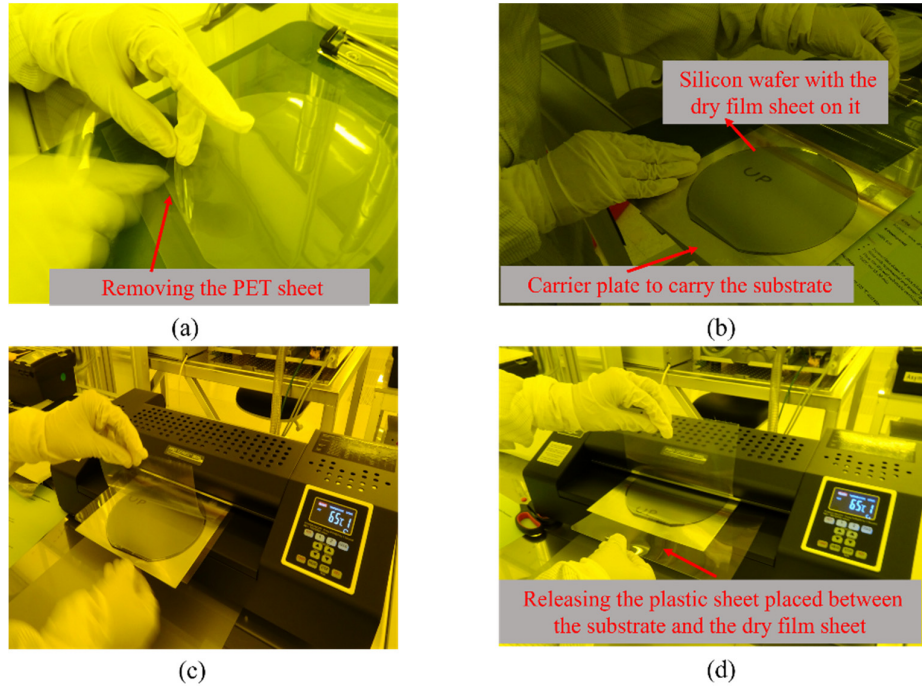


Figure 5.1: Dry film photoresist lamination steps: (a) removing the PET sheet, (b) dry film photoresist placed on a wafer and the wafer placed in carrier plate, (c) lamination of dry film photoresist, (d) withdrawing the middle plastic sheet slowly.

An Al plate was used to carry the substrate during the lamination process. As mentioned before, SUEX dry film comes sandwiched between two PET sheets. Before lamination, the PET sheet on one side was removed. The rest of the PET sheet was removed just before exposing the dry-film sheet under UV light. After releasing the PET sheet on one side of the dry film, it was placed on the substrate. A Si wafer has been used as a substrate for all the works presented in this thesis. A plastic sheet was placed between the dry film sheet and the substrate and removed slowly during the lamination process to assure a bubble-free lamination. Another plastic sheet was used to cover the substrate during lamination to prevent any sticking with the laminator. The detail of the fabrication process will be discussed in the following paragraphs.

To obtain a full polymer structure we laminate a thin SUEX film on the Si substrate as a base layer and later fabricate the device structure on this base layer. Once the device fabrication is completed the base layer can be released from the substrate depending on the requirement of the application. Process steps i- iv need to be repeated depending on the number of steps in a structure (discussed in Paper V). Generally, the fabrication can be divided into pairs of steps:

fabrication of the base layer, followed by the fabrication of the device structure on the previously fabricated base layer to define the pattern of the fabricated device. A schematic of the dry film fabrication is presented in Figure 5.2.

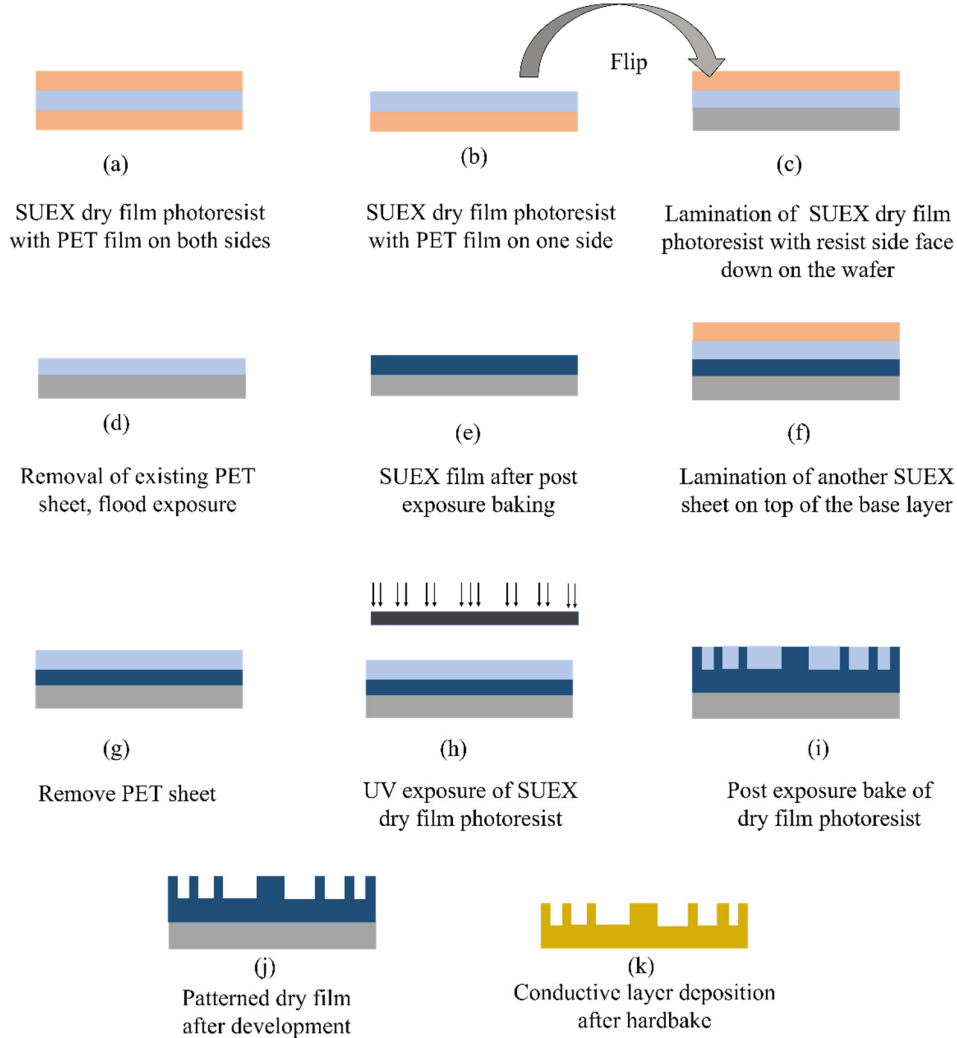


Figure 5.2: Schematic of dry film device fabrication.

i) Base layer fabrication

As mentioned earlier, a substrate is needed to laminate the SUEX films to run the fabrication steps. Depending on the application and other requirements one can decide to release the fabricated piece from the substrate or keep the fabricated piece on the substrate. We have demonstrated both approaches in this thesis. For some devices, we release the structure from the carrier wafer after completing chip fabrication (Paper IV and Paper V), whereas for some chips we kept the substrate and did not release the structure.

In case to keep the fabricated structure on the substrate good adhesion between the substrate and the laminated film is needed. A dehydration bake of the carrier is very important for good adhesion. Also, to assure proper adhesion between the laminated layer and the substrate, a PLB

was done. The process steps to fabricate the base layer were the following: lamination of thin SUEX dry film sheet, PLB, UV exposure, and PEB. The UV exposure can be done with (Paper V) or without (Paper II-Paper IV) a mask depending on the geometry of the base layer. The schematic process steps are shown in Figure 5.2a - Figure 5.2e. The details of the fabrication process can be found in Paper II.

If the fabricated structure is released after the fabrication, then the substrate surface does not need any surface preparation. The adhesion between the substrate and the dry resist is sufficient to complete the fabrication process. To release the structure, Omnicoat can be used as a sacrificial layer. After the development of the photoresist, the chip needs to go through a sacrificial layer removal step. Developer MF319 was used to remove the sacrificial layer. Another fast-releasing method used was to keep the PET sheet on one side. In this method, the PET sheet of the dry film was not removed, instead, the PET containing SUEX film was attached to the Si wafer by using a Kapton tape. Then the top PET sheet was removed, and the general base layer fabrication steps were followed. In this case, the fabricated device was released automatically during development.

ii) Device layer fabrication

Before starting the lamination of dry film sheets to obtain the device structure, the UV-exposed layer was subject to a plasma ashing step to improve the adhesion of the subsequent dry film layer.

To define the geometry of the device, multiple dry film sheets of different thicknesses were used. After the lamination of each dry film sheet, a PLB was done. Once the laminated layers were exposed to UV with the desired mask (Figure 5.2h) they went through a PEB (Figure 5.2i). As mentioned at the beginning of this section the process steps i- iv can be repeated to obtain multilayer structures. Once all the features are defined, the fabricated structure went through a development process. After that, either the released structure or the diced chips containing the substrate and the dry film structures went through a hard baking process. The hard-baked pieces were then sputtered and electroplated with a Ti/Au layer. In our cases, the thickness of the conductive layer was decided based on the frequency band and the skin depth of the deposited conductive material at that frequency. The details of the fabrication process were presented in Paper II-Paper V.

5.4 Process Optimization

5.4.1 Exposure dose selection

The exposure dose is one of the critical parameters of SUEX dry film fabrication. We noticed delamination of structures during development. The effect of all the parameters such as lamination temperature and speed, PLB and PEB time, and temperature, were tested, and yet the delamination issue was unaltered. However, increasing the exposure dose finally resolved the delamination issue.

To fabricate the devices presented in Paper II and Paper III, three dry film sheets of different thicknesses were used to fabricate the device layer. However, a single dry film sheet was used for the optimization process.

Process Optimization

A 40 μm thick SUEX film was used for a base layer (See section 5.3i) to fabricate a structure containing square pins of dimension $167\ \mu\text{m} \times 167\ \mu\text{m}$. A 400 μm SUEX sheet and the exposure energy of $1500\ \text{mJ}/\text{cm}^2$ were used for this assessment. The pins started to delaminate from the base layer during the development process. Figure 5.3b, shows that the lower part of the pin has a narrow edge, which indicates the exposure dose was not sufficient to crosslink the total thickness. For the following experiments, we decided to use thin film, even with the lack of process parameters from the manufacturer.

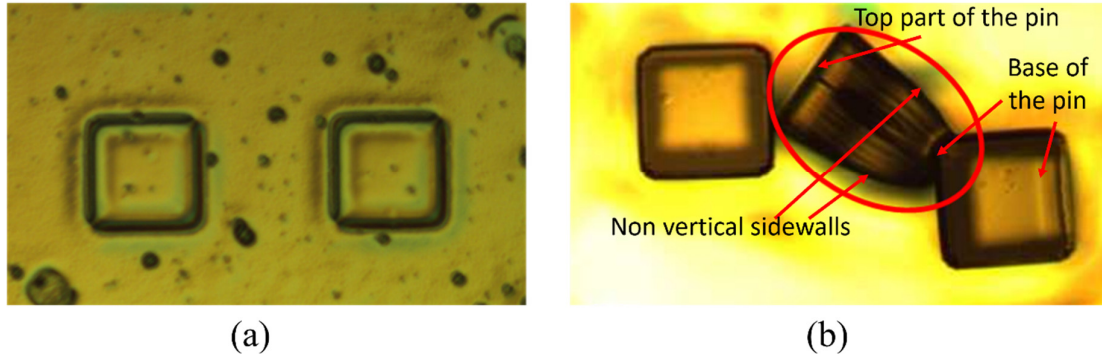


Figure 5.3: (a) Baselayer after delamination of pins, (b) a pin released from the base layer.

A 40 μm thick SUEX sheet was used as a base layer and a 50 μm thick SUEX sheet for the device layer. The suitable exposure dose to crosslink a 50 μm SUEX sheet was found to be $1500\ \text{mJ}/\text{cm}^2$. Figure 5.4 shows a microscope image of a 50 μm thick SUEX structure where the pins are attached to the base layer.

Later two 50 μm SUEX sheets were used to obtain the exposure dose for 100 μm thick film. In the SUEX data sheet, the recommended exposure dose for a 100 μm SUEX film was $450\ \text{mJ}/\text{cm}^2$, whereas in our case, an exposure energy of $3000\ \text{mJ}/\text{cm}^2$ was required for the 100 μm SUEX sheet, which is approximately 6 times higher than the recommended value. The exposure dose depends on the reflectivity of the substrate. Generally, a non-reflective substrate such as copper, glass, and Au needs a much higher dose (double or more) than the exposure dose needed on Si. As we used a thin SUEX film as the base layer the exposure dose was quite different than the exposure dose needed when Si was used as a substrate.

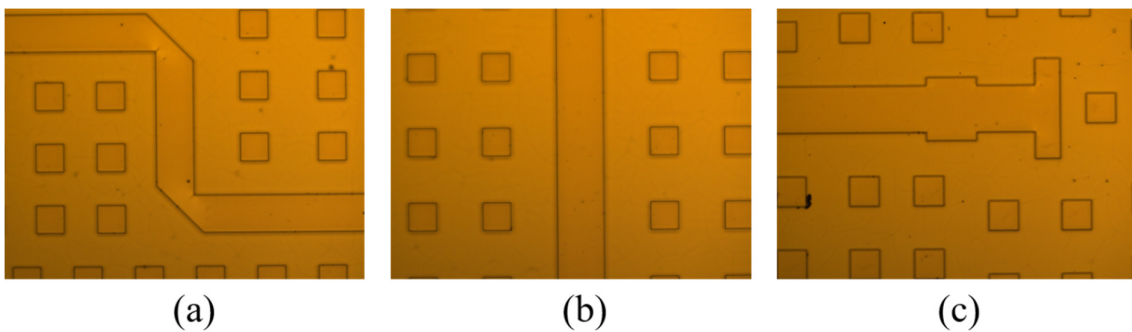


Figure 5.4: SUEX structures after optimizing the exposure dose, (a) bend ridge, (b) part of the resonator, (c) T-ridge section of the transition.

To obtain the structure mentioned in Paper II we used three SUEX sheets of thickness 200 μm , 50 μm , and 20 μm and by using an exposure dose of 9000 mJ/cm^2 the first SUEX dry film photoresist-based passive waveguide component was fabricated and presented in Paper II. Table 5.1 shows the selected exposure dose of SUEX dry film photoresist for different thicknesses.

Multiple exposures

From the previous discussion, we figured out that quite a high exposure dose was needed to achieve good adhesion between the fabricated structures and the flood-exposed base layer. However, this long exposure time can cause some problems such as dimensional variation of the mask due to heat, heating of the photoresist, and an overexposed pattern.

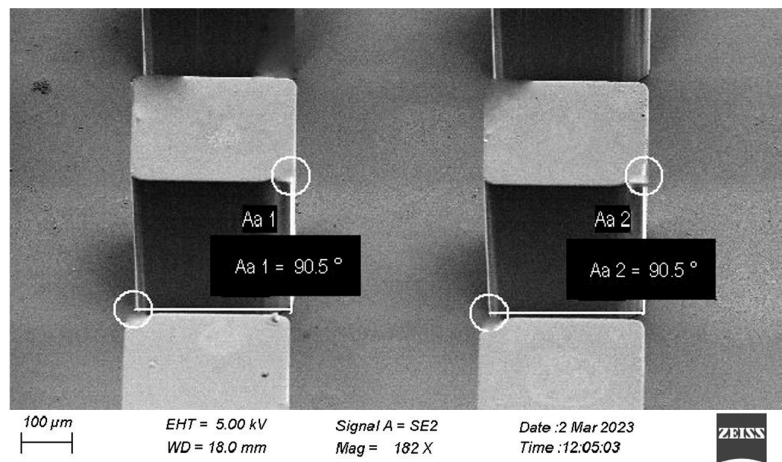


Figure 5.5: SEM image of a fabricated structure showing vertical sidewalls.

The device presented in Paper I has structures of height 270 μm and the exposure dose of 9000 mJ/cm^2 was used for 270 μm thick SUEX. Considering the above-mentioned challenges, we decided to execute multiple exposures of the photoresist. The process of performing multiple exposures is simple. We divided the total exposure dose into small fractions and perform the exposure of the photoresist maintaining a certain cool-down time interval. In the first optimization, we divided the total exposure into 6 steps with an interval of 30 sec, and an exposure dose of 1500 mJ/cm^2 was chosen for each step. Later we decided to have a shorter exposure dose and a longer gap between each exposure and therefore decide to use an exposure dose of 900 mJ/cm^2 with an interval of 60 sec between each exposure. We found the photoresist has enough time to relax if we have a longer break between each step and provide a better geometrical profile. Additionally, too high an exposure dose can cause an undesired exposure by scattering, and diffraction and results in undesired patterned transfer. In case of multiple exposures, the substrate containing the photoresists does not need to be removed from the mask aligner, rather a shutter will open and shut during exposure and resting period respectively. Figure 5.5 shows the SEM image of a structure fabricated by using 10 exposure doses.

Table 5.1: List of the exposure dose of SUEX dry film photoresist for different thicknesses.

Dry film sheet thickness, μm	Exposure dose, mJ/cm^2 on the base dry film layer	Recommended exposure dose, mJ/cm^2 on Si wafer[213]
40	1200	-
50	1500	-
80	1800	-
100	3000	450
140	4000	
200	6000	575
250	-	675
270	9000	-
400	9000	-
500	-	1150

5.4.2 Thick resist lamination

The lamination of the dry film is a straightforward process. However, thick resist lamination requires some consideration and an improved setup. As mentioned earlier an Al plate was used to carry the substrate during the lamination process. Therefore, the thickness of the structure that passes through the laminator includes an Al plate ($\sim 500 \mu\text{m}$ thick) and Si wafer ($\sim 500 \mu\text{m}$ thick), and on top of that the laminated SUEX film. We observed that $300 \mu\text{m}$ thick films along with the Al plate and Si wafer can pass through the laminator unproblematically. After that, the additional films that undergo the lamination step need some supporting setup to facilitate smooth lamination. In our case, we used shims of different thicknesses and created steps that would gradually move the laminator roller up and then eventually release it onto the Si wafer that is containing the resist layer. Figure 5.6 shows the lamination process of the thick photoresist.

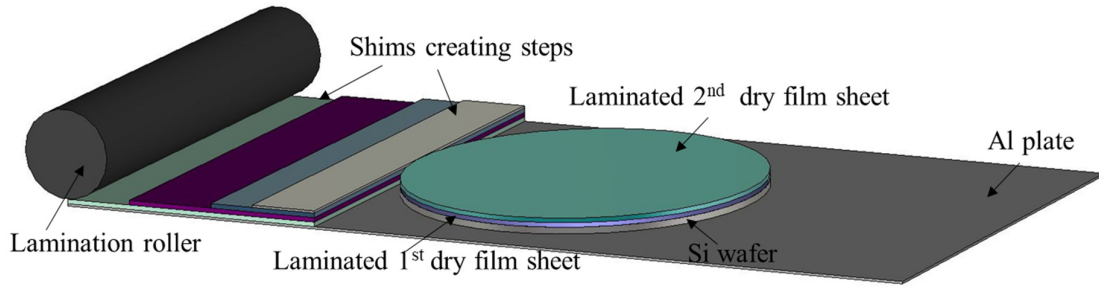


Figure 5.6: Lamination of thick photoresist by using shims.

5.5 Fabricated Devices

Different types of GW components have been fabricated by utilizing the SUEX dry film photoresist. In this section, we will present the fabricated devices and discuss their performance and the possibilities and limitations of the proposed fabrication method.

i) Gap waveguide resonator

Paper II presents a ridge gap waveguide resonator to exhibit two resonances at 234.6 GHz and 284 GHz. The loss in transmission lines can be determined by the Q-factors of the resonators. The waveguide flanges have been connected directly to each side of the resonator to establish a certain weak coupling between the transition and the resonator. Therefore, the Q of the resonator is not affected by the loading of the transitions, and the unloaded Q (Q_u) is possible to measure. To help the measurement a milled package has been used and the waveguide flanges are connected directly to the package. The details of the designed resonator and its fabrication can be found in Paper II.

The height of the ridge and the pins was targeted at 270 μm . The pin height of the fabricated device was measured to be $272 \pm 2 \mu\text{m}$ and exhibited excellent height uniformity and flatness over the laminated area, and the SEM image shows that the sidewalls have a high verticality (see Figure 5.5). The fabricated resonator and the measurement result are presented in Figure 5.7.

Discussion

The ridge gap resonator was previously fabricated by using silicon micromachining [93], and SU8 micromachining [214]. The main reason to use different materials to fabricate the same device was to investigate the material and method in terms of device performance, fabrication process complexities and time, and the possibility of batch production with a low production cost. A detailed analysis covering the fabrication method, processing time, and device performance has been given in Paper II. Table 5.2 presents a performance comparison of the unloaded Q-values and losses from simulations, and measurement of an identical ridge gap resonator fabricated by Si, SU8, and SUEX dry film photoresist. The design of the RGW resonator was optimized considering the thickness of dry films that were available. Hence, the

simulation result of the presented resonator was not identical to the previously demonstrated RGW resonator [93, 214].

Paper II successfully demonstrates that SUEX dry film can be an alternative to conventional DRIE and liquid SU8 photoresist for the fabrication of mm-wave passive waveguide components. Additional benefits of using SUEX films besides providing geometrical structures with high accuracy are fewer processing steps, shorter prototyping time, and low processing cost as expensive cleanroom equipment is not required.

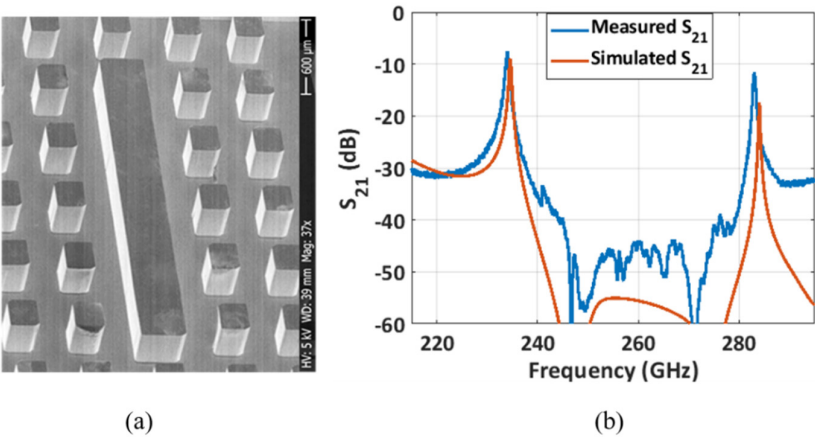


Figure 5.7: SEM image of a fabricated resonator and full electromagnetic wave simulation compared with measurement results (Paper II).

Table 5.2: Measured unloaded Q -values and corresponding loss/mm for the ridge gap resonator fabricated by silicon, SU8, and SUEX.

Technology		Frequency (GHz)		Q_u -value		Loss(dB/mm)	
DRIE [93]	Simulation	234	284	859	992	0.025	0.026
	Measured	234	283	642	628	0.033	0.043
SU8 [214]	Simulation	234	284	859	992	0.025	0.026
	Measured	233	283	319	628	0.067	0.041
SUEX Paper II	Simulation	234.6	284	802	938	0.026	0.028
	Measured	234	283	656	786	0.032	0.033

ii) Gap waveguide transition

At high frequencies, the interface of most measurement setups is based on RWs. Therefore, low-loss, simple and wideband transitions from GW to conventional RWs are needed. Different types of existing transitions have been mentioned in Chapter 3. However, the proposed transitions presented in Paper III are zero-step transitions. The significance of the designed transitions comes from their simplicity, easy assembly, high tolerance to manufacturing and assembly error, and wideband performance. Three transmission lines have been designed, fabricated, and demonstrated: a straight ridge line, a bent ridge line with two 90-degree bends, and a groove gap line. For all these transitions, the waveguide port was located on top of the metal plate of the waveguide. This top plate acts as the PEC surface of the gap waveguide structures and the rows of pins on the bottom plate act as a PMC surface.

SUEX dry film photoresist has been used for the fabrication of the transitions. The height of the structures is $270\text{ }\mu\text{m}$, and a $40\text{ }\mu\text{m}$ thick base layer was used to construct the ridge and the pins. The thickness of the base layer is independent of transition performance. However, it is critical while designing the support package (discussed later in this section). Three SUEX dry film sheets of thickness $200\text{ }\mu\text{m}$, $50\text{ }\mu\text{m}$, and $20\text{ }\mu\text{m}$ have been used to achieve $270\text{ }\mu\text{m}$ thick structures. Details of the designed transitions and the fabrication method were presented in Paper III. Figure 5.8 shows the three fabricated chips and SEM images of the straight RGW and the bent RGW.

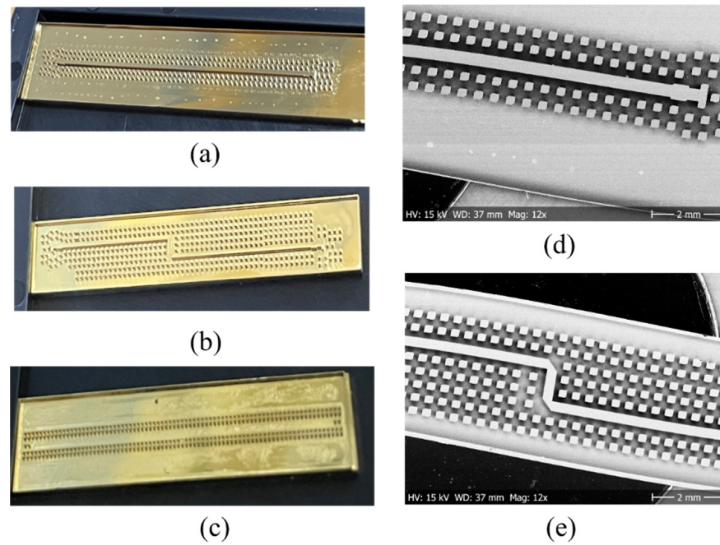


Figure 5.8: Fabricated chips: (a) straight RGW on chip (b) bent RGW chip, (c) groove GW chip. SEM images of the fabricated chips: (d) straight RGW, (e) bent RGW (Paper III).

A tolerance analysis was conducted to investigate the sensitivity of the designed RW to RGW transition with respect to manufacturing and assembly errors. The effects of variations in air gap size, the height of the pins, and the misalignment between the chip and the top waveguide ports have been analyzed. The pin height and the air gap have been swept around their nominal values to observe their sensitivity toward dry film fabrication (considering the fabrication accuracy presented in Paper II). It has been observed that even after $\pm 10\text{ }\mu\text{m}$ air gap variation the transition performance is satisfactory. However, as the pin height varies within a range of

$\pm 10 \mu\text{m}$, the overall working bandwidth of the transition is reduced slightly (details can be found in Paper III)

Different techniques to measure THz passive components have already been discussed in Chapter 1. It is very common to use supporting blocks to characterize the fabricated passive waveguide components. Three different support packages were designed and manufactured by CNC milling for the characterization of the three fabricated chips. In Paper III we propose a very simple technique to overcome the misalignment between the DUT and the RW. The top part of the support package has an opening for the standard WR-3.4 rectangular waveguide and acted as a PEC surface during the measurement. The bottom part of the support package has a channel for the chip. The channel was designed in a way so that the chip did not move during the measurement. The depth of the channel was decided considering the thickness of the base layer ($40 \mu\text{m}$ thick SUEX film) and carrier wafer (for the case when the fabricated structure is not released).

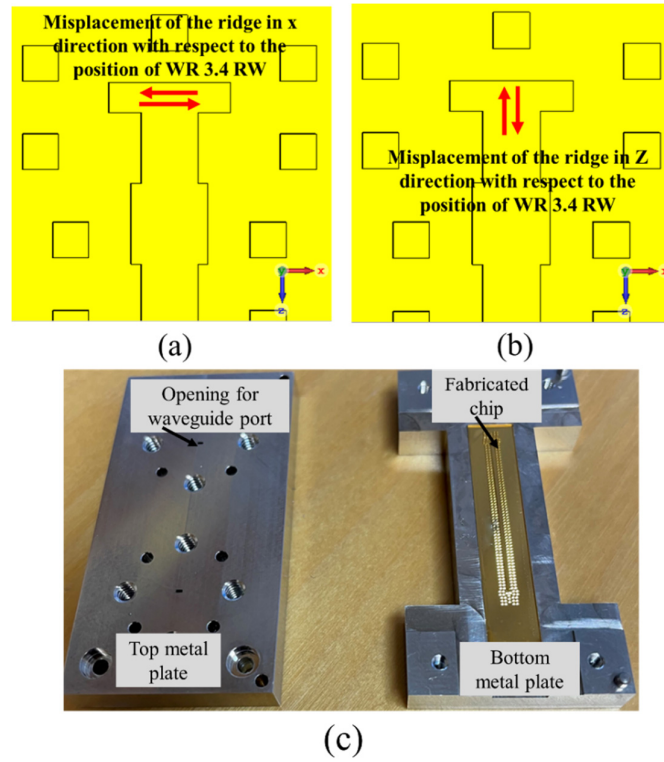


Figure 5.9: Schematic of the misalignment of the ridge with respect to the WG position, (a) transverse direction, (b) longitudinal direction, and (c) top and bottom plate of the support package with the fabricated chip (Paper III).

The tolerance measurements showed that even with $\pm 20 \mu\text{m}$ misalignment for the original position of the ridge, in the transverse direction, the performance of the transition remains unchanged. However, in the longitudinal direction, the transition is a bit more sensitive, yet the S_{11} is below -15 dB with this $\pm 20 \mu\text{m}$ misalignment. Considering the accuracy of the milled piece ($\sim \pm 5 \mu\text{m}$), $\pm 20 \mu\text{m}$ misalignment was a very good margin to perform the measurement precisely. Figure 5.9 shows the schematic of the misalignment of the ridge with respect to the WG position and Figure 5.10 shows the simulation and measured S-parameters of back-to-back transmission lines.

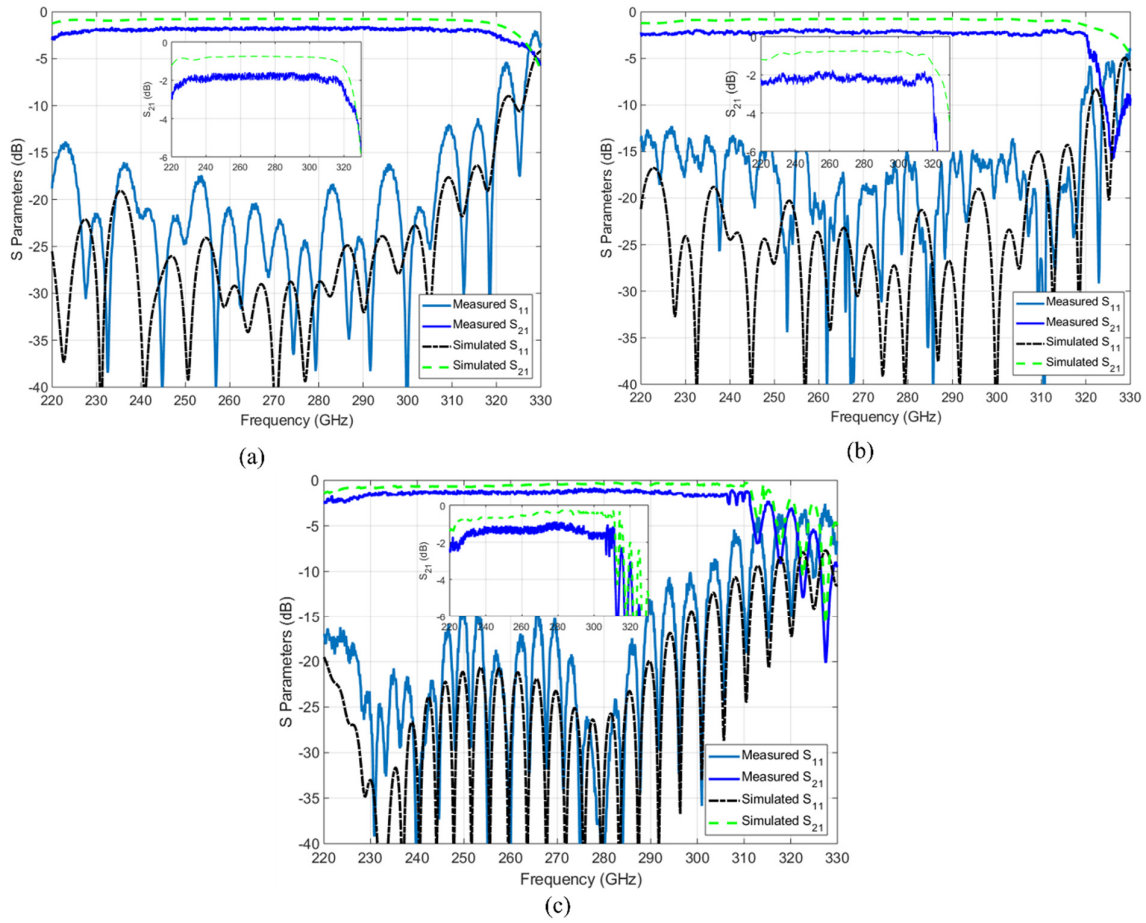


Figure 5.10: Measured (solid line) and simulated (dashed lines) S -parameters of the back-to-back (a) straight RGW transmission line, (b) bent RGW transmission line, (c) GGW transmission line (Paper III).

Discussion

The measurement results show good agreement with the simulation. This proves the validity of the fabrication method. The measured height of the fabricated pins is $272 \pm 2 \mu\text{m}$, and the surface roughness of the fabricated chip is $3.25 \pm 0.5 \text{ nm}$. This is on par with the accuracy presented in Paper II and verifies the reproducibility of the fabrication method.

Table 5.3 presents a comparison between the performance of waveguides fabricated by state-of-the-art manufacturing techniques and our work. The results presented in the table show RW to RGW transition has higher insertion loss compared to the GGW transition which is very common and already reported [130].

However, the GGW transition demonstrates insertion loss equivalent to that of CNC milled and DRIE fabricated RW. It should be noted that the 3-D printed waveguides and Si micromachined waveguides have comparable losses to the commercial ones, however, surface treatment is required to maintain a low surface roughness (see Chapter 2). Both SU8 and Si micromachining requires very time-consuming fabrication processes. Therefore, the dry film photoresist has excellent potential to act as an interconnect and integration platform (will be discussed more in Chapter 6).

Table 5.3: State-of-the-art waveguide technology

Technology	Frequency (GHz)	IL (dB/mm)	Ref
CNC	220–330	0.04	[215]
CNC	210–280	0.016	[216]
DRIE	220–325	0.045	[84]
DRIE	325–360	0.081	[86]
SU8, single layer	220–325	0.05	[30]
SU8, double layer	220–325	0.03	[30]
SU8	220–300	0.03	[217]
SU8 bend WG	240–300	0.134	[218]
UV-LIGA	220–325	0.096	[219]
3D printing	220–330	0.02	[220]
Dry film photoresist straight RGW-RW	220–320	0.075	Paper III
Dry film photoresist bent RGW-RW	220–320	0.075	Paper III
Dry film photoresist GGW-RW	220–320	0.045	Paper III

iii) Gap waveguide-based power divider

Power dividers are important components of microwave and millimeter wave circuits. They work as fundamental building blocks for multiplexers, power combiners, and antenna feed networks. Depending on its application a power divider can be used for both dividing and combining power. The designed power divider presented in Paper IV used the straight RGW transition that has been presented in Paper III to couple the electromagnetic (EM) wave that passes through the standard WR-3.4 RW to propagate through the GW structures. All the design details can be found in Paper IV. Similar to the structures presented in Paper III, the height of the ridges and the pins of this designed power divider is $270\text{ }\mu\text{m}$. Therefore, the fabrication process was the same as that presented in Paper III. While designing the 3-dB power divider a $\lambda/4$ section was added to the T-junction with a length of $275\text{ }\mu\text{m}$ and a width of $379\text{ }\mu\text{m}$. The middle ridges are cut to divide the power equally between them. The features of this middle cut were selected considering better input matching, better power distribution between the two ridges, and fabrication limitations.

Before finalizing the design, a tolerance check considering the fabrication accuracy was performed. The air gap between the top plate and the structure of the bottom plate is a critical parameter for any GW device. Therefore, to evaluate the tolerance error, this air gap has been swept $\pm 20\text{ }\mu\text{m}$ around the nominal value. Also, the effect of the pin height variation has been examined and $\pm 10\text{ }\mu\text{m}$ tolerance has been considered (details can be found in Paper IV). Figure 5.11 shows the microscopic image, a SEM image of the fabricated power divider, a close-up SEM image of the T-section, and the measurement setup. The height of the fabricated structures is $272 \pm 2\text{ }\mu\text{m}$ which is very close to the designed pin height. The measured surface roughness of the fabricated chip was $3.25 \pm 0.5\text{ nm}$, which is adequate for this frequency range.

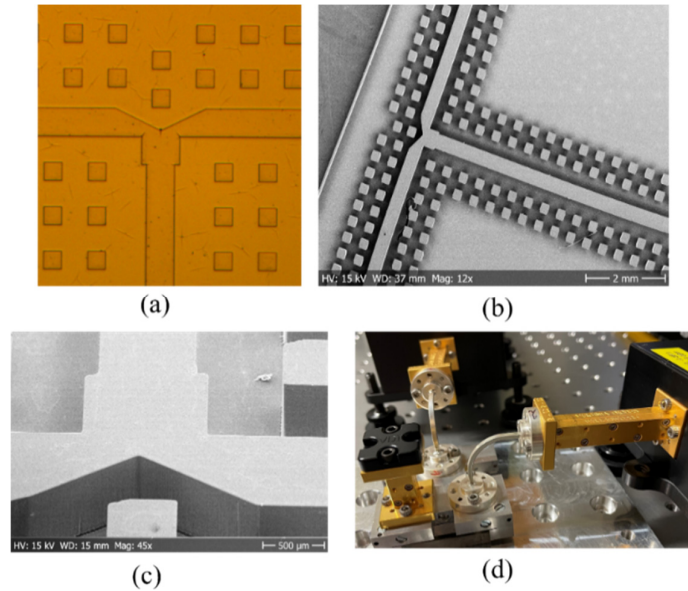


Figure 5.11: (a) Microscopic image, (b) SEM image of the fabricated power divider, (c) closeup SEM image of the T-section, (d) measurement setup.

Discussion

Fabrication of the GW power divider requires further considerations due to the presence of the T-section ridge. During the design of the power divider, we consider the middle section cut in a way that assures better power distribution between the two ridges, and that during fabrication, we do not end up with a rounded corner instead of a sharp corner. The SEM image presented in Figure 5.11 shows a sharp section that demonstrates that the accuracy of the fabrication method is suitable for THz frequencies. This indicates that SUEX dry film photoresists can deliver features with high accuracy by proper selection of the process parameters.

iv) D-band slot array antenna based on gap waveguide technology

A slot array antenna, operating in the D band, has been designed based on gap waveguide technology, fabricated by SUEX dry film photoresist, and presented in Paper V. The designed antenna consists of two layers: a slot layer and a feed layer with a transition to measuring waveguide. The antenna contains structures that require a multiple-level dry film fabrication process with thicknesses ranging from 80 μm to 400 μm with $\pm 10 \mu\text{m}$ tolerance. The input reflection coefficient was measured to be below -11 dB over a 10% bandwidth from 136-148 GHz, and the antenna gain was measured to be 11.4 dBi at 142 GHz, both of which are in fair agreement with simulations. The presented slot array antenna was designed based on the zero-gap waveguide concept. However, considering the fabrication tolerance we optimize the design for a 10 μm air gap. We observed the impedance matching for air gaps from 0 μm to 20 μm , where S_{11} remains below -10 dB within the band.

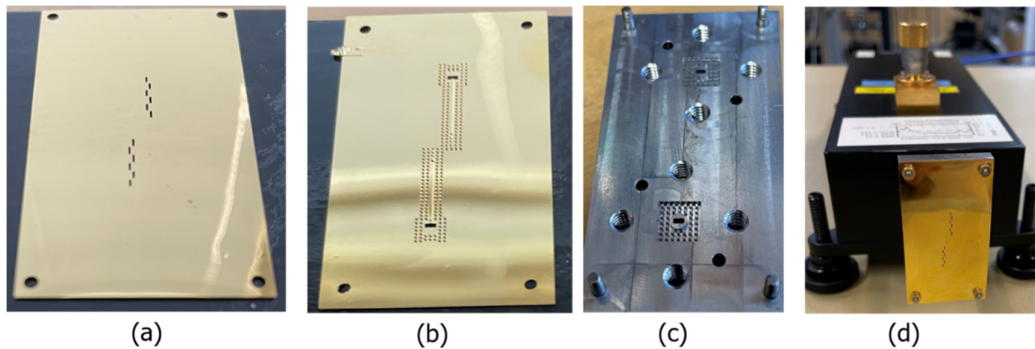


Figure 5.12: The fabricated antenna, (a) slot layer, (b) feed layer, (c) supporting bottom plate with WR-6.5 opening and gap waveguide pin flange structure, (d) fabricated antenna mounted in the machined supporting plate and connected to the VDI D-band extender.

The fabrication of the slot layer is simple as it requires only a single fabrication process. The thickness of the slot layer in our design was 400 μm . The feed layer consists of a 400 μm thick base that contains the opening for the waveguide, a ridge with a step, and pins. The feed layer design of the slot array antenna was optimized considering the available SUEX film thickness. The fabrication of the feed layer requires four rounds of fabrication. A 400 μm thick base layer was patterned first to define the opening of the WG, later a 120 μm step was defined along with defining the partial height of the ridge and partial height of the pins. After that, the remaining 180 μm height of the ridge was defined together with a partial height of the pins and later the remaining height of the pins was defined. The details of the design and the fabrication process can be found in Paper V.

The achieved slot layer thickness was $404 \pm 2 \mu\text{m}$, the height of the step in the ridge was $123 \pm 2 \mu\text{m}$, the height of the ridge was $304 \pm 2 \mu\text{m}$, and the pins were $385 \pm 2 \mu\text{m}$. The measured surface roughness of the fabricated chip was $8.7 \pm 0.5 \text{ nm}$.

To characterize the fabricated antenna a supporting piece is needed. The supporting metal block has an opening to connect it to a conventional RW flange. To facilitate the mounting of the fabricated chips, alignment pins have been used and the fabricated pieces contain alignment holes. Even though the structures fabricated by using SUEx dry film are comparatively flat, while mounting the fabricated feed layer to the metal block, introducing a few micrometers gap between the metal block and the feed layer is hard to avoid. At frequencies above 100 GHz, even a microscopic air gap between the antenna port and the measurement flange introduces significant leakage and influences the antenna measurement. A gap waveguide flange is introduced on the back side of the antenna to minimize leakage. The pin-flange adapter was previously used to avoid leakage at the interface of two waveguides[41]. The introduction of the flange implies a slight change in the total reflection coefficient. However, the simulation result showed that even after having a $25 \mu\text{m}$ air gap between the antenna port and the measurement flange the reflection coefficient of the antenna stays below -12 dB over the band of interest.

Thermal cycling test

In Chapter 1 we mentioned different types of challenges that are encountered when we want to work at the THz frequency range. Among the different challenges, one is thermal effects, and these are aggravated when using a polymer as a device material. It is expected that a system will be exposed to a wide range of temperatures during operation. One expected phenomenon can be the delamination of the conductive layer during thermal cycling due to the mismatch in the CTE of the polymer and the deposited conductive layer. Keeping this in mind, a thermal cycling test in the temperature range -50 to 135°C with a ramp-up time of 10 min and 30 min dwell time was conducted for 300 thermal cycles.

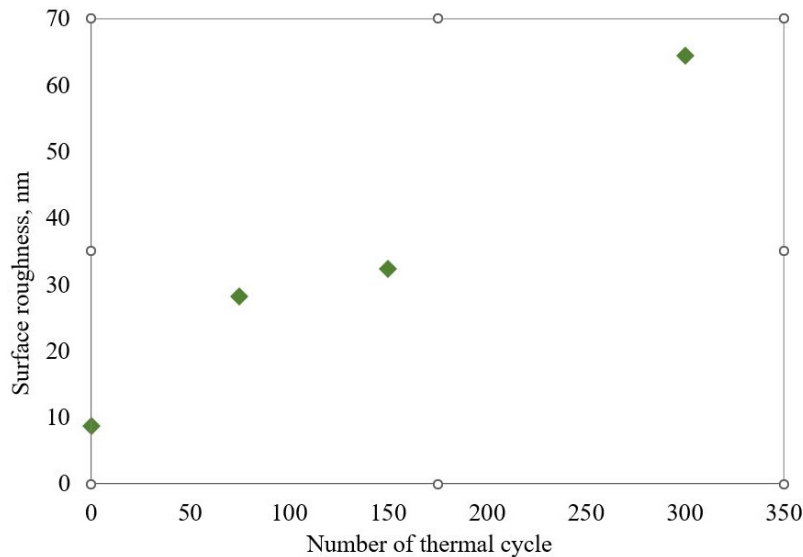


Figure 5.13: Measured surface roughness of the fabricated antenna at different thermal cycles.

To evaluate the effect of thermal cycling on the antenna parts, the antenna chip has been examined under the microscope to investigate any crack or delamination of the conductive layer. Also, the reflection coefficient and the surface roughness of the antenna have been measured after 75, 150, and 300 thermal cycles. Figure 5.13 shows the measured surface roughness of the fabricated antenna at different thermal cycles. A similar effect has been reported where the surface roughness increases with increased temperature [221, 222].

The CTE of SUEX is ~ 50 ppm/ $^{\circ}\text{C}$ [213] and AU is ~ 14 ppm/ $^{\circ}\text{C}$. To evaluate the effect of thermal cycling on the antenna parts, the antenna chip has been examined under the microscope to investigate any crack or delamination of the conductive layer. However, no delamination between the SUEX film and the AU layer has been observed, even with a CTE mismatch. The measured S_{11} is below -11 dB within the band of interest even after conducting the thermal cycling tests. Figure 5.14 shows the S_{11} measurement results after 75, 150, and 300 thermal cycles. Detail discussion regarding the slight mismatch among the measurement results can be found in Paper V.

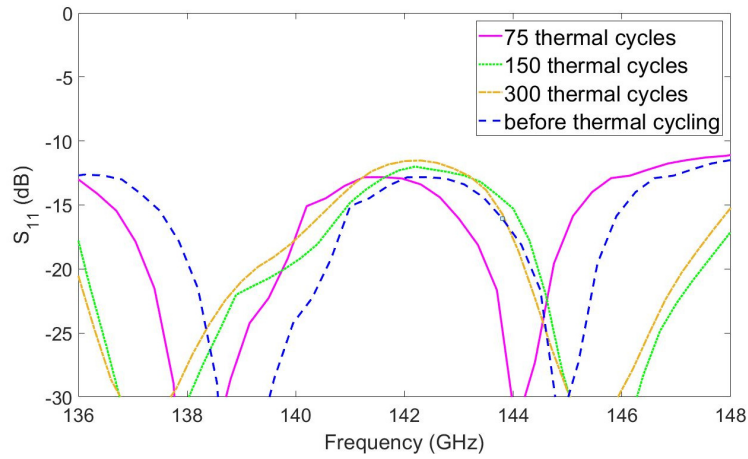


Figure 5.14: Simulated and measured S_{11} of the fabricated antenna before and after the thermal cycling test.

Discussion

Previously SUEX dry film photoresist has been used to fabricate waveguide components that contain structures of similar height. That choice was made intentionally to have a better understanding of the fabrication process and also to resolve fabrication issues. Once the fabrication method had been calibrated and a better understanding of the fabrication method has been attained, the slot array antenna containing a multilayer structure was fabricated.

In section 4.5i- 4.5iii, we observed that SUEX can fabricate structures with 2 ± 2 μm accuracy. However, the fabrication accuracy of the 380 μm pins was 385 ± 2 μm . The fabrication precision can be dissimilar in the case of multiple-height structure and depend on the number of dry film sheets that have been used to acquire a certain thickness. In the case of multilayer structure when we define structures step by step, the total number of sheets that have been used to fabricate the complete structure will increase and so will the fabrication inaccuracy.

To fabricate a pin of 380 μm height, one 300 μm SUEX film and two 40 μm SUEX films are required. However, if we consider this specific antenna the pin has been defined in different

steps; partially while defining the step of $120\ \mu\text{m}$ ($100\ \mu\text{m} + 20\ \mu\text{m}$ SUEX films), partially while defining the ridge of $180\ \mu\text{m}$ ($100\ \mu\text{m} + 40\ \mu\text{m} + 40\ \mu\text{m}$ SUEX films), and finally by laminating two $40\ \mu\text{m}$ SUEX films. Therefore, the accuracy will be different in the second case. Figure 5.15. shows the schematic of a case where the fabrication of a pin of $380\ \mu\text{m}$ height is part of a multilayer fabrication. By considering the available thicknesses of SUEX dry films, better accuracy is possible to achieve. The fabrication accuracy for the fabricated pins was $385 \pm 2\ \mu\text{m}$, which is still within the tolerance range of the designed antenna.

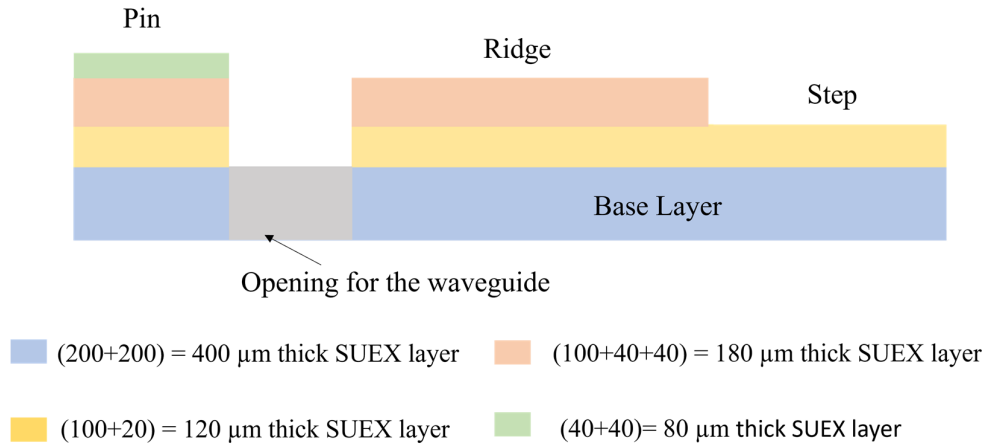


Figure 5.15: The schematic of a case where the fabrication of a pin of $380\ \mu\text{m}$ height is part of a multilayer fabrication.

Another challenge was the risk of delamination between the separately laminated and patterned layers. Previously, different thicknesses of dry film sheets have been laminated and later exposed together. For this antenna, step-by-step lamination and exposure were needed and adhesion between the crosslinked SUEX film and non-crosslinked SUEX film can be different. However, the proper selection of the exposure dose assures the adhesion between the separately laminated and patterned layers. With these measures, SUEX dry film can be used to obtain complicated geometry if required.

5.6 Summary

Accomplishments

Fabrication tolerance and repeatability

The fabrication tolerance for the proposed fabrication method meets the tolerance requirement of THz frequencies. The obtained height of the structures is better than 1% of the desired height. Different types of structures have been fabricated by using the optimized fabrication parameters. The fabrication results and measurement results were satisfactory and show the reproducibility of the fabrication method.

Fabrication complexity

The proposed fabrication process is a straightforward method. Compared to liquid photoresist-based processing it requires less time-consuming fabrication steps. While developing the fabrication process, only the exposure dose needs to be modified for different SUEX film

Summary

thicknesses. The rest of the process parameters: lamination temperature and time, PLB temperature and time, and PEB temperature can be the same and independent of feature size and geometry. Even though PEB time and development time depend on the geometry of the feature, those parameters are not critical and do not need fine-tuning.

Surface roughness of the fabricated device

The surface roughness of the fabricated devices plays a strong role in the device's performance. The measured surface roughness of the fabricated device is very low and suitable for any THz device. No post-fabrication surface treatment is needed which simplifies the total device fabrication process.

Limitations

Alignment

The performance of all the GW devices is very much dependent on the constant air gap between the PEC and the PMC surface. If the PEC surface is made out of the SEUX film, then maintaining a constant air gap throughout the entire structure can be challenging. The slot layer presented in Paper V is aligned to the feed layer with four alignment screws. When the slot layer was assembled with four screws placed in the four corners of the supporting metal blocks, an unwanted air gap was introduced in the middle section. Therefore, the fixing and placement of the screws need some extra attention to avoid an unintentional air gap in the middle.

Multiple height structures

Obtaining a multilayer structure with SUEX is not very straightforward. SUEX films are not transparent and therefore it is difficult to get clear visibility of the previously patterned alignment mark. The general way to obtain a multi-layer structure by dry photoresist is by developing the first patterned layer, making the pattern visible, and laminating another layer of dry film and patterning it. The visibility of the developed pattern gives a better view from the newly laminated layer. However, this will increase the total fabrication time. The alignment marks must be designed and patterned in a way so that they can be visible from the laminated top layer. Otherwise, the alignment process can become quite challenging and time-consuming.

Thickness limitation

SUEX films are readily available in a limited number of thicknesses. This restricts the flexibility of the designers when doing electromagnetic design. However, it is possible to order customized thicknesses, which will introduce some extra costs.

Mechanical tolerance

The SUEX film has shown significant strength while mounting the fabricated chip through the alignment pins and during the tightening of screwing. They are quite stable during handling. However, multiple occasions of mounting and demounting can cause a crack in the chip. Proper selection of the hard baking time and temperature can improve the mechanical stability of the SUEX chips.

Chapter 6

Transition from Waveguide-to-Microstrip Line

In this chapter, we will present two low-loss waveguide-to-microstrip line transitions suitable for MMIC integration and packaging. Two different transitions will be discussed in terms of fabrication accuracy, alignment tolerance, as well as the surface roughness of the fabricated and the milled pieces. The effect of using either an E-plane split block or an H-plane split block will also be addressed.

6.1 Background and Motivation

Integrating the active components with their passive counterparts is the way to realize a complete system. With the advances in semiconductor technologies, the possibility of a complete multi-functional integrated circuit at millimeter-wave (mmWave) and Terahertz (THz) frequency bands is becoming a reality now [223]. Ideally, the packaging process of such MMICs should not influence the system performance and be attained with low loss and high bandwidth. Different techniques of integrating active and passive components have been discussed in Chapter 1 and Paper VI.

Compact MMICs are compatible with planar waveguides such as microstrip and coplanar waveguides. On the other hand, passive components such as antennas and high-quality factor filters are waveguide technology based. Additionally, for packaging, where the required distance between the active and the passive devices are not scalable with frequency due to the need for standard interfaces and bias connections, low-loss transitions are essential. Recently, SIW has been used as THz interconnect but these transitions require another additional transition to connect the RW, where the interface with RWs is a requirement and thus increases the overall loss of the system [224]. On the other hand, reported CPW to RW transitions require precise metal contact to provide transformation of the EM field from one transmission line to another [225]. Thus, a good transition between a microstrip line and an RW is very attractive and beneficial. However, as mentioned in Chapter 1, integration of active microwave components with the standard waveguide is complicated and challenging due to the need for proper electrical connection, limited by substrate size, or narrow band operation.

AMC surfaces have already been used to suppress the parasitic mode in oversized MMIC substrates [47, 226]. At the THz frequency band and especially above 100 GHz the integration becomes challenging in terms of waveguide loss, fabrication accuracy, alignment accuracy, and surface roughness. Similarly, at higher frequencies, the dimension of the AMC pins becomes small with increased requirements on tolerance. As the dry film photoresist has shown

very good fabrication accuracy the AMC pins can be fabricated by the dry film photoresist above 100 GHz. Paper VI presents two transitions from a waveguide to a microstrip line for large-sized MMIC integration and packaging at 250 GHz. The presented transitions work at 220 GHz to 320 GHz. The proposed transitions can be used for chip-to-chip interconnectivity as well.

6.2 Challenges

Design limitation: The design of the microstrip structure needs to be as simple as possible at the same time it should offer low insertion loss. The design of the transition should be done considering the fabrication tolerance to take proper advantage of the micromachining methods. Also, transitions should be compact and should operate over as large a bandwidth as possible.

E-plane and H-plane split block configuration: The effect of an H-plane split block has already been discussed. Therefore, the design must consider the effect of leakage due to improper alignment between the split blocks.

Alignment of the microstrip chip: If the transition involves several features, and all the features are dependent on each other, then the separately manufactured parts can influence the performance of the transition due to misalignment. A tolerance check considering the misalignment among different blocks needs to be done during the design of the transition. Also, the metal split blocks need some attention to ensure a better alignment of the chips.

Size of the MMIC: The size of the MMIC is a very important factor while designing a transition. Usually, multi-functional MMICs are bigger than the size of the chip that contains only the transition section. Thus, direct MMIC integration may not be possible in all transition configurations.

Fabrication challenges

Thin substrate handling: The designed transition needs a dielectric material as substrate and depending on the operating frequency the substrate can be very thin. Handling a thin substrate during fabrication can be very challenging and it needs to be attached to a carrier wafer. Different types of wafer bonding techniques have already been mentioned and discussed along with their application area and bonding conditions [227, 228]. Thin wafers deform easily during bonding to compensate to surface nonuniformities at the bond interface [227]. Therefore, in the case of using a thin substrate, a chip-sized substrate is usually used during processing, so that it can bond easily and entirely with the carrier wafer. However, this is not a suitable method for batch fabrication. A bonding method that is suitable for handling an entire wafer during processing will be interesting to consider.

Patterning the substrate: A general way of patterning a substrate is using the liftoff technique, where a target material is deposited on the surface of a substrate using a sacrificial material (e.g. photoresist). However, if the thickness of the deposited material is several microns, then the liftoff of the sacrificial material can be difficult. Therefore, the choice of fabrication methods needs some consideration.

6.3 Transition Design

An inline transition and a vertical transition have been presented in Paper VI. Both transitions used five rows of EBG pins in the direction of the width of the transition section to prevent any leakage during the coupling and propagation of the electromagnetic wave through the microstrip line. Therefore, this allows the use of MMIC without considering any size limitation.

The dimensional accuracy of the EBG pins is critical in the performance of the proposed transitions. Considering the high fabrication accuracy of SUEX, we have chosen to use SUEX dry film photoresist to obtain the pins instead of milled EBG pins. Therefore, while designing the transitions the height of the EBG pins was selected considering the available thickness of the SUEX dry film sheets (discussed in Section 5.5iv). For the inline transition, the height of the EBG pins has been chosen to be $280\text{ }\mu\text{m}$ and for the vertical transition, it was set to $260\text{ }\mu\text{m}$, which is slightly less than $\lambda/4$ at the operating frequency.

To realize a chip-to-waveguide transition, the inline transition used an on-chip patch, with a microstrip line to excite the patch and a cavity that acts as a coupling section to couple the EM signal between the microstrip section and the waveguide section. Also, a capacitive post has been used as a coupling pin to enhance the bandwidth of the proposed transition. The ground plane underneath the patch was removed to couple the signal through the substrate. A coupling pin was used to help the coupling of the signal.

A $50\text{ }\mu\text{m}$ -thick quartz chip was used as substrate and was placed in a back-to-back metal waveguide block module. In this case, the waveguide was split in the H-plane. The bottom part of the module housed the chip, the coupling pin, the cavity, and half of the waveguide channel and the top part of the module included the EBG structure and half of the waveguide channels. Figure 6.1 shows the proposed inline transition.

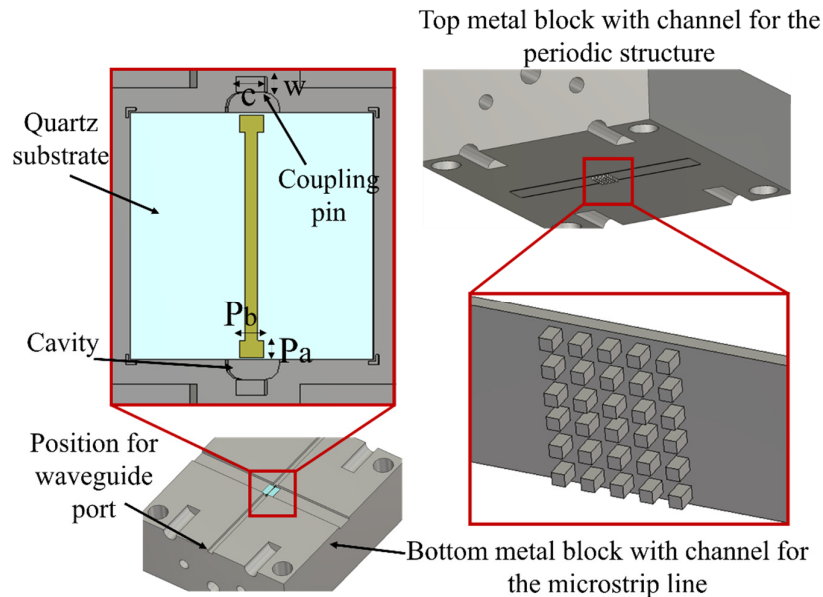


Figure 6.1: Proposed packaging solution as an inline transition.

The proposed vertical transition is a straightforward transition without using any back short or cavity to couple the electromagnetic field between the waveguide to the microstrip line, shown in Fig 6.2. A rectangular patch was used to realize a chip-to-waveguide transition. For further impedance matching and to achieve a wide-band performance, a narrow microstrip subsection has been used which acts as an inductor and compensates for the fringing capacitance of the probe section. The backside metal is removed in the area underneath the patch to allow coupling through the substrate. The main benefit of the vertical transition over the previously mentioned inline transition is that the vertical transition uses an E-plane split block module and is hereby free from the split block-related leakage issues mentioned in Chapter 1. The details of both transitions can be found in Paper VI.

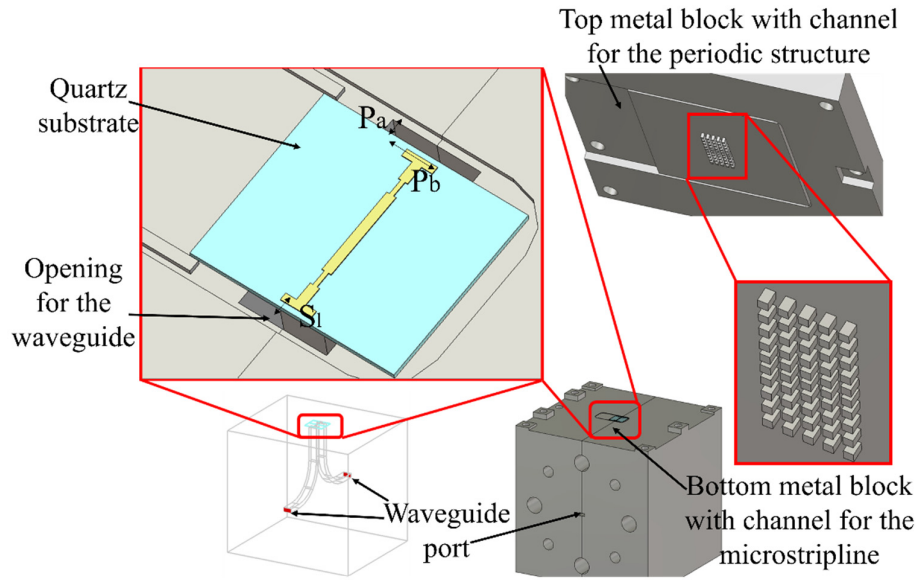


Figure 6.2: Proposed packaging solution as a vertical transition for arbitrary width substrate.

6.3.1 Supporting metal block design

As mentioned earlier the microstrip chip and the top EBG pins both have been fabricated using the micromachining methods and later placed in the metal blocks. Therefore, the design of the metal blocks required some consideration. The bottom metal plate for the inline transition contains the cavity, coupling pin, and alignment marks to place the quartz substrate and the waveguide channel. The top metal plate has a channel to place the SUEX EBG pins. The bottom part of the metal block for the vertical transition is comparatively simple as it contains only a channel for the microstrip chip, alignment marks, and the opening for the waveguides and the top plate has a channel for the SUEX EBG pins.

The depth of all the channels for holding the chips and the EBG layer has been determined considering the thickness of the quartz substrate including conductive glue, and the thickness of the base layer that contains the EBG pins with some extra depth considering the thickness of the conductive glue. Hence an extra 10 μm depth was added to the channels in the metal blocks. Alignment marks were used in the bottom metal block to help the placement of the microstrip chip relative to the WG opening. Standard WR-3.4 interfaces were machined on

both the input and output ports of the module to help the characterization. Figure 6.3 shows the schematic of the milled metal pieces.

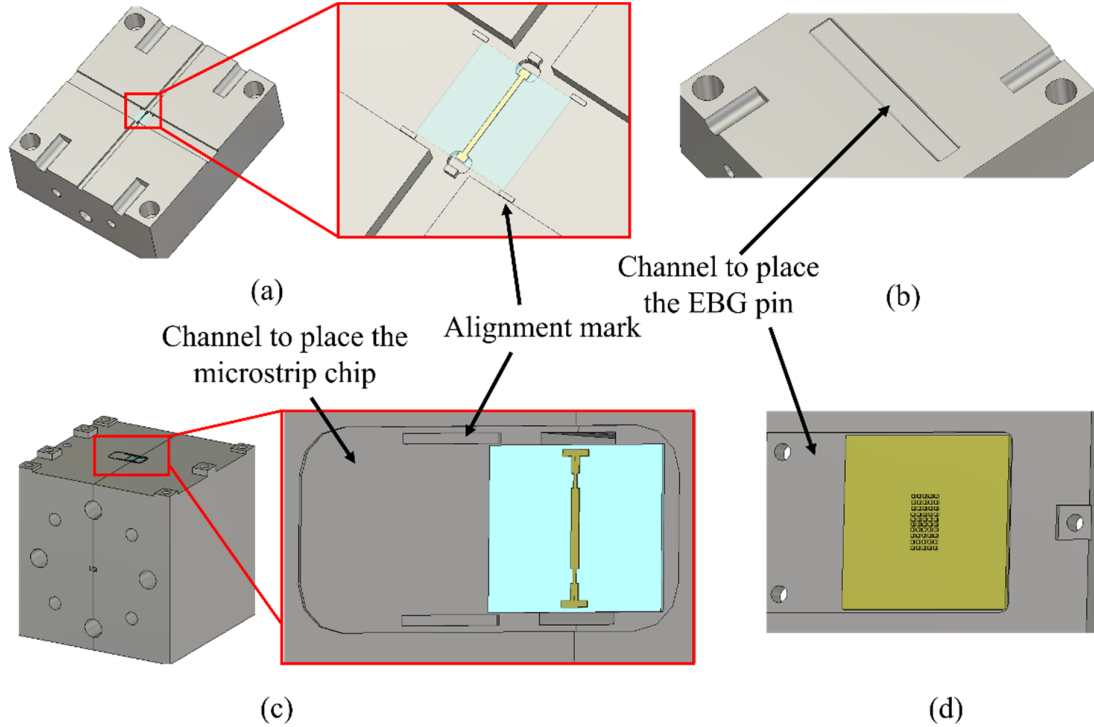


Figure 6.3: Schematic of the metal block, (a) bottom plate of the inline transition, (b) top plate of the inline transition, (c) bottom plate of the vertical transition, (d) top plate of the vertical transition.

6.4 Fabrication Method

The details of the fabrication method will be discussed in this section.

6.4.1 EBG pin fabrication

A silicon wafer was used as a substrate and once the fabrication of the EBG pins was done the structures have been released from the substrate before the deposition of the conductive layer.

To obtain the EBG structures for the vertical transition we used a 400 μm SUEX film as a base layer containing the EBG pins. After lamination the 400 μm SUEX film went through UV exposure and PEB, followed by the lamination of 200 μm , 40 μm , and 20 μm SUEX films to obtain 260 μm high pins. The laminated structure then went through the general dry film fabrication steps mentioned in Section 5.3 ii. The fabrication of the EBG structures for the inline transition was the same, except that the thickness of the base plate for the transition was 200 μm and the pin height was obtained by lamination of 200 μm , 40 μm , and 40 μm SUEX films. To make the chips conductive, 50 nm of titanium (Ti) and 200 nm gold (Au) have been sputtered followed by the electroplating of a 2 μm thick Au layer.

6.4.2 Microstrip line fabrication

For both transitions, quartz of 50 μm thickness has been chosen as the substrate. The microstrip line has been patterned on the quartz substrate. However, handling this thin quartz substrate was very challenging, and therefore the fabrication process was designed in two steps:

- i) attaching the quartz to a silicon (Si) wafer to secure the handling of this thin substrate
- ii) patterning the microstrip line.

A 2-inch quartz wafer has been used as a working substrate and the quartz wafer was attached to a Si wafer to secure the quartz during handling. A 20 μm thick SUEX film was used in this case as an additive material; it was laminated on a 4-inch Si wafer followed by placing the quartz wafer on it, subjecting it to a PLB for 10 mins at 65 $^{\circ}\text{C}$. The reason to perform this PLB is to ensure proper adhesion between the quartz and the Si. A flood exposure with the exposure energy of 300 mJ/cm^2 was done followed by a PEB. The flood exposure of the SUEX film ensures that the photoresist will not react during the development of the patterned resist, electroplating, or any other processing steps.

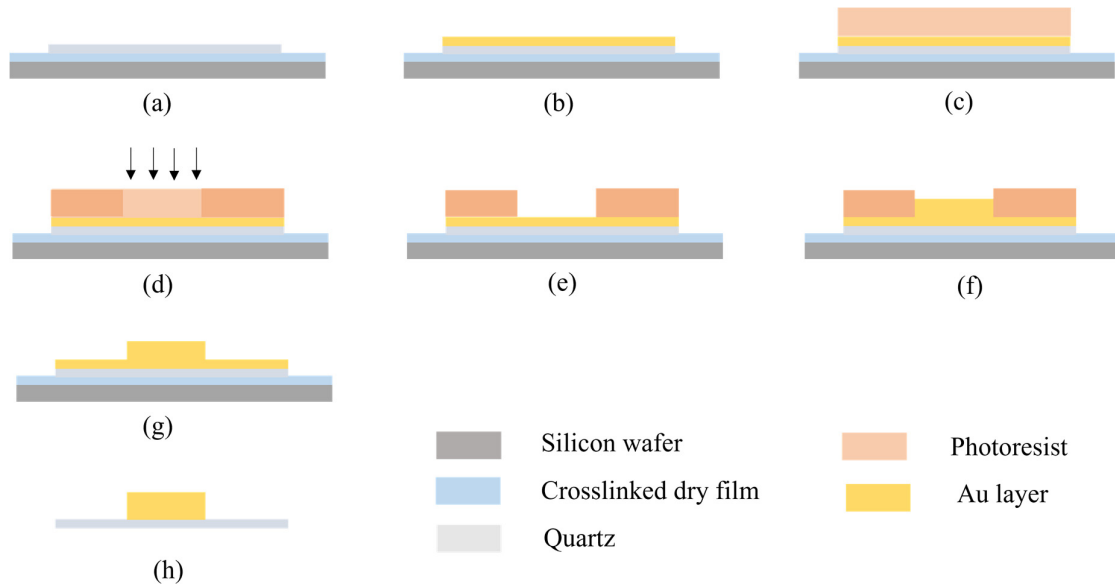


Figure 6.4: Schematic of the quartz fabrication, (a) preparing the quartz substrate for handling, (b) deposition of the seed layer, (c) spin coat resist S1813, (d) exposure of the photoresist, (e) photoresist after development, (f) electroplating of the quartz wafer, (g) removal of the photoresist, (h) dicing of the quartz wafer and releasing from the handling wafer.

The quartz wafer was then ready for patterning. 16 nm Ti and 20 nm Au were sputtered to obtain a seed layer. The photoresist S1813 was later used to pattern the seed layer. To obtain an approximately 1.8 μm thick structure by the photoresist, S1813 was spin-coated at 2000 rpm followed by a soft bake at 115 $^{\circ}\text{C}$ for 1 min. The photoresist was exposed at 150 mJ/cm^2 , developed by using developer MF319, and hard baked at 150 $^{\circ}\text{C}$ for 10 mins. The patterned quartz wafer went through the electroplating process. The electroplating parameters were tuned considering the narrow opening of the patterned photoresist. As the size of the electroplating bath was fixed in our case, varying the distance between the anode and the substrate was not possible. Therefore, we tuned the electroplating current and time considering the required

conductive layer thickness and the narrow openings of the patterned resist. After the electroplating, the photoresist has been removed by using acetone. The wafer was then diced into pieces and the quartz chip has been removed from the Si wafer. The seed layer was then removed by ion etching. Fig 6.4 shows the schematic of the quartz fabrication process.

6.5 Results and Discussion

The fabricated microstrip chips can be seen in Figure 6.5. The fabricated SUEX pins showed good accuracy, and the resulting pin heights are $\pm 5 \mu\text{m}$ of the nominal value. The measured surface roughness for the fabricated SUEX pins is $4.5 \pm 0.5 \text{ nm}$ and the microstrip line is $14 \pm 1.5 \text{ nm}$.

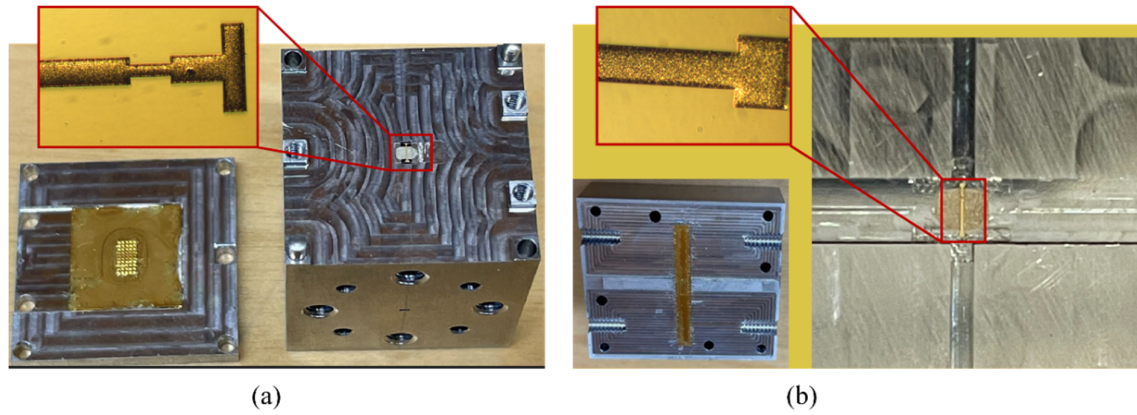


Figure 6.5: Fabricated microstrip chip and EBG pins mounted on the milled metal block, (a) vertical transition, (b) inline transition.

The measurement results for the vertical transition in the back-to-back case exhibit an insertion loss of 1.8 dB – 2.2 dB for the back-to-back transition. Figure 6.6a shows the image of the back-to-back transition during measurement. Therefore, the estimated loss per transition is approximately $\sim 0.9 \text{ dB}$ to 1.1 dB and this includes the losses in the waveguide and the transition section. The proposed transition works from 220 GHz to 285 GHz which translates to 26% fractional bandwidth of the entire frequency band, shown in Figure 6.6b. For this transition, we used the E-plane split block, and therefore we did not observe any major effect of leakage between the metal waveguide blocks.

The measurement of the inline transition has been done following the same procedure as the vertical transition. The return loss is better than -10 dB from 220 GHz to 310 GHz, shown in Fig 6.7. However, the measured insertion loss shows a significant discrepancy from the simulated result. The discrepancy can be explained by the surface roughness of the milled block and the additional distance between the waveguide port to the coupling pin, which was not considered in the simulation. During the optimization of the transition, the waveguide port was placed close to the coupling pin, whereas, in the final measurement, the distance between the waveguide port and the coupling pin was 15 mm. The surface roughness of the milled pieces was measured to be approximately $600 \text{ nm} \pm 10 \text{ nm}$. Additionally, to prevent any leakage from the metal blocks perfect electrical connection is needed. However, a $3 \mu\text{m}$ gap was measured between the two metal blocks after mounting them together with screws. After introducing the

Results and Discussion

measured surface roughness and 3 μm gap between the two metal blocks in the simulations, we observed an insertion loss very similar to the measurement result, shown in Fig. 6.7c.

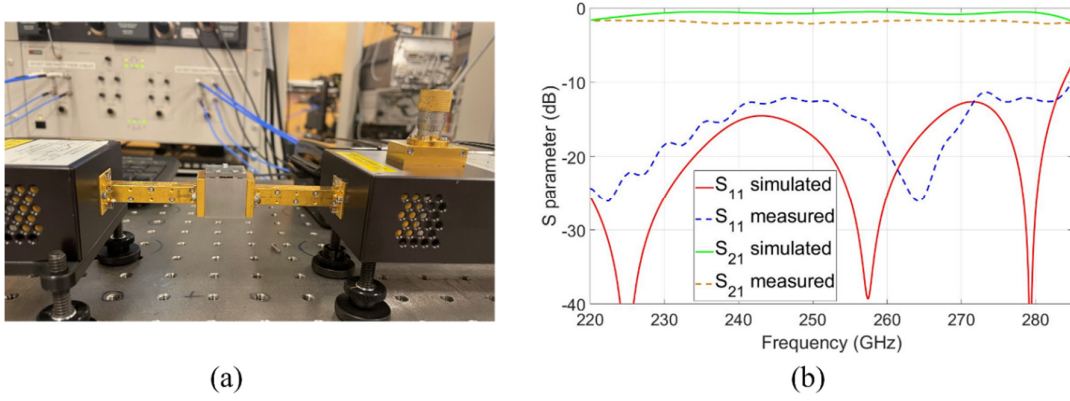


Figure 6.6: Measurement of the vertical transition, (a) measurement setup for the back-to-back waveguide transition, (b) simulation and measured S-parameter results for the back-to-back vertical transition.

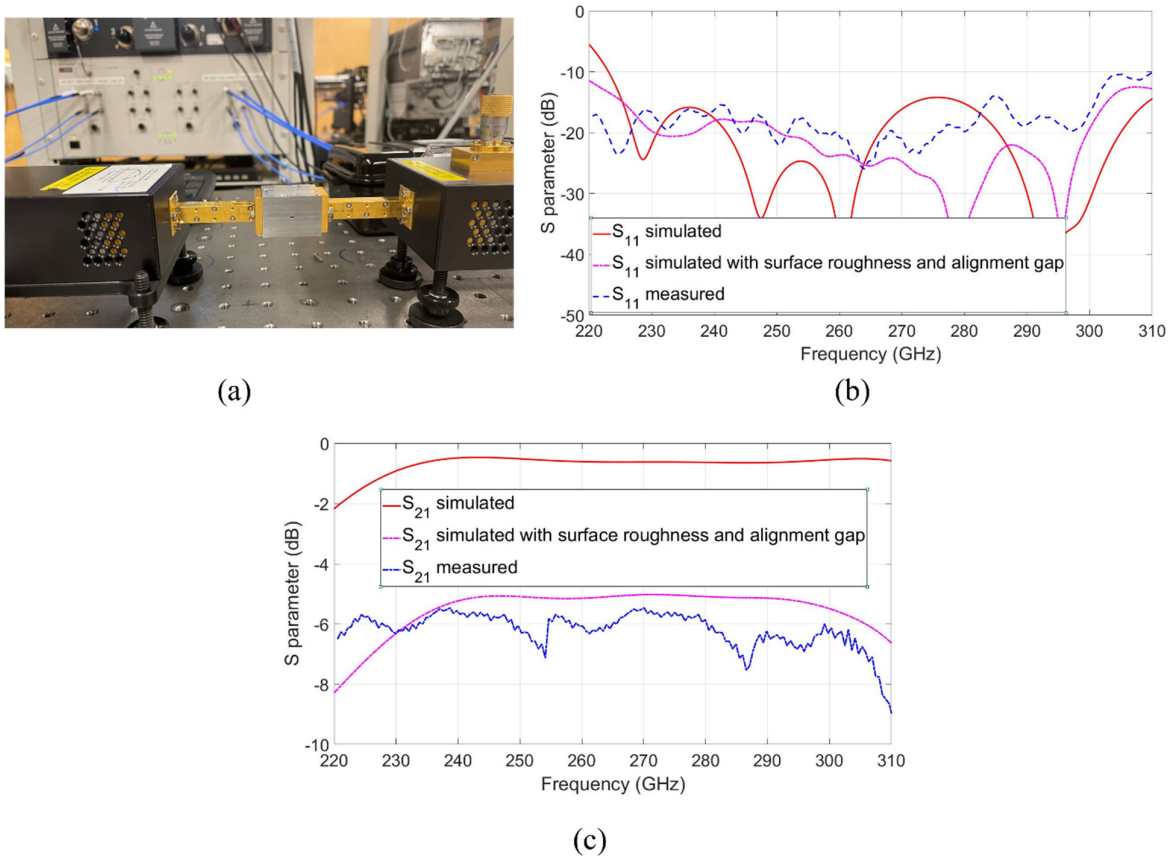


Figure 6.7: Measurement of the inline transition, (a) measurement setup for the back-to-back waveguide transition, (b) simulation and measured return loss for the back-to-back inline transition, (c) simulation and measured insertion loss for the back-to-back inline transition.

Accomplishment

Low insertion loss

The designed transitions showed satisfactory insertion loss, although the inline transition requires improved surface roughness quality of the milled pieces.

No limitation in MMIC size and no unwanted radiation

The EBG pins can prevent any unwanted mode to propagate through the substrate therefore the proposed transitions can be made as a part of the MMIC of arbitrary size. The EBG pins also guide the E-field and prevent leakage in undesired directions thereby suppressing any unwanted radiation which may create parasitic cavity modes or couple to other passive or active components present in the system.

Batch fabrication of the thin substrate and EBG pins

The fabrication process produced a microstrip chip with very low surface roughness and with high dimensional accuracy. Also, the adopted wafer handling technique is a straightforward way of handling very thin and fragile wafers. Previously the top EBG pins have been manufactured by milling. This is the first time that EBG pins have been fabricated by the microfabrication method. The high accuracy of the dry film fabrication and the resulting low surface roughness of the fabricated devices are very suitable for low-cost and large-volume production of devices operating at THz frequencies.

Wideband performance

The vertical transition offers 26% of the fractional bandwidth of the entire frequency band. The inline transition works for almost the entire band from 220 GHz to 310 GHz. Both transitions are wideband and suitable for applications where wideband performance is needed.

Limitations

Effect of H-plane split block

The inline transition showed a very high insertion loss compared to the simulation result. This high insertion loss is the effect of the high surface roughness of the milled pieces and the leakage due to the unwanted gap between the milled metal blocks. Figure 6.8 shows the gap between the two metal blocks.

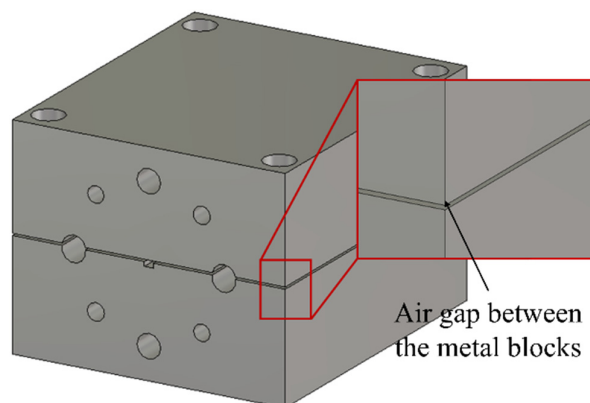


Figure 6.8: Schematic of the air gap between two split blocks for the inline transition.

Results and Discussion

Surface roughness of the milled pieces

The milled pieces showed very high surface roughness. To reduce the surface roughness, post-processing is needed which can add time and cost to the fabrication process.

Manual assembly of the fabricated chips

Even though the transition showed very good performance, the placement of the microstrip chip and the EBG pins is a manual process, which can affect the transition performance and reproducibility. This is a major bottleneck and can hinder the high-volume production of such systems.

Chapter 7

Conclusion and Future Work

At THz frequencies, i.e., above 100 GHz, the traditional machine-based waveguide manufacturing method becomes costly, complicated, and challenging. This is due to the wavelength-dependent miniaturization of waveguide components and increased sensitivity to fabrication tolerances. Micromachining processes have the potential to solve the problem. However, the existing micromachining techniques still suffer from some fabrication issues and need to be further improved for the waveguide components operating at THz frequencies. Furthermore, most of the potentially suitable microfabrication methods require complicated and time extensive processes and thereby prevent the batch fabrication of waveguide components in a cost-efficient way. The development of a fabrication technique that can overcome the challenges of the existing fabrication methods along with reducing the processing complexities and costs will be valued highly by the THz community.

GW technology is a promising waveguide technology, and it offers several benefits over the existing planar and hollow waveguides. The most attractive characteristic of GWs is that the electromagnetic wave propagates through the air in the GW structures and the presence of the AMC surface prevents leakage of EM waves in an unwanted direction. Therefore, the waveguide is not dependent on the dielectric properties of the material used for manufacturing. Hence, any material suitable to be used for low-cost fabrication can be used for the fabrication of gap waveguide structures, provided it can be coated with a suitable conductor. This introduces new opportunities to focus on batch fabrication of gap waveguide components cost-effectively. The thesis presents two microfabrication methods to fabricate passive waveguide components operating above 100 GHz.

The presented template-based injection molding process presented in Paper I is an example of a rapid manufacturing method. This process was designed by taking advantage of existing SU8-microfabrication schemes. Its perhaps most attractive feature is the reusability of the fabricated SU8 master and PDMS mold which will substantially reduce the fabrication time. The final device was obtained by injection molding of the photoresist OSTEMER. To validate the fabrication process, a high-gain slot array antenna based on GW technology was fabricated. This rapid, straightforward, and novel fabrication method successfully demonstrated the high gain antenna and validate good agreement between the measurement results and the simulation. However, there is room to improve the alignment accuracy between the PDMS molds and the Al mold by introducing an automated alignment process.

Given that injection molding is one efficient way of fast device fabrication, it is still interesting to explore other competitive materials that can be suitable to use directly to fabricate THz components. Considering the challenges of liquid photoresists, a SUEX dry film photoresist-based method was developed and investigated. The dry film photoresist-based fabrication method is very fast compared to other existing fabrication methods, and it requires less sensitive fabrication equipment. Promising measurement results of the dry film-based devices open a new door toward low-cost waveguide component fabrication at THz frequencies. An investigation of the thermal cycling effect on metal-coated SUEX structure has also been

conducted, showing the possibility of using the fabricated device where large temperature variations are expected.

The integration concepts presented in this thesis show a promising demonstration of wideband integration of multi-functional MMICs without being limited by substrate size. Both the microstrip chip and the EBG structure were fabricated by using microfabrication methods. Utilizing the high fabrication accuracy of SUEX processing, a periodic metal pin array has been fabricated, and a transition between RW to microstrip line has been proposed and demonstrated. This can constitute an effective and low-cost solution for integrating large-size MMICs into waveguide blocks. The demonstrated transition is also suitable for chip-to-chip transitions.

The thesis proposes two new fabrication methods. Both the injection molding and SUEX dry film photoresist-based methods showed high fabrication accuracy and reproducibility, as well as suitability for batch fabrication of passive waveguide THz components in a cost-efficient way. Table 7.1 presents a comparison of injection molding and SUEX dry film fabrication compared to current state-of-the-art fabrication methods. The main conclusion of the thesis is that polymers can be suitable for the fabrication of passive waveguide components operating at THz frequencies.

7.1 Future Work

Due to the time limitation of the involved projects, work beyond 320 GHz has not been carried out. More concentrated work can be done to extend the two proposed micromachining methods even above 300 GHz. More discrete components operating above 320 GHz and at different THz bands need to be implemented. The design tolerance will be more demanding at even higher frequencies. The compatibility of the fabrication processes can be explored by fabricating more passive components. Both proposed fabrication methods are very simple to work with and are suitable for batch fabrication of WG components. Therefore, complicated geometries such as double-sided structures or multilayers can be attempted to explore the full potential of these fabrication methods.

The integration of active and passive components merits further investigation. The CTEs of polymers are typically very different from those of metal and silicon, wherefore studies of thermal effects on integrating active components with polymer-based passive components will be required.

The proposed transitions showed promising potential for integrating the active RF circuits and polymer-based passive components, and a complete RF front-end realized with polymer-based components can be also explored.

Table 7.1: Comparison of different manufacturing technology for THz applications

Technology	CNC	3D printing	Silicon	SU8	Inj. molding*	SUEX
Processing steps	✓	✓	✗	✗	✓	✓
Processing time	✗✗	✗	✗✗	✗✗	✓✓	✓✓
Fabrication accuracy	✓	✓	✓✓	✓✓	✓✓	✓✓
Ability to deliver critical feature	✓	✓	✓✓	✓✓	✓✓	✓✓
Minimum feature size	✓	✓	✓✓	✓✓	✓✓	✓✓
Surface roughness	✗*	✗✗*	✓**	✓**	✓**	✓***
Mass producible	✗	✗	✓	✓	✓	✓
Product uniformity	✗	✗	✓✓	✓	✓✓	✓✓
Need of sophisticated tools	✗✗	✗	✗✗	✗	✓✓	✓✓
Production cost	✗✗	✓	✓	✓	✓✓	✓✓

A checkmark symbolizes the performance. ✗: reasonable, ✗✗: not satisfactory, ✓: good, ✓✓: very good

✗*: ~1 μm , ✗✗*: ~10 μm , ✓**: Less than 100 nm, ✓***: Less than 10 nm,

Inj. molding*: Injection molding not considering the reusable part fabrication steps.

Bibliography

1. Mittleman, D.M., *Perspective: Terahertz science and technology*. Journal of Applied Physics, 2017. **122**(23): p. 230901.
2. Lubecke, V.M., K. Mizuno, and G.M. Rebeiz, *Micromachining for terahertz applications*. IEEE Transactions on Microwave Theory and Techniques, 1998. **46**(11): p. 1821-1831.
3. Campion, J., et al., *Toward Industrial Exploitation of THz Frequencies: Integration of SiGe MMICs in Silicon-Micromachined Waveguide Systems*. IEEE Transactions on Terahertz Science and Technology, 2019. **9**(6): p. 624-636.
4. Xu, R., et al., *A Review of Broadband Low-Cost and High-Gain Low-Terahertz Antennas for Wireless Communications Applications*. IEEE Access, 2020. **8**: p. 57615-57629.
5. Lockie, D. and D. Peck, *High-data-rate millimeter-wave radios*. IEEE Microwave Magazine, 2009. **10**(5): p. 75-83.
6. Carpenter, S., et al., *A D-Band 48-Gbit/s 64-QAM/QPSK Direct-Conversion I/Q Transceiver Chipset*. IEEE Transactions on Microwave Theory and Techniques, 2016. **64**(4): p. 1285-1296.
7. Rodríguez-Vázquez, P., et al., *A 16-QAM 100-Gb/s 1-M Wireless Link With an EVM of 17% at 230 GHz in an SiGe Technology*. IEEE Microwave and Wireless Components Letters, 2019. **29**(4): p. 297-299.
8. Cooper, K.B., et al., *A High-Resolution Imaging Radar at 580 GHz*. IEEE Microwave and Wireless Components Letters, 2008. **18**(1): p. 64-66.
9. Cooper, K.B., et al., *Penetrating 3-D Imaging at 4- and 25-m Range Using a Submillimeter-Wave Radar*. IEEE Transactions on Microwave Theory and Techniques, 2008. **56**(12): p. 2771-2778.
10. Ning, W., et al., *Resolution Enhancement in Terahertz Imaging via Deconvolution*. IEEE Access, 2019. **7**: p. 65116-65121.
11. Taylor, Z.D., et al., *THz Medical Imaging: in vivo Hydration Sensing*. IEEE Transactions on Terahertz Science and Technology, 2011. **1**(1): p. 201-219.
12. Gui, S., J. Li, and Y. Pi, *Security Imaging for Multi-Target Screening Based on Adaptive Scene Segmentation With Terahertz Radar*. IEEE Sensors Journal, 2019. **19**(7): p. 2675-2684.
13. Appleby, R. and R.N. Anderton, *Millimeter-Wave and Submillimeter-Wave Imaging for Security and Surveillance*. Proceedings of the IEEE, 2007. **95**: p. 1683-1690.
14. Shang, X., et al., *Micromachined W-band waveguide and filter with two embedded H-plane bends*. Microwaves, Antennas & Propagation, IET, 2011. **5**: p. 334-339.
15. Zhang, M., J. Hirokawa, and M. Ando, *An E-Band Partially Corporate Feed Uniform Slot Array With Laminated Quasi Double-Layer Waveguide and Virtual PMC Terminations*. IEEE Transactions on Antennas and Propagation, 2011. **59**(5): p. 1521-1527.
16. Becker, J.P., J.R. East, and L. Katehi, *Performance of silicon micromachined waveguide at W-band*. Electronics Letters, 2002. **38**: p. 638-639.
17. Rebeiz, G.M., *RF MEMS: Theory, Design, and Technology*. 2003.
18. Rudolf, H., M. Carter, and A. Baryshev, *The ALMA Front End Optics—System Aspects and European Measurement Results*. IEEE Transactions on Antennas and Propagation, 2007. **55**(11): p. 2966-2973.
19. Pozar, D.M., *Microwave engineering*. 2011: John Wiley & sons.
20. Shang, X., et al., *Micromachined W-band waveguide and filter with two embedded H-plane bends*. Iet Microwaves Antennas & Propagation, 2011. **5**: p. 334-339.

Bibliography

21. Li, Y., et al., *Simulation and experiment on SIW slot array antennas*. IEEE Microwave and Wireless Components Letters, 2004. **14**(9): p. 446-448.
22. Hirokawa, J. and M. Ando, *Single-layer feed waveguide consisting of posts for plane TEM wave excitation in parallel plates*. IEEE Transactions on Antennas and Propagation, 1998. **46**(5): p. 625-630.
23. Bozzi, M., et al. *On the losses in substrate integrated waveguides*. in *2007 European Microwave Conference*. 2007.
24. Feng, X. and W. Ke, *Guided-wave and leakage characteristics of substrate integrated waveguide*. IEEE Transactions on Microwave Theory and Techniques, 2005. **53**(1): p. 66-73.
25. Kildal, P., et al., *Local Metamaterial-Based Waveguides in Gaps Between Parallel Metal Plates*. IEEE Antennas and Wireless Propagation Letters, 2009. **8**: p. 84-87.
26. Kildal, P. *Three metamaterial-based gap waveguides between parallel metal plates for mm/submm waves*. in *2009 3rd European Conference on Antennas and Propagation*. 2009.
27. Jung-Kubiak, C., et al., *A Multistep DRIE Process for Complex Terahertz Waveguide Components*. IEEE Transactions on Terahertz Science and Technology, 2016. **6**(5): p. 690-695.
28. Desmaris, V., et al. *Terahertz components packaging using integrated waveguide technology*. in *2011 IEEE MTT-S International Microwave Workshop Series on Millimeter Wave Integration Technologies*. 2011.
29. Tian, Y., X. Shang, and M. Lancaster, *Fabrication of multilayered SU8 structure for terahertz waveguide with ultralow transmission loss*. Journal of Micro/Nanolithography, MEMS, and MOEMS, 2014. **13**(1): p. 013002.
30. Shang, X., et al., *WR-3 Band Waveguides and Filters Fabricated Using SU8 Photoresist Micromachining Technology*. IEEE Transactions on Terahertz Science and Technology, 2012. **2**(6): p. 629-637.
31. Shah, U., et al., *A 500–750 GHz RF MEMS Waveguide Switch*. IEEE Transactions on Terahertz Science and Technology, 2017. **7**(3): p. 326-334.
32. Shang, X., et al., *Submillimeter wave waveguide filters fabricated by SU-8 process and laser micromachining (Review paper)*. IET Microwaves, Antennas & Propagation, 2017. **11**.
33. Zhao, X., et al., *Silicon Micromachined D-Band Diplexer Using Releasable Filling Structure Technique*. IEEE Transactions on Microwave Theory and Techniques, 2020. **68**(8): p. 3448-3460.
34. Krivovitca, A., et al. *Micromachined Silicon-core Substrate-integrated Waveguides with Coplanarprobe Transitions at 220–330 GHz*. in *2018 IEEE/MTT-S International Microwave Symposium - IMS*. 2018.
35. Reck, T.J., et al., *Measurement of Silicon Micromachined Waveguide Components at 500–750 GHz*. IEEE Transactions on Terahertz Science and Technology, 2014. **4**(1): p. 33-38.
36. Tong, Z. and A. Stelzer, *A Vertical Transition Between Rectangular Waveguide and Coupled Microstrip Lines*. IEEE Microwave and Wireless Components Letters, 2012. **22**(5): p. 251-253.
37. Vosoogh, A., H. Zirath, and Z.S. He, *Novel Air-Filled Waveguide Transmission Line Based on Multilayer Thin Metal Plates*. IEEE Transactions on Terahertz Science and Technology, 2019. **9**(3): p. 282-290.
38. Cabello-Sánchez, J., et al., *A Corrugated Planar-Goubau-Line Termination for Terahertz Waves*. IEEE Microwave and Wireless Technology Letters, 2023: p. 1-4.
39. Bauwens, M.F., et al. *A 1.1 THz micromachined on-wafer probe*. in *2014 IEEE MTT-S International Microwave Symposium (IMS2014)*. 2014.
40. Crowe, T.W., et al. *VNA frequency extenders to 1.1 THz*. in *2011 International Conference on Infrared, Millimeter, and Terahertz Waves*. 2011.
41. Rahiminejad, S., et al., *Micromachined contactless pin-flange adapter for robust high-frequency measurements*. Journal of Micromechanics and Microengineering, 2014. **24**(8): p. 084004.
42. Hörberg, M., et al., *A 110–170-GHz Non-Galvanic Interface for Integrating Silicon Micromachined Chips With Metallic Waveguide Systems*. IEEE Transactions on Microwave Theory and Techniques, 2021. **69**(8): p. 3667-3674.

43. Jam, A., et al., *A Non-Contact Waveguide Probe for On-Wafer S₁₁-Parameter Measurements for Submillimeter-Wave to Terahertz Band*. IEEE Transactions on Terahertz Science and Technology, 2014. **4**(4): p. 515-522.
44. Lu, H.C., et al., *Flip-Chip-Assembled W-Band CMOS Chip Modules on Ceramic Integrated Passive Device With Transition Compensation for Millimeter-Wave System-in-Package Integration*. IEEE Transactions on Microwave Theory and Techniques, 2012. **60**(3): p. 766-777.
45. Jameson, S. and E. Socher, *A Wide-Band CMOS to Waveguide Transition at mm-Wave Frequencies With Wire-Bonds*. IEEE Transactions on Microwave Theory and Techniques, 2015. **63**(9): p. 2741-2750.
46. Deal, W.R., et al., *A 670 GHz Low Noise Amplifier with <10 dB Packaged Noise Figure*. IEEE Microwave and Wireless Components Letters, 2016. **26**(10): p. 837-839.
47. Zaman, A.U., et al., *Millimeter Wave E-Plane Transition From Waveguide to Microstrip Line With Large Substrate Size Related to MMIC Integration*. IEEE Microwave and Wireless Components Letters, 2016. **26**(7): p. 481-483.
48. Zhang, Y., et al., *A Waveguide to Microstrip Inline Transition With Very Simple Modular Assembly*. IEEE Microwave and Wireless Components Letters, 2010. **20**(9): p. 480-482.
49. Boukari, B., et al., *Robust Microstrip-to-Waveguide Transitions for Millimeter-Wave Radar Sensor Applications*. IEEE Antennas and Wireless Propagation Letters, 2009. **8**: p. 759-762.
50. Cano, J.L., A. Mediavilla, and A.R. Perez, *Full-Band Air-Filled Waveguide-to-Substrate Integrated Waveguide (SIW) Direct Transition*. IEEE Microwave and Wireless Components Letters, 2015. **25**(2): p. 79-81.
51. Topak, E., J. Hasch, and T. Zwick, *Compact Topside Millimeter-Wave Waveguide-to-Microstrip Transitions*. IEEE Microwave and Wireless Components Letters, 2013. **23**(12): p. 641-643.
52. Samoska, L., et al., *A Submillimeter-Wave HEMT Amplifier Module With Integrated Waveguide Transitions Operating Above 300 GHz*. IEEE Transactions on Microwave Theory and Techniques, 2008. **56**(6): p. 1380-1388.
53. Cooke, C.M., et al. *Narrow-band Band-pass Filters for Terahertz Applications*. in *2021 IEEE MTT-S International Microwave Symposium (IMS)*. 2021.
54. Bruneau, P.J., H.D. Janzen, and J.S. Ward. *Machining of terahertz split-block waveguides with micrometer precision*. in *2008 33rd International Conference on Infrared, Millimeter and Terahertz Waves*. 2008.
55. Koller, D., E.W. Bryerton, and J.L. Hesler, *WM380 (675–700 GHz) Bandpass Filters in Milled, Split-Block Construction*. IEEE Transactions on Terahertz Science and Technology, 2018. **8**(6): p. 630-637.
56. Büchel, D., et al., *4.7-THz Superconducting Hot Electron Bolometer Waveguide Mixer*. IEEE Transactions on Terahertz Science and Technology, 2015. **5**(2): p. 207-214.
57. Chattopadhyay, G., et al., *Micromachined Packaging for Terahertz Systems*. Proceedings of the IEEE, 2017. **105**(6): p. 1139-1150.
58. Yu, Y., et al., *D-Band Waveguide Diplexer Fabricated Using Micro Laser Sintering*. IEEE Transactions on Components, Packaging and Manufacturing Technology, 2022. **12**(9): p. 1446-1457.
59. Nayeri, P., et al., *3D Printed Dielectric Reflectarrays: Low-Cost High-Gain Antennas at Sub-Millimeter Waves*. IEEE Transactions on Antennas and Propagation, 2014. **62**(4): p. 2000-2008.
60. Zhang, B. and H. Zirath, *Metallic 3-D Printed Rectangular Waveguides for Millimeter-Wave Applications*. IEEE Transactions on Components, Packaging and Manufacturing Technology, 2016. **6**(5): p. 796-804.
61. Shang, X., et al., *W-Band Waveguide Filters Fabricated by Laser Micromachining and 3-D Printing*. IEEE Transactions on Microwave Theory and Techniques, 2016. **64**(8): p. 2572-2580.
62. Konstantinou, X., et al., *Fully Aerosol Jet-Printed Passive Components for 140–220-GHz Operation*. IEEE Microwave and Wireless Technology Letters, 2022: p. 1-4.

Bibliography

63. Bartlett, C., J. Bornemann, and M. Höft, *3-D-Printing and High-Precision Milling of W-Band Filter Components With Admittance Inverter Sequences*. IEEE Transactions on Components, Packaging and Manufacturing Technology, 2021. **11**(12): p. 2140-2147.
64. Bieren, A.v., et al. *Monolithic metal-coated plastic components for mm-wave applications*. in *2014 39th International Conference on Infrared, Millimeter, and Terahertz waves (IRMMW-THz)*. 2014.
65. Zhang, B., et al., *Metallic 3-D Printed Antennas for Millimeter- and Submillimeter Wave Applications*. IEEE Transactions on Terahertz Science and Technology, 2016. **6**(4): p. 592-600.
66. Gu, C., et al., *A D-Band 3D-Printed Antenna*. IEEE Transactions on Terahertz Science and Technology, 2020. **10**(5): p. 433-442.
67. Zhang, B., et al., *Investigation on 3-D-Printing Technologies for Millimeter- Wave and Terahertz Applications*. Proceedings of the IEEE, 2017. **105**(4): p. 723-736.
68. Zhang, B., et al., *Review of 3D Printed Millimeter-Wave and Terahertz Passive Devices*. International Journal of Antennas and Propagation, 2017. **2017**: p. 1297931.
69. Rutledge, D., et al., *Antennas and waveguides for far-infrared integrated circuits*. IEEE Journal of Quantum Electronics, 1980. **16**(5): p. 508-516.
70. Silverio, V. and S. Cardoso de Freitas, *Microfabrication Techniques for Microfluidic Devices*, in *Complex Fluid-Flows in Microfluidics*, F.J. Galindo-Rosales, Editor. 2018, Springer International Publishing: Cham. p. 25-51.
71. Becker, J.P. and L.P.B. Katehi. *Toward a novel planar circuit compatible silicon micromachined waveguide*. in *IEEE 8th Topical Meeting on Electrical Performance of Electronic Packaging (Cat. No.99TH8412)*. 1999.
72. Yap, M., et al. *Silicon micromachined waveguides for millimeter and submillimeter wavelengths*.
73. Veidt, B., et al., *Diagonal horn integrated with micromachined waveguide for submillimetre applications*. Electronics Letters, 1995. **31**: p. 1307-1309.
74. Bean, K.E., *Anisotropic etching of silicon*. IEEE Transactions on Electron Devices, 1978. **25**(10): p. 1185-1193.
75. Seidel, H., et al., *Anisotropic Etching of Crystalline Silicon in Alkaline Solutions: II . Influence of Dopants*. Journal of The Electrochemical Society, 1990. **137**(11): p. 3626-3632.
76. Li, Y., P.L. Kirby, and J. Papapolymerou. *Silicon Micromachined W-Band Folded and Straight Waveguides Using DRIE Technique*. in *2006 IEEE MTT-S International Microwave Symposium Digest*. 2006.
77. Lee, Y., et al., *Fully micromachined finite-ground coplanar line-to-waveguide transitions for W-band applications*. IEEE Transactions on Microwave Theory and Techniques, 2004. **52**: p. 1001-1007.
78. Li, C., et al. *Fabrication and analysis of integrated MEMS pyramidal horn antenna for terahertz applications*. in *2012 7th IEEE International Conference on Nano/Micro Engineered and Molecular Systems (NEMS)*. 2012.
79. Kirby, P.L., et al. *A micromachined 400 GHz rectangular waveguide and 3-pole bandpass filter on a silicon substrate*. in *2004 IEEE MTT-S International Microwave Symposium Digest (IEEE Cat. No.04CH37535)*. 2004.
80. Liu, S., et al., *1 THz Micromachined Waveguide Band-Pass Filter*. Journal of Infrared, Millimeter, and Terahertz Waves, 2016. **37**(5): p. 435-447.
81. Reck, T., et al. *Silicon micromachined waveguide components at 0.75 to 1.1 THz*. in *2014 39th International Conference on Infrared, Millimeter, and Terahertz waves (IRMMW-THz)*. 2014.
82. Gomez-Torrent, A., et al., *A 38 dB Gain, Low-Loss, Flat Array Antenna for 320–400 GHz Enabled by Silicon-on-Insulator Micromachining*. IEEE Transactions on Antennas and Propagation, 2020. **68**(6): p. 4450-4458.
83. Pino, M.A.-d., et al., *Micromachining for Advanced Terahertz: Interconnects and Packaging Techniques at Terahertz Frequencies*. IEEE Microwave Magazine, 2020. **21**(1): p. 18-34.

84. Beuerle, B., et al., *A Very Low Loss 220–325 GHz Silicon Micromachined Waveguide Technology*. IEEE Transactions on Terahertz Science and Technology, 2018. **8**(2): p. 248-250.
85. Malmqvist, R., et al. *A 220–325 GHz low-loss micromachined waveguide power divider*. in *2017 IEEE Asia Pacific Microwave Conference (APMC)*. 2017.
86. Reck, T., et al., *A Silicon Micromachined Eight-Pixel Transceiver Array for Submillimeter-Wave Radar*. IEEE Transactions on Terahertz Science and Technology, 2015. **5**: p. 1-10.
87. Biber, S., et al., *Design and Measurement of a 600 GHz Micromachined Horn Antenna Manufactured by Combined DRIE and KOH-Etching of Silicon*. 2005.
88. Zhao, X.H., et al., *D-Band Micromachined Silicon Rectangular Waveguide Filter*. IEEE Microwave and Wireless Components Letters, 2012. **22**(5): p. 230-232.
89. Shuang, L., et al. *WR-1.0 band waveguide band-pass filter based on micromachining technique*. in *2014 IEEE International Conference on Communication Problem-solving*. 2014.
90. Reck, T., C. Jung-Kubiak, and G. Chattopadhyay, *A 700-GHz MEMS Waveguide Switch*. IEEE Transactions on Terahertz Science and Technology, 2016. **6**(4): p. 641-643.
91. Cegielski, P., et al., *A Four Level Silicon Microstructure Fabrication by DRIE*. 2015.
92. Rahiminejad, S., et al., *Demonstration of a micromachined planar distribution network in gap waveguide technology for a linear slot array antenna at 100 GHz*. Journal of Micromechanics and Microengineering, 2016. **26**: p. 074001.
93. Rahiminejad, S., et al., *Micromachined ridge gap waveguide and resonator for millimeter-wave applications*. Sensors and Actuators A: Physical, 2012. **186**: p. 264-269.
94. Zhao, X., O. Glubokov, and J. Oberhammer, *A Silicon-Micromachined Waveguide Platform With Axial Ports for Integrated Sub-THz Filters*. IEEE Transactions on Microwave Theory and Techniques, 2022. **70**(2): p. 1221-1232.
95. Khanal, S., et al. *A Waveguide Based Terahertz Variable Attenuator*. in *2022 47th International Conference on Infrared, Millimeter and Terahertz Waves (IRMMW-THz)*. 2022.
96. Shibata, N., et al. *600-GHz-band Silicon Dielectric Waveguide Module*. in *2021 46th International Conference on Infrared, Millimeter and Terahertz Waves (IRMMW-THz)*. 2021.
97. Zeng, L., et al., *A Silicon Chip-Based Waveguide Directional Coupler for Terahertz Applications*. IEEE Transactions on Terahertz Science and Technology, 2020. **10**(6): p. 698-703.
98. Mohr, J., *LIGA : A technology for fabricating microstructures and microsystems*. Sensors and Materials, 1998. **10**: p. 363-373.
99. Paoloni, C., et al., *Design and Realization Aspects of 1-THz Cascade Backward Wave Amplifier Based on Double Corrugated Waveguide*. IEEE Transactions on Electron Devices, 2013. **60**(3): p. 1236-1243.
100. Malekabadi, A. and C. Paoloni, *UV-LIGA microfabrication process for sub-terahertz waveguides utilizing multiple layered SU-8 photoresist*. Journal of Micromechanics and Microengineering, 2016. **26**(9): p. 095010.
101. Desmaris, V., et al. *Microfabrication Technology for All-Metal Sub-mm and THz Waveguide Receiver Components*. 2008.
102. Li, H., Y. Li, and J. Feng, *Fabrication of 340-GHz Folded Waveguides Using KMPR Photoresist*. IEEE Electron Device Letters, 2013. **34**(3): p. 462-464.
103. Li, H., J. Feng, and G. Bai. *Microfabrication of W-band folded waveguide slow wave structure using DRIE and UV-LIGA technology*. in *2011 IEEE International Vacuum Electronics Conference (IVEC)*. 2011.
104. Dochev, D., et al., *A Technology Demonstrator for 1.6–2.0 THz Waveguide HEB Receiver with a Novel Mixer Layout*. Journal of infrared, millimeter and terahertz waves, 2011. **32**: p. 451-465.
105. Liu, Y., et al., *UV-LIGA Based Discrete Fabrication Process for Terahertz Corrugated Feed Horn*. Procedia CIRP, 2020. **95**: p. 838-843.

Bibliography

106. Deng, J.Y., et al., *A 3 dB E-plane waveguide directional coupler employing micromachining technique for terahertz application*. Microwave and Optical Technology Letters, 2020. **62**(11): p. 3425-3431.
107. Collins, C.E., et al., *A new micro-machined millimeter-wave and terahertz snap-together rectangular waveguide technology*. IEEE Microwave and Guided Wave Letters, 1999. **9**(2): p. 63-65.
108. Shang, X., et al., *A SU8 Micromachined WR-1.5 Band Waveguide Filter*. IEEE Microwave and Wireless Components Letters, 2013. **23**(6): p. 300-302.
109. Wang, Y., et al., *Micromachined 300-GHz SU-8-Based Slotted Waveguide Antenna*. IEEE Antennas and Wireless Propagation Letters, 2011. **10**: p. 573-576.
110. Yang, H., et al., *WR-3 Waveguide Bandpass Filters Fabricated Using High Precision CNC Machining and SU-8 Photoresist Technology*. IEEE Transactions on Terahertz Science and Technology, 2018. **8**(1): p. 100-107.
111. Mahmud, R.H., et al., *Micromachined SU-8-Based Terahertz 8×8 Slotted Waveguide Antenna Array*. Journal of Infrared, Millimeter, and Terahertz Waves, 2021. **42**(11): p. 1116-1130.
112. Guo, C., et al., *A 135–150-GHz Frequency Tripler Using SU-8 Micromachined WR-5 Waveguides*. IEEE Transactions on Microwave Theory and Techniques, 2020. **68**(3): p. 1035-1044.
113. Aktary, M., et al., *High-resolution pattern generation using the epoxy novolak SU-8 2000 resist by electron beam lithography*. Journal of Vacuum Science & Technology B: Microelectronics and Nanometer Structures Processing, Measurement, and Phenomena, 2003. **21**(4): p. L5-L7.
114. Vora, K.D., et al., *Specification of mechanical support structures to prevent SU-8 stiction in high aspect ratio structures*. Journal of Micromechanics and Microengineering, 2005. **15**(5): p. 978-983.
115. Lin, C.-H., et al., *A new fabrication process for ultra-thick microfluidic microstructures utilizing SU-8 photoresist*. Journal of Micromechanics and Microengineering, 2002. **12**(5): p. 590-597.
116. Nordquist, C.D., et al., *Properties of Surface Metal Micromachined Rectangular Waveguide Operating Near 3 THz*. IEEE Journal of Selected Topics in Quantum Electronics, 2011. **17**(1): p. 130-137.
117. Digby, J.W., et al., *Fabrication and characterization of micromachined rectangular waveguide components for use at millimeter-wave and terahertz frequencies*. IEEE Transactions on Microwave Theory and Techniques, 2000. **48**(8): p. 1293-1302.
118. Vanhille, K., et al. *Ka-band surface-mount directional coupler fabricated using micro-rectangular coaxial transmission lines*. in 2008 IEEE MTT-S International Microwave Symposium Digest. 2008.
119. Jordan, J.W., et al. *Monolithically Fabricated 4096-Element, PolyStrata® Broadband D-band Array Demonstrator*. in 2019 IEEE MTT-S International Microwave Symposium (IMS). 2019.
120. Kildal, P., *Artificially soft and hard surfaces in electromagnetics*. IEEE Transactions on Antennas and Propagation, 1990. **38**(10): p. 1537-1544.
121. Kildal, P.-S., *Definition of Artificially Soft and Hard Surfaces for Electromagnetic Waves*. Electronics Letters, 1988. **24**: p. 168-170.
122. Silveirinha, M. and C. Fernandes, *Electromagnetic Characterization of Textured Surfaces Formed by Metallic Pins*. Antennas and Propagation, IEEE Transactions on, 2008. **56**: p. 405-415.
123. Sievenpiper, D., et al., *High-impedance electromagnetic surfaces with a forbidden frequency band*. IEEE Transactions on Microwave Theory and Techniques, 1999. **47**(11): p. 2059-2074.
124. Rajo-Iglesias, E. and P.-S. Kildal, *Numerical studies of bandwidth of parallel-plate cut-off realised by a bed of nails, corrugations and mushroom-type electromagnetic bandgap for use in gap waveguides*. Microwaves, Antennas & Propagation, IET, 2011. **5**: p. 282-289.
125. Valero-Nogueira, A., et al., *Experimental Demonstration of Local Quasi-TEM Gap Modes in Single-Hard-Wall Waveguides*. Microwave and Wireless Components Letters, IEEE, 2009. **19**: p. 536-538.
126. Valero-Nogueira, A., et al., *Gap Waveguides Using a Suspended Strip on a Bed of Nails*. Antennas and Wireless Propagation Letters, IEEE, 2011. **10**: p. 1006-1009.
127. Zaman, A.U., et al. *Increasing parallel plate stop-band in gap waveguides using inverted pyramid-shaped nails for slot array application above 60GHz*. in Proceedings of the 5th European Conference on Antennas and Propagation (EUCAP). 2011.

128. Rajo-Iglesias, E., et al., *Bed of Springs for Packaging of Microstrip Circuits in the Microwave Frequency Range*. IEEE Transactions on Components, Packaging and Manufacturing Technology, 2012. **2**(10): p. 1623-1628.
129. Rajo-Iglesias, E. and P. Kildal. *Groove gap waveguide: A rectangular waveguide between contactless metal plates enabled by parallel-plate cut-off*. in *Proceedings of the Fourth European Conference on Antennas and Propagation*. 2010.
130. Zaman, A.U. and P.-S. Kildal, *GAP Waveguides*, in *Handbook of Antenna Technologies*, Z.N. Chen, et al., Editors. 2016, Springer Singapore: Singapore. p. 3273-3347.
131. Brazález, A.A., A.U. Zaman, and P. Kildal. *Design of a coplanar waveguide-to-ridge gap waveguide transition via capacitive coupling*. in *2012 6th European Conference on Antennas and Propagation (EUCAP)*. 2012.
132. Vosoogh, A., A.U. Zaman, and J. Yang. *Simple and Broadband Transition Between Rectangular Waveguide and Groove Gap Waveguide for MM-Wave Applications*. in *2018 IEEE International Symposium on Antennas and Propagation & USNC/URSI National Radio Science Meeting*. 2018.
133. Brazález, A.A., et al., *Design and Validation of Microstrip Gap Waveguides and Their Transitions to Rectangular Waveguide, for Millimeter-Wave Applications*. IEEE Transactions on Microwave Theory and Techniques, 2015. **63**(12): p. 4035-4050.
134. Biurrún-Quel, C., J. Teniente, and C. del-Río, *Reduced Loss and Prevention of Substrate Modes with a Novel Coplanar Waveguide Based on Gap Waveguide Technology*. Sensors, 2023. **23**(6): p. 2909.
135. Zhang, B., Y. Zhang, and F. Xiao, *Broadband Contactless 90° Waveguide Transition with a U-Shaped Choke Groove*. IEEE Microwave and Wireless Components Letters, 2022. **32**(11): p. 1279-1282.
136. Chen, X. and D. Sun. *A Wideband E-plane Vertical Transition from Rectangle Waveguide to Groove Gap Waveguide*. in *2022 IEEE MTT-S International Wireless Symposium, IWS 2022 - Proceedings*. 2022.
137. Rossi, R. and R. Vincenti Gatti, *X-Band In-Line Coaxial-to-Groove Gap Waveguide Transition*. Electronics (Switzerland), 2022. **11**(15).
138. Pérez-Escudero, J.M., et al. *Design of a Groove Gap Waveguide to Microstrip inline transition*. in *2019 13th European Conference on Antennas and Propagation (EuCAP)*. 2019.
139. Zaman, A.U., et al. *Design of transition from coaxial line to ridge gap waveguide*. in *2009 IEEE Antennas and Propagation Society International Symposium*. 2009.
140. Pucci, E., et al., *Study of Q-factors of ridge and groove gap waveguide resonators*. Microwaves, Antennas & Propagation, IET, 2013. **7**: p. 900-908.
141. Ahmadi, B. and A. Banai, *Direct Coupled Resonator Filters Realized by Gap Waveguide Technology*. IEEE Transactions on Microwave Theory and Techniques, 2015. **63**(10): p. 3445-3452.
142. Sorkherizi, M.S., A. Khaleghi, and P. Kildal, *Direct-Coupled Cavity Filter in Ridge Gap Waveguide*. IEEE Transactions on Components, Packaging and Manufacturing Technology, 2014. **4**(3): p. 490-495.
143. Sharifi, M. and A. Kishk, *Completely Tuned Coupled Cavity Filters in Defected Bed of Nails Cavity*. IEEE Transactions on Components, Packaging and Manufacturing Technology, 2016. **PP**: p. 1-8.
144. Alós, E.A., A.U. Zaman, and P. Kildal, *Ka-Band Gap Waveguide Coupled-Resonator Filter for Radio Link Diplexer Application*. IEEE Transactions on Components, Packaging and Manufacturing Technology, 2013. **3**(5): p. 870-879.
145. Zaman, A.U., P. Kildal, and A.A. Kishk, *Narrow-Band Microwave Filter Using High-Q Groove Gap Waveguide Resonators With Manufacturing Flexibility and No Sidewalls*. IEEE Transactions on Components, Packaging and Manufacturing Technology, 2012. **2**(11): p. 1882-1889.
146. Rezaee, M., A. Zaman, and P.-S. Kildal, *A groove gap waveguide iris filter for V-band application*. 2015. 462-465.
147. Olmo-Olmeda, A.d., et al. *A novel band-pass filter topology for millimeter-wave applications based on the groove gap waveguide*. in *2013 IEEE MTT-S International Microwave Symposium Digest (MTT)*. 2013.

Bibliography

148. Berenguer, A., et al. *Low insertion loss 61 GHz narrow-band filter implemented with Groove Gap Waveguides*. in *2014 44th European Microwave Conference*. 2014.
149. Sun, D. and J. Xu, *A Novel Iris Waveguide Bandpass Filter Using Air Gapped Waveguide Technology*. IEEE Microwave and Wireless Components Letters, 2016. **26**(7): p. 475-477.
150. Al-Juboori, B., et al. *Millimeter wave cross-coupled bandpass filter based on groove gap waveguide technology*. in *2017 10th UK-Europe-China Workshop on Millimetre Waves and Terahertz Technologies (UCMMT)*. 2017.
151. Sorkherizi, M.S. and A.A. Kishk, *Self-Packaged, Low-Loss, Planar Bandpass Filters for Millimeter-Wave Application Based on Printed Gap Waveguide Technology*. IEEE Transactions on Components, Packaging and Manufacturing Technology, 2017. **7**(9): p. 1419-1431.
152. Vosough, A., A.A. Brazález, and P. Kildal, *A V-Band Inverted Microstrip Gap Waveguide End-Coupled Bandpass Filter*. IEEE Microwave and Wireless Components Letters, 2016. **26**(4): p. 261-263.
153. Sorkherizi, M.S. and A.A. Kishk, *Fully Printed Gap Waveguide With Facilitated Design Properties*. IEEE Microwave and Wireless Components Letters, 2016. **26**(9): p. 657-659.
154. Rezaee, M. and A. Zaman, *Groove Gap Waveguide Filter Based on Horizontally Polarized Resonators for V-Band Applications*. IEEE Transactions on Microwave Theory and Techniques, 2020. **PP**: p. 1-1.
155. Quan, Y., et al., *An unequal power divider based on ridge gap waveguide with an inserted conductor plate*. Microwave and Optical Technology Letters, 2021. **63**(2): p. 443-449.
156. Farahbakhsh, A., *Ka-Band Coplanar Magic-T Based on Gap Waveguide Technology*. IEEE Microwave and Wireless Components Letters, 2020. **30**(9): p. 853-856.
157. Quan, Y., et al., *A Simple Asymmetric Orthomode Transducer Based on Groove Gap Waveguide*. IEEE Microwave and Wireless Components Letters, 2020. **30**(10): p. 953-956.
158. Zarifi, D., A. Farahbakhsh, and A.U. Zaman, *Design and Fabrication of Wideband Millimeter-Wave Directional Couplers With Different Coupling Factors Based on Gap Waveguide Technology*. IEEE Access, 2019. **7**: p. 88822-88829.
159. Aljarosha, A., A.U. Zaman, and R. Maaskant, *A Wideband Contactless and Bondwire-Free MMIC to Waveguide Transition*. IEEE Microwave and Wireless Components Letters, 2017. **27**(5): p. 437-439.
160. Zaman, A.U. and P. Kildal, *Wide-Band Slot Antenna Arrays With Single-Layer Corporate-Feed Network in Ridge Gap Waveguide Technology*. IEEE Transactions on Antennas and Propagation, 2014. **62**(6): p. 2992-3001.
161. Liu, J., et al., *Design and Fabrication of a High-Gain 60-GHz Cavity-Backed Slot Antenna Array Fed by Inverted Microstrip Gap Waveguide*. IEEE Transactions on Antennas and Propagation, 2017. **65**(4): p. 2117-2122.
162. Zarifi, D., et al., *Design and Fabrication of a High-Gain 60-GHz Corrugated Slot Antenna Array With Ridge Gap Waveguide Distribution Layer*. IEEE Transactions on Antennas and Propagation, 2016. **64**(7): p. 2905-2913.
163. Sáez, A.J., et al., *Single-Layer Cavity-Backed Slot Array Fed by Groove Gap Waveguide*. IEEE Antennas and Wireless Propagation Letters, 2016. **15**: p. 1402-1405.
164. Ferrando-Rocher, M., et al., *A Dual-Polarized Slotted-Waveguide Antenna Based on Gap Waveguide Technology*. 2017.
165. Zarifi, D., A. Farahbakhsh, and A.U. Zaman, *A Gap Waveguide-Fed Wideband Patch Antenna Array for 60-GHz Applications*. IEEE Transactions on Antennas and Propagation, 2017. **65**(9): p. 4875-4879.
166. Farahbakhsh, A., D. Zarifi, and A.U. Zaman, *A mmWave Wideband Slot Array Antenna Based on Ridge Gap Waveguide With 30% Bandwidth*. IEEE Transactions on Antennas and Propagation, 2018. **66**(2): p. 1008-1013.
167. Ferrando-Rocher, M., et al., *Performance Assessment of Gap-Waveguide Array Antennas: CNC Milling Versus Three-Dimensional Printing*. IEEE Antennas and Wireless Propagation Letters, 2018. **17**: p. 2056-2060.

168. Liu, J., et al., *A Slot Array Antenna With Single-Layered Corporate-Feed Based on Ridge Gap Waveguide in the 60 GHz Band*. IEEE Transactions on Antennas and Propagation, 2019. **67**(3): p. 1650-1658.
169. Liu, J., A.U. Zaman, and J. Yang. *Two Types of High Gain Slot Array Antennas based on Ridge Gap Waveguide in the D-Band*. in *2019 IEEE-APS Topical Conference on Antennas and Propagation in Wireless Communications (APWC)*. 2019.
170. Sorkherizi, M.S., A. Dadgarpour, and A.A. Kishk, *Planar High-efficiency Antenna Array Using New Printed Ridge Gap Waveguide Technology*. IEEE Transactions on Antennas and Propagation, 2017. **65**(7): p. 3772-3776.
171. Pucci, E., et al., *Planar Dual-Mode Horn Array With Corporate-Feed Network in Inverted Microstrip Gap Waveguide*. IEEE Transactions on Antennas and Propagation, 2014. **62**(7): p. 3534-3542.
172. Razavi, S.A., et al. *Design of 60GHz planar array antennas using PCB-based microstrip-ridge gap waveguide and SIW*. in *The 8th European Conference on Antennas and Propagation (EuCAP 2014)*. 2014.
173. Rajo-Iglesias, E., A. Zaman, and P.-S. Kildal, *Parallel Plate Cavity Mode Suppression in Microstrip Circuit Packages Using a Lid of Nails*. Microwave and Wireless Components Letters, IEEE, 2010. **20**: p. 31-33.
174. Zaman, A.U., J. Yang, and P. Kildal. *Using Lid of pins for packaging of microstrip board for descrambling the ports of eleven antenna for radio telescope applications*. in *2010 IEEE Antennas and Propagation Society International Symposium*. 2010.
175. Zaman, A., et al., *Gap Waveguide PMC Packaging for Improved Isolation of Circuit Components in High-Frequency Microwave Modules*. Components, Packaging and Manufacturing Technology, IEEE Transactions on, 2014. **4**: p. 16-25.
176. Zhang, J., et al., *Gap Waveguide PMC Packaging for a SIW-GCPW-Based Filter*. IEEE Microwave and Wireless Components Letters, 2016. **26**(3): p. 159-161.
177. Ahmadi, B. and A. Banai, *Substrateless Amplifier Module Realized by Ridge Gap Waveguide Technology for Millimeter-Wave Applications*. IEEE Transactions on Microwave Theory and Techniques, 2016. **64**(11): p. 3623-3630.
178. Vosoogh, A., et al., *Compact Integrated Full-Duplex Gap Waveguide-Based Radio Front End For Multi-Gbit/s Point-to-Point Backhaul Links at E-Band*. IEEE Transactions on Microwave Theory and Techniques, 2019. **67**(9): p. 3783-3797.
179. Zaman, A.U., et al., *Design of a Simple Transition From Microstrip to Ridge Gap Waveguide Suited for MMIC and Antenna Integration*. IEEE Antennas and Wireless Propagation Letters, 2013. **12**: p. 1558-1561.
180. Nandi, U., et al., *Novel Millimeter Wave Transition From Microstrip Line to Groove Gap Waveguide for MMIC Packaging and Antenna Integration*. IEEE Microwave and Wireless Components Letters, 2017. **27**(8): p. 691-693.
181. Zaman, A.U., et al., *Novel Low-Loss Millimeter-Wave Transition From Waveguide-to-Microstrip Line Suitable for MMIC Integration and Packaging*. IEEE Microwave and Wireless Components Letters, 2017. **27**(12): p. 1098-1100.
182. Ren, Q., et al., *Novel Integration Techniques for Gap Waveguides and MMICs Suitable for Multilayer Waveguide Applications*. IEEE Transactions on Microwave Theory and Techniques, 2022. **70**(9): p. 4120-4128.
183. Monasterio, D., et al., *A Mode-Suppressing Metasurface for Large-Width MMICs Suitable for Tightly Packaged Millimeter and Submillimeter Heterodyne Receivers*. IEEE Transactions on Terahertz Science and Technology, 2021. **11**(6): p. 712-715.
184. Wang, H., W. Feng, and Y. Shi. *Microstrip-Ridge Gap Waveguide Layer Transition for Compact Waveguide Packaging Interconnection*. in *2022 IEEE MTT-S International Wireless Symposium (IWS)*. 2022.
185. Zheng, P., et al., *Design of a W-Band Full-Polarization Monopulse Cassegrain Antenna*. IEEE Antennas and Wireless Propagation Letters, 2017. **16**: p. 99-103.

Bibliography

186. Cheng, Y.J., Y.X. Guo, and Z.G. Liu, *W-Band Large-Scale High-Gain Planar Integrated Antenna Array*. IEEE Transactions on Antennas and Propagation, 2014. **62**(6): p. 3370-3373.
187. Miao, Z.W., et al., *140 GHz High-Gain LTCC-Integrated Transmit-Array Antenna Using a Wideband SIW Aperture-Coupling Phase Delay Structure*. IEEE Transactions on Antennas and Propagation, 2018. **66**(1): p. 182-190.
188. Tekkouk, K., et al., *Corporate-Feed Slotted Waveguide Array Antenna in the 350-GHz Band by Silicon Process*. IEEE Transactions on Antennas and Propagation, 2017. **65**(1): p. 217-225.
189. Vosoogh, A., et al., *W -Band Low-Profile Monopulse Slot Array Antenna Based on Gap Waveguide Corporate-Feed Network*. IEEE Transactions on Antennas and Propagation, 2018. **66**(12): p. 6997-7009.
190. Ding, X., et al., *A 16 × 16-Element Slot Array Fed by Double-Layered Gap Waveguide Distribution Network at 160 GHz*. IEEE Access, 2020. **8**: p. 55372-55382.
191. Cullens, E.D., et al., *Micro-Fabricated 130–180 GHz Frequency Scanning Waveguide Arrays*. IEEE Transactions on Antennas and Propagation, 2012. **60**(8): p. 3647-3653.
192. Xiao, J., et al., *140-GHz TE₃₄₀-Mode Substrate Integrated Cavities-Fed Slot Antenna Array in LTCC*. IEEE Access, 2019. **PP**: p. 1-1.
193. Kim, D., et al., *64 x 64-Element and 32x32-Element Slot Array Antennas Using Double-Layer Hollow-Waveguide Corporate-Feed in the 120 GHz Band*. IEEE Transactions on Antennas and Propagation, 2014. **62**(3): p. 1507-1512.
194. Carlborg, C.F., et al., *Beyond PDMS: off-stoichiometry thiol-ene (OSTE) based soft lithography for rapid prototyping of microfluidic devices*. Lab on a Chip, 2011. **11**(18): p. 3136-3147.
195. Lobov, G.S., et al., *Electro-optical effects of high aspect ratio P3HT nanofibers colloid in polymer microfluid cells*. Optics Letters, 2017. **42**(11): p. 2157-2160.
196. Sandström, N., et al., *Reaction injection molding and direct covalent bonding of OSTE+ polymer microfluidic devices*. Journal of Micromechanics and Microengineering, 2015. **25**(7): p. 075002.
197. Rosato, D.V., D.V. Rosato, and M.V. Rosato, *12 - REACTION INJECTION MOLDING*, in *Plastic Product Material and Process Selection Handbook*, D.V. Rosato, D.V. Rosato, and M.V. Rosato, Editors. 2004, Elsevier: Oxford. p. 406-427.
198. Shafagh, R.Z., W.v.d. Wijngaart, and T. Haraldsson. *NANORIM: Sub-micron structuring with reaction injection molding*. in *2017 IEEE 30th International Conference on Micro Electro Mechanical Systems (MEMS)*. 2017.
199. Rahiminejad, S., et al. *Rapid manufacturing of OSTE polymer RF-MEMS components*. in *2017 IEEE 30th International Conference on Micro Electro Mechanical Systems (MEMS)*. 2017.
200. Pardon, G., et al., *Rapid mold-free manufacturing of microfluidic devices with robust and spatially directed surface modifications*. Microfluidics and Nanofluidics, 2014. **17**(4): p. 773-779.
201. Pirskanen, J., et al., *Replication of sub-micrometre features using microsystems technology*. Plastics, Rubber and Composites, 2005. **34**(5-6): p. 222-226.
202. Scott, S.M. and Z. Ali, *Fabrication Methods for Microfluidic Devices: An Overview*. Micromachines (Basel), 2021. **12**(3).
203. Johnsona, D.W., et al. *SUEx Dry Film Resist@ A new Material for High Aspect Ratio Lithography*. 2012.
204. Maurischat, K., *Dry film photoresists - a never ending success story?* Circuit World, 1998. **24**(2): p. 34-37.
205. Leong, Y.W., et al. *Forming a Vertical Interconnect Structure Using Dry Film Processing for Fan Out Wafer Level Packaging*. in *2017 IEEE 67th Electronic Components and Technology Conference (ECTC)*. 2017.
206. Vulto, P., et al., *Microfluidic channel fabrication in dry film resist for production and prototyping of hybrid chips*. Lab on a Chip, 2005. **5**(2): p. 158-162.
207. Ehrfeld, W., et al., *Materials of LIGA technology*. Microsystem Technologies, 1999. **5**(3): p. 105-112.

208. Lorenz, H., et al., *Low-cost technology for multilayer electroplated parts using laminated dry film resist*. Sensors and Actuators A: Physical, 1996. **53**(1): p. 364-368.
209. Kukhareuka, E., et al., *Electroplating moulds using dry film thick negative photoresist*. Journal of Micromechanics and Microengineering, 2003. **13**.
210. Kukhareuka, E., et al., *Electroplating moulds using dry film thick negative photoresist*. Journal of Micromechanics and Microengineering, 2003. **13**(4): p. S67.
211. Johnson, D.W., et al. *SUEx process optimization for ultra-thick high-aspect ratio LIGA imaging*. in *Advanced Lithography*. 2011.
212. Johnson, D.W., et al. *SUEx Dry Film Resist – A new Material for High Aspect Ratio Lithography*. 2012.
213. DJ MicroLaminates, I., *Product Data Sheet, SUEx® Thick Dry Film Sheets (TDFS)*. June 2020.
214. Rahiminejad, S., et al., *SU8 ridge-gap waveguide resonator*. International Journal of Microwave and Wireless Technologies, 2014. **6**: p. 459-465.
215. Ding, J.Q., et al., *WR-3 Band Quasi-Elliptical Waveguide Filters Using Higher Order Mode Resonances*. IEEE Transactions on Terahertz Science and Technology, 2017. **7**(3): p. 302-309.
216. R. Kerr, C.L., G. Petencin, D. Koller, and M. Shannon, *Loss of gold plated waveguides at 210-280 GHz*. ALMA MEMO 585, 2009: p. 1-6.
217. Yingtao, T., S. Xiaobang, and J.L. Michael, *Fabrication of multilayered SU8 structure for terahertz waveguide with ultralow transmission loss*. Journal of Micro/Nanolithography, MEMS, and MOEMS, 2014. **13**(1): p. 013002.
218. Skaik, T., et al. *A micromachined WR-3 waveguide with embedded bends for direct flange connections*. in *The 40th European Microwave Conference*. 2010.
219. Stanec, J.R. and N.S. Barker, *Fabrication and Integration of Micromachined Submillimeter-Wave Circuits*. IEEE Microwave and Wireless Components Letters, 2011. **21**(8): p. 409-411.
220. von Bieren, A., et al., *Monolithic metal-coated plastic components for mm-wave applications*. International Conference on Infrared, Millimeter, and Terahertz Waves, IRMMW-THz, 2014.
221. Dimitrijevic, S., et al., *Temperature effect on decorative gold coatings obtained from electrolyte based on mercaptotriazole - Comparison with cyanide*. International Journal of Materials Research, 2014. **105**: p. 272-281.
222. Reddy, H., et al., *Temperature-dependent optical properties of gold thin films*. Optical Materials Express, 2016. **6**(9): p. 2776-2802.
223. Pfeiffer, U.R., et al. *Current Status of Terahertz Integrated Circuits - From Components to Systems*. in *2018 IEEE BiCMOS and Compound Semiconductor Integrated Circuits and Technology Symposium (BCICTS)*. 2018.
224. Kordiboroujeni, Z. and J. Bornemann, *New Wideband Transition From Microstrip Line to Substrate Integrated Waveguide*. IEEE Transactions on Microwave Theory and Techniques, 2014. **62**(12): p. 2983-2989.
225. Dong, Y., et al. *A D-Band Rectangular Waveguide-to-Coplanar Waveguide Transition Using Metal Ridge*. in *2019 IEEE MTT-S International Microwave Symposium (IMS)*. 2019.
226. Hassona, A., et al., *Compact Low-Loss Chip-to-Waveguide and Chip-to-Chip Packaging Concept Using EBG Structures*. IEEE Microwave and Wireless Components Letters, 2021. **31**(1): p. 9-12.
227. Niklaus, F., et al., *Adhesive wafer bonding*. Journal of Applied Physics, 2006. **99**(3): p. 031101.
228. Oberhammer, J., F. Niklaus, and G. Stemme, *Sealing of adhesive bonded devices on wafer level*. Sensors and Actuators A: Physical, 2004. **110**(1): p. 407-412.

Bibliography